

8-2010

Principal Component Analysis based Image Fusion Routine with Application to Stamping Split Detection

Yi Zhou

Clemson University, yizhou2009@hotmail.com

Follow this and additional works at: https://tigerprints.clemson.edu/all_dissertations

 Part of the [Operations Research, Systems Engineering and Industrial Engineering Commons](#)

Recommended Citation

Zhou, Yi, "Principal Component Analysis based Image Fusion Routine with Application to Stamping Split Detection" (2010). *All Dissertations*. 615.

https://tigerprints.clemson.edu/all_dissertations/615

This Dissertation is brought to you for free and open access by the Dissertations at TigerPrints. It has been accepted for inclusion in All Dissertations by an authorized administrator of TigerPrints. For more information, please contact kokeefe@clemson.edu.

PRINCIPAL COMPONENT ANALYSIS
BASED IMAGE FUSION ROUTINE
WITH APPLICATION TO STAMPING SPLIT DETECTION

A Dissertation
Presented to
the Graduate School of
Clemson University

In Partial Fulfillment
of the Requirements for the Degree
Doctor of Philosophy
Automotive Engineering

by
Yi Zhou
August 2010

Accepted by:
Dr. Mohammed A. Omar, Committee Chair
Dr. Imtiaz Haque
Dr. Thomas R. Kurfess
Dr. Todd H. Hubing

ABSTRACT

This dissertation presents a novel thermal and visible image fusion system with application in online automotive stamping split detection. The thermal vision system scans temperature maps of highly reflective steel panels to locate abnormal temperature readings indicative of high local wrinkling pressure that causes metal splitting. The visible vision system offsets the blurring effect of thermal vision system caused by heat diffusion across the surface through conduction and heat loss to the surroundings through convection. The fusion of thermal and visible images combines two separate physical channels and provides more informative result image than either of the original ones.

Principal Component Analysis (PCA) is employed to transform original image to its eigenspace. By retaining the principal components with influencing eigenvalues, PCA keeps the key features in the original image and reduces noise level. Then pixel level image fusion algorithms are developed to fuse original images from the thermal and visible channels, enhance the result image from low level and reduce undesirable noises. Finally, an automatic split detection algorithm is designed and implemented to perform online objective automotive stamping split detection.

The integrated PCA based image fusion system for stamping split detection is developed and tested on an automotive press line. It is also assessed by online thermal and visible acquisitions and illustrates performance and success. Different splits with variant shape, size and amount are detected under actual operating conditions.

DEDICATION

To my family.

ACKNOWLEDGMENTS

I would like to acknowledge my advisor, Dr. Mohammad Omar, for his continuous support and patient guidance throughout this work. I also would like to thank my committee members, Dr. Imtiaz Haque, Dr. Thomas Kurfess and Dr. Todd Hubing for their valuable suggestions and comments to improve the quality of this work.

The author also would like to acknowledge our industrial partners: Mr. Tomokazu Okuno and Mr. Masahiro Yamakage from Toyota Motor Manufacturing Kentucky Inc.; Ms. Charlene Lane and Mr. Joel VanWingerden from Spartanburg Steel Products Inc. for their technical support and constructive cooperation.

Special thanks to Mr. Rohit Parvataneni, Mr. Eric Planting, Mr. Konda Reddy and other colleagues in our research group. Finally I appreciate any help from other co-workers and friends that makes this work possible.

TABLE OF CONTENTS

	Page
ABSTRACT.....	ii
DEDICATION.....	iii
ACKNOWLEDGMENTS	iv
TABLE OF CONTENTS.....	v
LIST OF TABLES.....	viii
LIST OF FIGURES	ix
CHAPTER ONE INTRODUCTION.....	1
1.1 Motivation.....	1
1.2 Problem Statement.....	2
1.3 Objectives	4
1.4 Approaches	5
1.5 Dissertation Organization	6
CHAPTER TWO THERMOGRAPHY.....	8
2.1 Literature Review of Stamping Process Control	8
2.1.1 Contact Method.....	9
2.1.2 Non-contact Method	13
2.2 Thermography Introduction.....	22
2.3 Thermography in Stamping Split Detection	25
2.3.1 Template Preprocessing	28
2.3.2 Split Detection	32
2.4 Thermography Limitations and Image Fusion.....	39
2.5 Summary	40
CHAPTER THREE IMAGE FUSION.....	41
3.1 Image Fusion Introduction.....	41
3.2 Literature Review of Image Fusion	43

Table of Contents (Continued)

	Page
3.3 Image Fusion in Night Vision.....	49
3.3.1 Pixel Level Image Fusion	53
3.3.2 Feature Level Image Fusion.....	64
3.3.3 Pixel Level Image Fusion vs. Feature Level Image Fusion.....	73
3.4 Summary	77
CHAPTER FOUR PRINCIPAL COMPONENT ANALYSIS	78
4.1 PCA Introduction	78
4.2 Literature Review of PCA	78
4.2.1 PCA in Thermography	78
4.2.2 PCA in Image Fusion.....	79
4.3 PCA Implementation	81
4.3.1 Original PCA	82
4.3.2 SVD based PCA.....	88
4.3.3 Economical SVD based PCA.....	89
4.4 PCA Application in Thermography	90
4.5 PCA Application in Image Fusion.....	95
4.6 Summary	106
CHAPTER FIVE PCA BASED FUSION IN STAMPING SPLIT DETECTION	107
5.1 System Overview	107
5.2 Camera System	111
5.3 Image Acquisition.....	112
5.3.1 FLIR ThermoVison SDK.....	112
5.3.2 MATLAB Image Acquisition Tool Box.....	117
5.4 Graphical User Interface	120
5.5 Principal Component Analysis	126
5.6 Image Fusion.....	128
5.7 Image Fusion Evaluation	131
5.7.1 Standard Deviation.....	131
5.7.2 SNR.....	132
5.7.3 Entropy.....	133
5.7.4 Cross Entropy.....	133

Table of Contents (Continued)

	Page
5.7.5 Mutual Information.....	134
5.8 Split Detection	135
5.9 Summary	139
CHAPTER SIX CONCLUSION	140
6.1 Conclusion	140
6.2 Contributions.....	142
6.3 Limitations and Future Work.....	143
REFERENCES	146

LIST OF TABLES

Table	Page
Table 5.1: Specifications of Thermal and Visible Cameras	111
Table 5.2: ThermoVision SDK Summary of API.....	114
Table 5.3: Comparison Results of Different Image Fusion Methods	135

LIST OF FIGURES

Figure	Page
Figure 1.1: Circle Grid Analysis (CGA).....	3
Figure 1.2: Photogrammetry based Sheet Metal Forming Analysis	4
Figure 2.1: Physical Setup of Stamping Operation.....	8
Figure 2.2: Schematics of the Hydraulic Mini-press	10
Figure 2.3: Arrangement of Rig and Sensors for Deep Drawing	11
Figure 2.4: A Schematic Representation of the PDS	12
Figure 2.5: The Schematic of Automatic Metallic Surface Inspection.....	14
Figure 2.6: The Defect Inspection Procedures.....	14
Figure 2.7: Construction Principle of the Optical Sensor	15
Figure 2.8: Utilization of the Optical Sensor in a Deep Drawing Tool	16
Figure 2.9: The Automatic Inspection System for Flow Detection on Car-body Parts	17
Figure 2.10: The Automatic Inspection System Diagram	18
Figure 2.11: The Thermal Distribution Acquisition System	19
Figure 2.12: Block Diagram of the Thermal Energy Distribution based Diagnosis.....	20
Figure 2.13: Thermal FEA of a Deep Drawing Cup.....	20
Figure 2.14: Thermal Image of the Deep Drawing Cup	20
Figure 2.15: Sample Thermal Images (a) Split-free; (b) Major Split; (c) Minor Split	28
Figure 2.16: Template Image after Thresholding	30
Figure 2.17: Template Image after Region Detection	31
Figure 2.18: Template ROI Image	32

List of Figures (Continued)

Figure	Page
Figure 2.19: Flow Chart of Split Detection	33
Figure 2.20: Contrast in ROI between Raw Image and Template Image.....	34
Figure 2.21: Large Contrast Regions in Template ROI.....	35
Figure 2.22: Split Detection Results: (a) Major Split; (b) Minor Split.....	37
Figure 2.23: Graphical User Interface of Stamping Split Detection Routines	38
Figure 3.1: Scheme of Pixel Level Fusion.....	41
Figure 3.2: Scheme of Feature Level Fusion	42
Figure 3.3: Scheme of Decision Level Fusion.....	43
Figure 3.4: Scheme of MST based Image Fusion.....	47
Figure 3.5: Scheme of Generic DWT Fusion	48
Figure 3.6: Passing Vehicle Scenario: (a) Thermal Image; (b) Visible Image.....	51
Figure 3.7: Approaching Vehicle Scenario: (a) Thermal Image; (b) Visible Image	53
Figure 3.8: Flow Chart of Pixel Level Image Fusion Algorithm.....	54
Figure 3.9: Pixel Level Fusion Result Image of Passing Vehicle Scenario.....	56
Figure 3.10: Histogram of Pixel Level Fusion Result Image of Passing Vehicle Scenario	58
Figure 3.11: Result Image after Seed Initiation	58
Figure 3.12: Boundary Detection Flow Chart.....	59
Figure 3.13: Result Image after Sobel Edge Detection.....	60
Figure 3.14: Result Image of Sobel Edge after Thresholding	61

List of Figures (Continued)

Figure	Page
Figure 3.15: Result Image with Object Boundaries.....	61
Figure 3.16: Flow Chart of Seed Growth.....	62
Figure 3.17: Result Image with Tracking Information	64
Figure 3.18: Flow Chart of Feature Level Image Fusion Routine	65
Figure 3.19: Seed Initiation Results: (a) Thermal Image; (b) Visible Image	67
Figure 3.20: Boundary Detection Results: (a) Thermal Image; (b) Visible Image	68
Figure 3.21: Feature Extraction Results: (a) Thermal Image; (b) Visible Image	69
Figure 3.22: Feature Relationships: (a) Intersection; (b) Disjoint; (c) Inclusion.....	70
Figure 3.23: Feature Level Fusion Result of Passing Vehicle Scenario.....	72
Figure 3.24: Feature Level Fusion Result of Approaching Vehicle Scenario	72
Figure 3.25: Image Fusion Results of Passing Vehicle Scenario: (a) Pixel Level; (b) Feature Level	74
Figure 3.26: Image Fusion Results of Approaching Vehicle Scenario: (a) Pixel Level; (b) Feature Level	76
Figure 4.1: Flow Chart of Original PCA	82
Figure 4.2: Sequence of Nt Image Frames with Width Nx and Height Ny	83
Figure 4.3: Flow Chart of SVD Based PCA.....	89
Figure 4.4: Result of Flash Ring Sample: (a) Raw Image; (b) Result Image	92
Figure 4.5: Result of Induction Heater Sample: (a) Raw Image; (b) Result Image.....	93
Figure 4.6: Result of Halogen Lamp Sample: (a) Raw Image; (b) Result Image.....	94

List of Figures (Continued)

Figure	Page
Figure 4.7: Flow Chart of PCA based Image Fusion.....	96
Figure 4.8: Passing Vehicle Scenario 1: (a) Raw Thermal Image; (b) Thermal Image after PCA; (c) Raw Visible Image; (d) Visible Image after PCA; (e) Fused Image without PCA; (f) Fused Image with PCA.....	99
Figure 4.9: Passing Vehicle Scenario 2: (a) Raw Thermal Image; (b) Thermal Image after PCA; (c) Raw Visible Image; (d) Visible Image after PCA; (e) Fused Image without PCA; (f) Fused Image with PCA.....	102
Figure 4.10: Approaching Vehicle Scenario: (a) Raw Thermal Image; (b) Thermal Image after PCA; (c) Raw Visible Image; (d) Visible Image after PCA; (e) Fused Image without PCA; (f) Fused Image with PCA.....	106
Figure 5.1: Configuration of PCA based Fusion System for Stamping Split Detection.	108
Figure 5.2: Experimental Setup of PCA based Image Fusion System	109
Figure 5.3: Stamping Split Sample of Vehicle Wheelhouse Part	110
Figure 5.4: Example Instructions using FLIR SDK Camera ActiveX Control Module.	115
Figure 5.5: FLIR SDK Camera ActiveX Control Module: (a) Camera Disconnected; (b) Camera Connected.....	116
Figure 5.6: Image Acquisition Toolbox Software Components	118
Figure 5.7: Example Instructions using MATLAB Image Acquisition Toolbox	119
Figure 5.8: GUI of PCA based Image Fusion System	121
Figure 5.9: File Menu of PCA based Image Fusion System GUI	122

List of Figures (Continued)

Figure	Page
Figure 5.10: Camera Menu of PCA based Image Fusion System GUI	122
Figure 5.11: ROI Menu of PCA based Image Fusion System GUI.....	123
Figure 5.12: ROI Selection of PCA based Image Fusion System GUI	124
Figure 5.13: Functions of PCA based Image Fusion System GUI	125
Figure 5.14: Result Images with and without PCA: (a) Raw Thermal Image; (b) Raw Visible Image; (c) Thermal Image after PCA; (d) Visible Image after PCA	128
Figure 5.15: Image Fusion Results with and without PCA: (a) Raw Thermal Image; (b) Raw Visible Image; (c) Thermal Image after PCA; (d) Visible Image after PCA; (e) Fixed Weighted Average without PCA; (f) Fixed Weighted Average with PCA; (g) PCA Weighted Average without PCA; (h) PCA Weighted Average with PCA; (i) Max Selection without PCA; (j) Max Selection with PCA.....	131
Figure 5.16: Flow Chart of Stamping Split Detection	136
Figure 5.17: Stamping Split Detection Intermediate Results of Sample 1: (a) Fused Image; (b) Template Image; (c) ROI; (d) Masked Contrast Image; (e) Detected Regions; (f) Regions after Closing; (g) Split Region; (h) Original Image with Split Detection	138
Figure 5.18: Stamping Split Detection Intermediate Results of Sample 2: (a) Fused Image; (b) Template Image; (c) ROI; (d) Masked Contrast Image; (e)	

Detected Regions; (f) Regions after Closing; (g) Split Region; (h) Original
Image with Split Detection 139

CHAPTER ONE

INTRODUCTION

1.1 Motivation

Stamping process is vital for the automotive manufacturing chain because it decides vehicle's structure, geometric dimensioning, body in white fit as well as final quality and performance. Typically, a vehicle shell is made up of 300 to 400 stamping components. However, ensuring high quality stamping is still a big challenge.

Firstly, it's difficult to control over forty stamping parameters that may suffer from unexplained deviations simultaneously in a short period, which makes the onsite stamping process control extremely complicated [1, 2].

Secondly, the material deviations of sheet metal are further complicated due to the increasing use of new steel grades such as High Strength Low Alloy (HSLA), Dual Phase (DP), in addition to Aluminum which has low n-value, narrow stamping window and high tendency to spring-back.

Furthermore, current stamping inspection and evaluation techniques are still based on subjective visual sampling conducted by line operators due to the complexity of stamping process and diversity of parts [3]. This operator-based subjective inspection requires extensive time and resources but does not guarantee defect escape and consistency.

Therefore, all these challenges motivate a strong need to develop new automotive stamping inspection approaches to provide online objective evaluation of stampings.

1.2 Problem Statement

Automotive stampings are evaluated based on appearance, strain and dimension that can be quantified using the Universal Formability Technology (UFT) developed by Ford Motor Company.

Depending on the mechanisms of stamping defects, there are six formability indices to evaluate automotive stampings:

- (1) Anti-fracturability for splits
- (2) Anti-edge fracturability for splits on edges
- (3) Anti-wrinklability for wrinkles
- (4) Shape-fixability for shape change
- (5) Stretchability for low stretch
- (6) Anti-bucklability for surface soft

Based on the above formability indices, current onsite stamping evaluation techniques are dependent on direct strain measurements.

Circle Grid Analysis (CGA) is a typical direct strain measurement method that utilizes calibration sample to evaluate the strains and directions used to adjust the stamping parameters. It can evaluate the strain location and magnitude, direction of metal displacement, strain distribution, and deformation mode as shown in Figure 1.1.

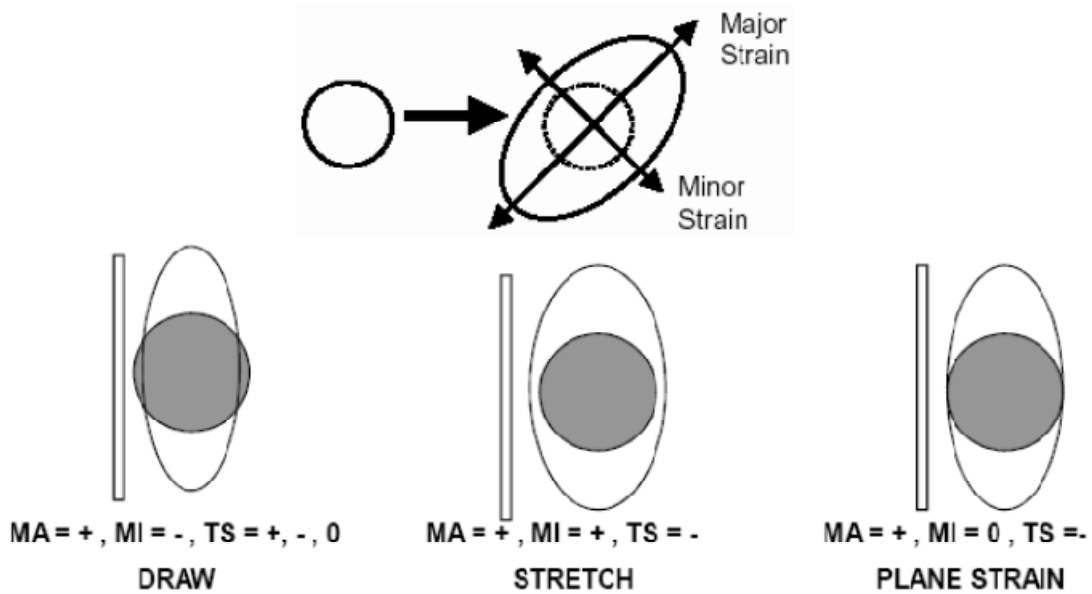


Figure 1.1: Circle Grid Analysis (CGA)

Photogrammetry is another strain measurement technique used to evaluate the onsite stamping quality [4]. First, it defines center points of many thousand marked dots in each image of the calibration sample. Then, the images are virtually assembled to represent the calibration sample as shown in Figure 1.2. From this virtual assembly, the center of each marked dot is defined in 3D coordinates. From the local distortion of the regular grid pattern, the local strain introduced by the stamping process is calculated. These strain values as well as the thickness reductions define the degree of the forming and are used for stamping evaluation.

However, in both CGA and Photogrammetry, the stamping shape, size and pattern should be calibrated before mass production for each material and thickness [5]. Furthermore, they are only useful for validating and calibrating stampings offline to

achieve designer's forming limit diagram. Thus, they can't be used as online tools to evaluate stampings and inspect defects.

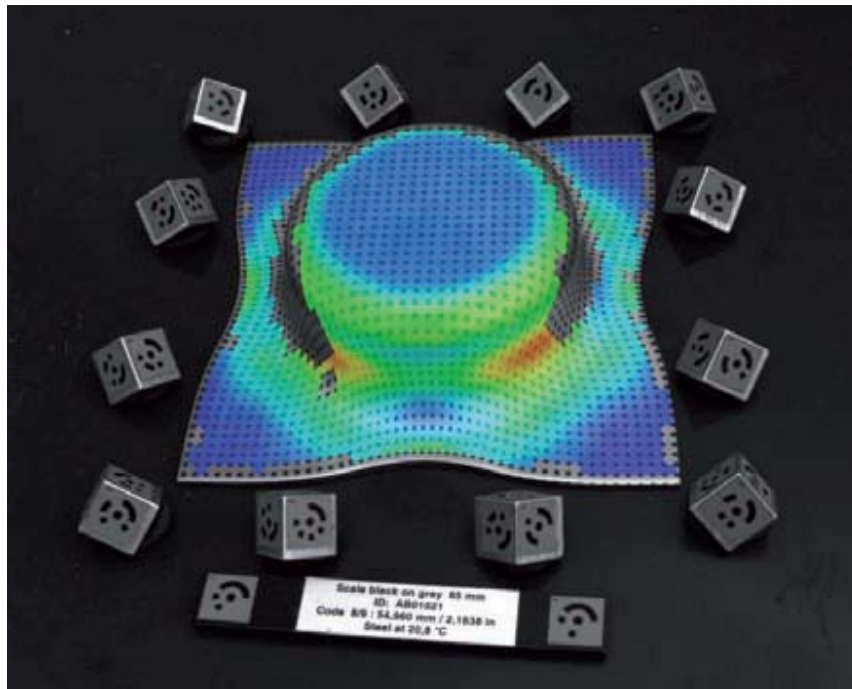


Figure 1.2: Photogrammetry based Sheet Metal Forming Analysis

1.3 Objectives

Due to the importance and challenge of current stamping process control, there is a strong need to develop new online inspection approach to provide automatic objective evaluation for automotive stampings. The goal of this dissertation is to develop a non-contact, non-intrusive online inspection system to evaluate automotive stampings and improve stamping process control.

Firstly, non-contact and non-intrusive inspection approach is non-destructive and versatile for complex shapes and various materials. It also helps to improve the stamping process control without impacting the line production rate.

Secondly, automatic online stamping inspection approach employs objective evaluation criteria for inspection thus eliminates subjective deviations introduced by line operators.

Finally, the online inspection approach helps in detecting defects instantly during the stamping process and provides instant feedback to adjust the stamping parameters, thus prevents the generation of further defects and defects escape.

1.4 Approaches

The PCA based image fusion system for stamping split detection is unique for combining Thermography, image fusion and PCA into an integrated system for online stamping split detection application.

First, a thermal vision modality based on Thermography is developed to detect stamping splits by correlating temperature maps to the die wrinkling pressure to detect split regions as hot spots. However, heat conduction and heat convection on the surface of the stamping part blur the thermal image and reduce its spatial resolution. To address this issue, image fusion technique is utilized to fuse another visible image with the thermal image for image enhancement.

Then, principal component analysis is employed to enhance the features in the original images and also reduce noise level. Later on, a pixel level image fusion

algorithm is developed to fuse thermal and visible images and generate more informative result image.

Finally, a seed growth based split detection algorithm is developed to extract features from fused image and perform automatic objective split detection providing split specifications such location, size, temperature and so forth.

1.5 Dissertation Organization

Chapter 1 presents the motivation, objectives and approaches of the dissertation and outlines its organization.

From Chapter 2 to Chapter 4, three major techniques, Thermography, image fusion and PCA, are introduced in theories and demonstrated with applications, respectively.

Chapter 2 introduces Thermography basics and presents its application in stamping split detection. To offset the drawbacks of Thermography, a fusion of thermal and visible images is motivated.

In Chapter 3, literature review of different image fusion techniques is presented and an image fusion application in night vision is developed and described with technical details.

Chapter 4 introduces PCA basics in Thermography and image fusion. PCA based image enhancement is developed and described in application of sheet metal protection coat inspection and night vision.

Chapter 5 integrates above three major techniques and demonstrates an integrated PCA based image fusion system for online stamping split detection developed on an automotive press line.

Finally, Chapter 6 wraps up the entire dissertation and presents the contributions and future work.

CHAPTER TWO
THERMOGRAPHY

2.1 Literature Review of Stamping Process Control

A typical stamping tool consists of three parts: the punch, the die and the binder as shown in Figure 2.1 [6, 7]. During stamping process, the punch presses the workpiece down into the die causing plastic deformation. The flow of the workpiece into the die is regulated by the binder force that holds the periphery of the workpiece between the binder and the die flange. The movement of the workpiece edge between the binder and the die flange is called drawn-in which is an important manufacturing index and also an indicator of the success of stamping process. Insufficient draw-in causes splits and excessive thinning while excessive draw-in induces wrinkles and surface defects.

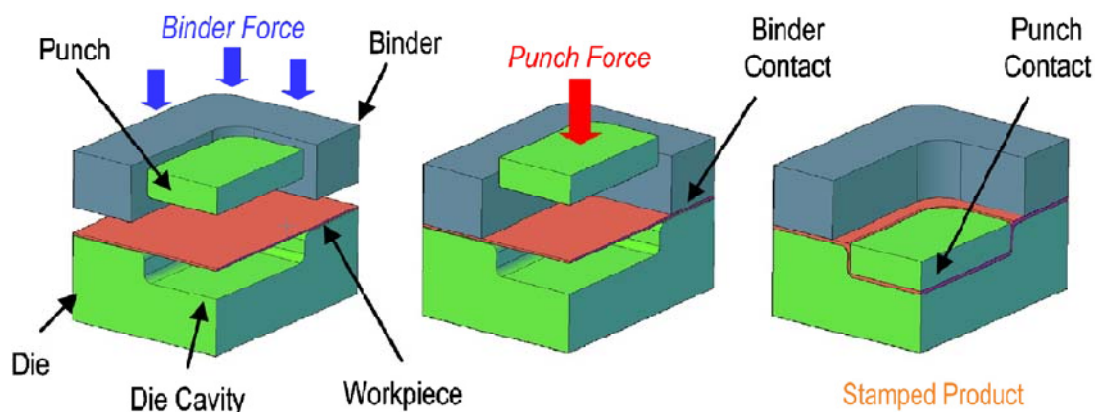


Figure 2.1: Physical Setup of Stamping Operation

Published literature on stamping process control method can be classified into two categories: stamping tool oriented contact method and stamping part oriented non-contact method.

The contact method typically installs draw-in sensors in the draw die to measure stamping data. It is usually used for offline applications in stamping diagnosis, modeling, simulation or reverse engineering to provide analysis of the stamping system for later improvement.

The non-contact method utilizes camera, ultrasonic, or microwave to measure the stamping data with no physical contact to the part. It is usually used for online applications to provide fast onsite defect detection for productivity and cost reduction.

2.1.1 Contact Method

The contact method typically analyzes the fault diagnosis of the stamping activities through monitoring the press tonnage. The analysis requires intensive computation to compress the data content and establish correlation to the stamping quality. Therefore, it is mainly used offline in research phase to improve the press tonnage and the die system. The key points are the modeling of the stamping process and the cause of the defect.

Draw-in sensors such as displacement sensor (LVDT), force sensor and pressure sensor (PZT) and strain gauge are widely utilized in contact stamping inspection system to measure the draw-in amount, speed, force, and pressure distribution. Through correlating multi-physical parameters, such as contact pressure, draw-in punch force, and

press traveling, the stamping process model can be well established for analysis and diagnostic.

Sun et al [8, 9] presented a hydraulic mini-press control system as shown in Figure 2.2 to evaluate stamping springback. The hydraulic press is equipped with a set of sensors to measure the system pressure and piston position. The actuation force is measured through two pressure sensors installed on the cylinder chambers. The piston position is measured through an optical scale and its acceleration is monitored through an accelerometer. The velocity is obtained by differentiation of the position signal. All inputs of the sensors and the electrical valves are connected to a DSP based real-time card from dSPACE that real-time control and acquisition can be performed.

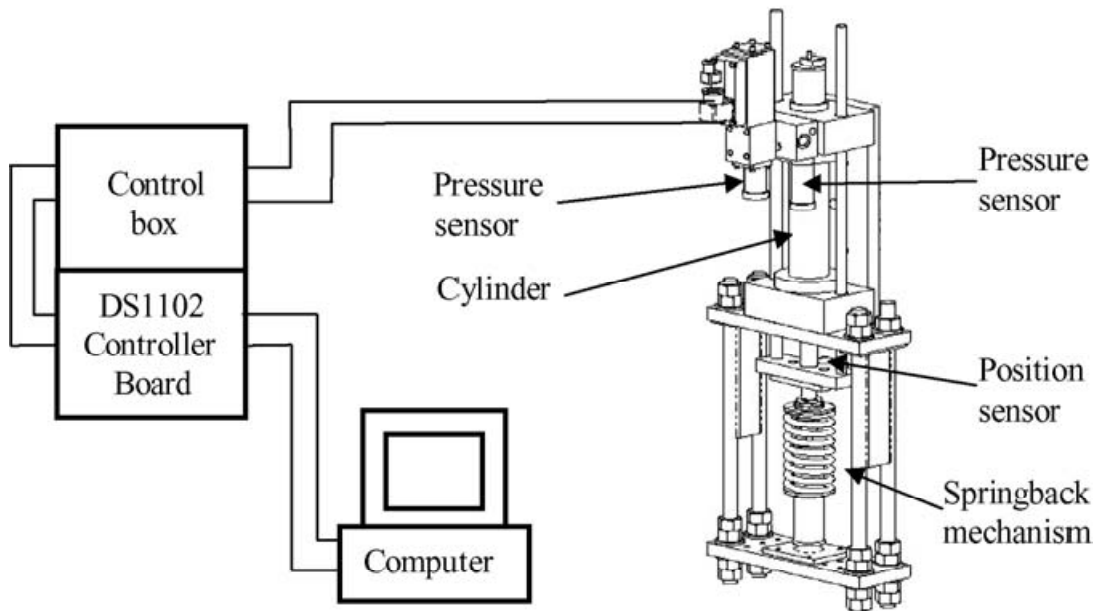


Figure 2.2: Schematics of the Hydraulic Mini-press

However, the tonnage sensing is limited in stamping process control application compared to tooling-embedded sensing, because it only relates to global parameters of the tonnage. This makes tonnage sensing incompatible with the need for spatial localization of disturbances or defects in the stamping process [7].

Lo et al [10, 11] demonstrated an adaptable Blank Holding Force (BHF) monitoring and control system to prevent the sidewall tearing and to restrain the flange from wrinkling during stamping process. The system shown in Figure 2.3 contains a Photoelectric Displacement Sensor (PDS) used to detect the movement of sheet metal on the die shoulder and a LVDT transducer on the upper die used to measure the wrinkle height during the stamping process. The output of the PDS is used to calculate the real-time minimum thickness of the sidewall. Together with the output of the LVDT, the results of the calculation serve as feedback parameters for the BHF control.

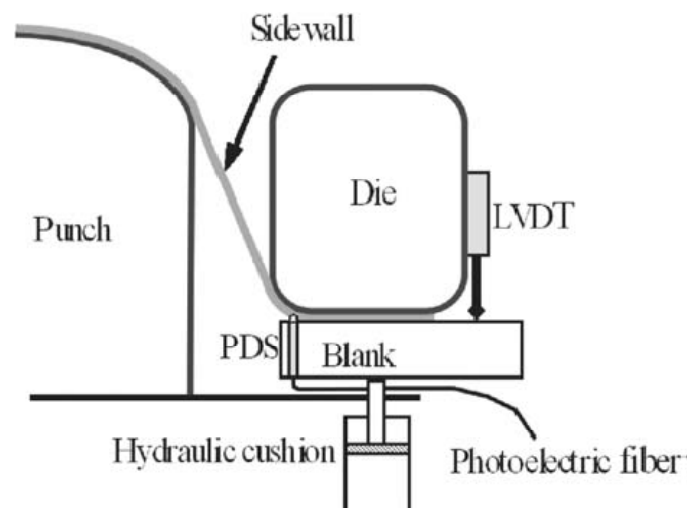


Figure 2.3: Arrangement of Rig and Sensors for Deep Drawing

The PDS consists of a gear sandwiched between two friction wheels, a sliding pin with spring, a fixing plug with an O-ring, and a fiber photoelectric sensor of reflection type as shown in Figure 2.4. It is inserted in a hole in the blank holder close to the punch side so that the sensor can pick up the movement of sheet metal on the die shoulder.

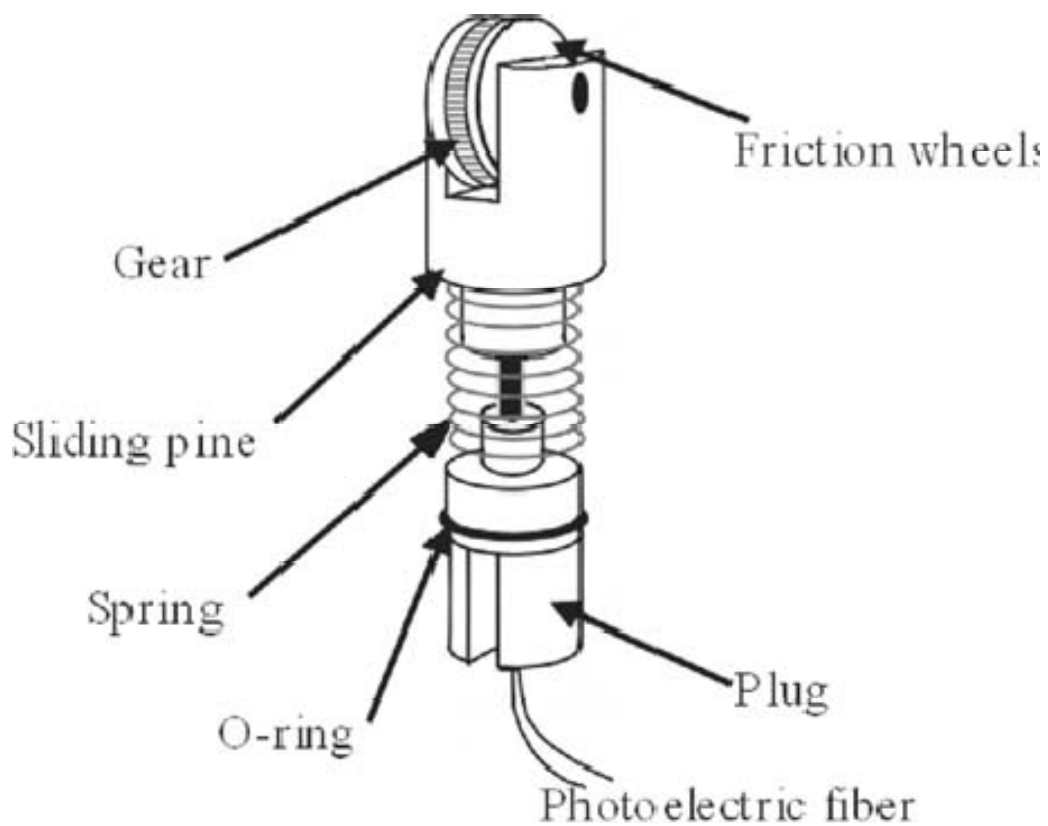


Figure 2.4: A Schematic Representation of the PDS

However, the LVDT type draw-in sensor is based on the resistance and requires physical touch of the tip on the sheet metal edge. The contact between the sheet and the LVDT tip could be lost when the edge starts to wrinkle [6].

2.1.2 Non-contact Method

The non-contact method detects the defect in stamping process in a real-time manner and sends out feedbacks signal instantly to reduce stamping waste. It focuses more on surface inspection of stamping part for fast defect detection. The key points are accuracy, speed and working range on parts with complex geometry.

Zheng et al [12] proposed an automatic inspection system to detect structural defects on metallic surfaces using machine vision, morphology and Genetic Algorithms (GA). The inspection system consists of three components: image acquisition, image processing, and decision making as shown in Figure 2.5. The image acquisition system has a lighting source sensitive to structural defects and a CCD camera. The image produced is subjected to grayscale morphology based processing. The genetic algorithms are employed to learn morphology processing parameters such as structuring elements and defect segmentation threshold. The image data is then classified to extract defect candidates or suspicious regions. Finally, the system generates the detection results and provides specific information of detects.

The defect inspection process is divided to two steps as shown in Figure 2.6. The first step is the learning phase, in which GAs are used to extract two groups of optimal structuring element parameters. One is segment threshold used for hole defects and the other one is noise removal threshold used for crack defects. The second step is the implementing phase, in which the parameters obtained by GAs are used for morphological processing for defect detection.

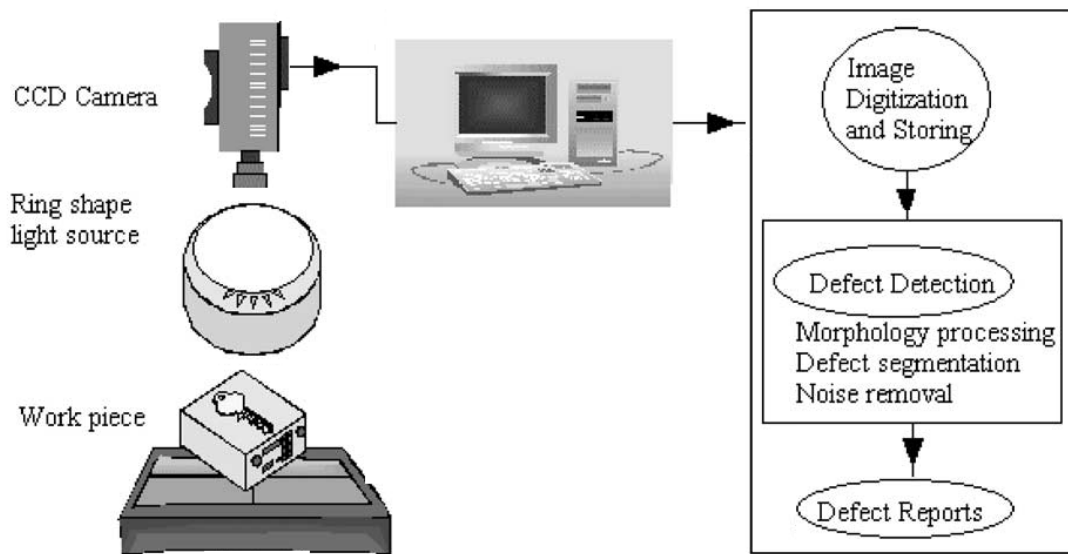


Figure 2.5: The Schematic of Automatic Metallic Surface Inspection

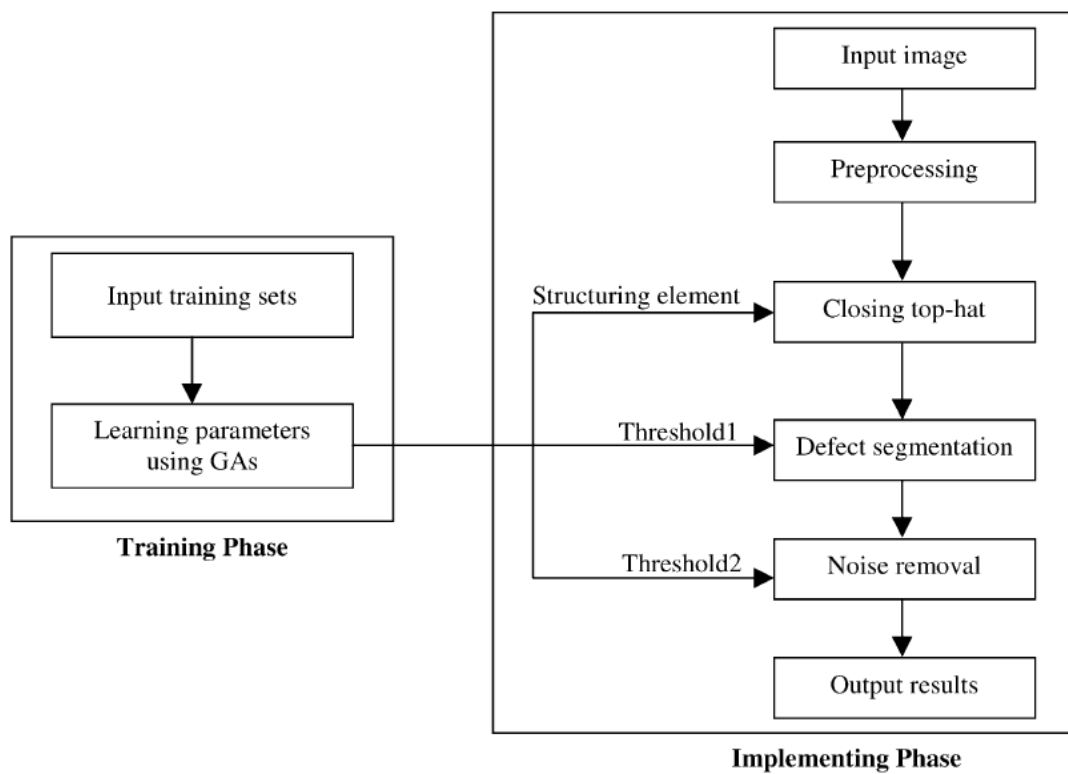


Figure 2.6: The Defect Inspection Procedures

Doege et al [13, 14] presented an optical sensor for contactless online process control of sheet metal forming. This optical sensor consists of a CMOS chip and an integrated digital signal processor. Two LEDs, a lens and other electronic components are included in this sensor. A convex lens is included in the optics in order to enlarge the sheet surface under observation. It is thus possible to exploit the structure of the sheet surface as a characteristic in sheet metal forming. The LED is utilized to illuminate the sheet surface being observed by the CMOS sensor as shown in Figure 2.7.

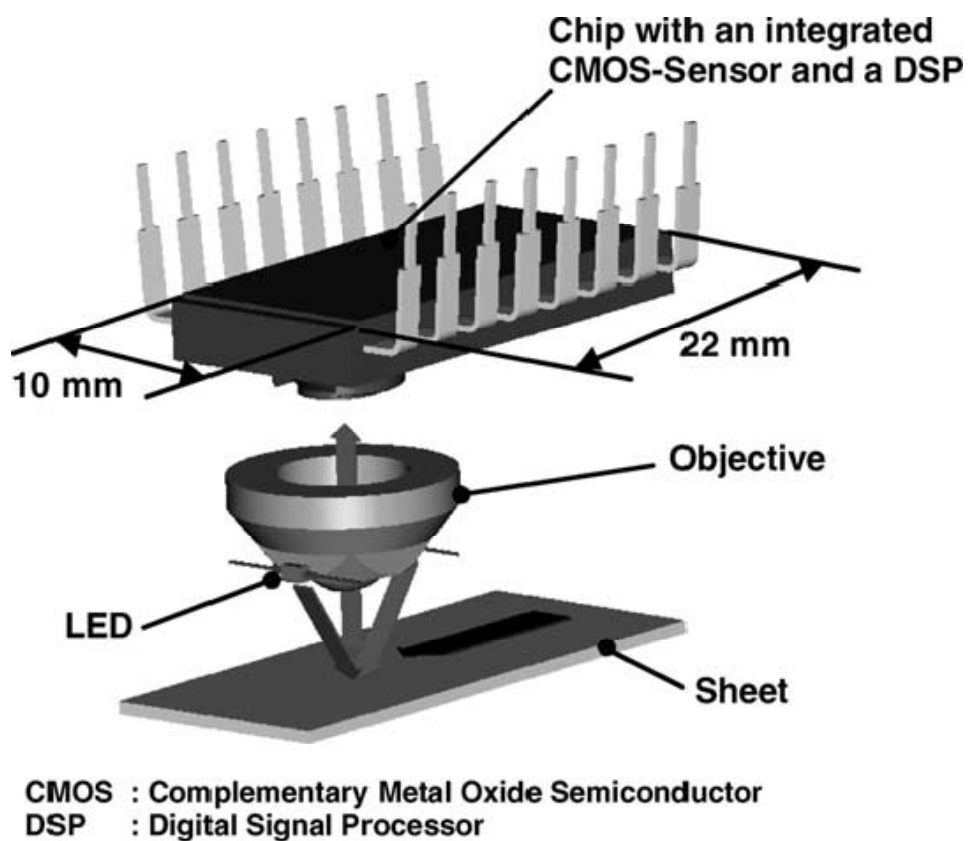


Figure 2.7: Construction Principle of the Optical Sensor

In order to collect significant information of the local material flow from the stamping process, eight optical sensors are fitted in critical positions on the flange area of a die as shown in Figure 2.8. Then, the process boundaries for error-free manufacturing regarding material flow path and velocity are determined. Therefore, the failure boundaries with reference to wrinkling and tearing become apparent.

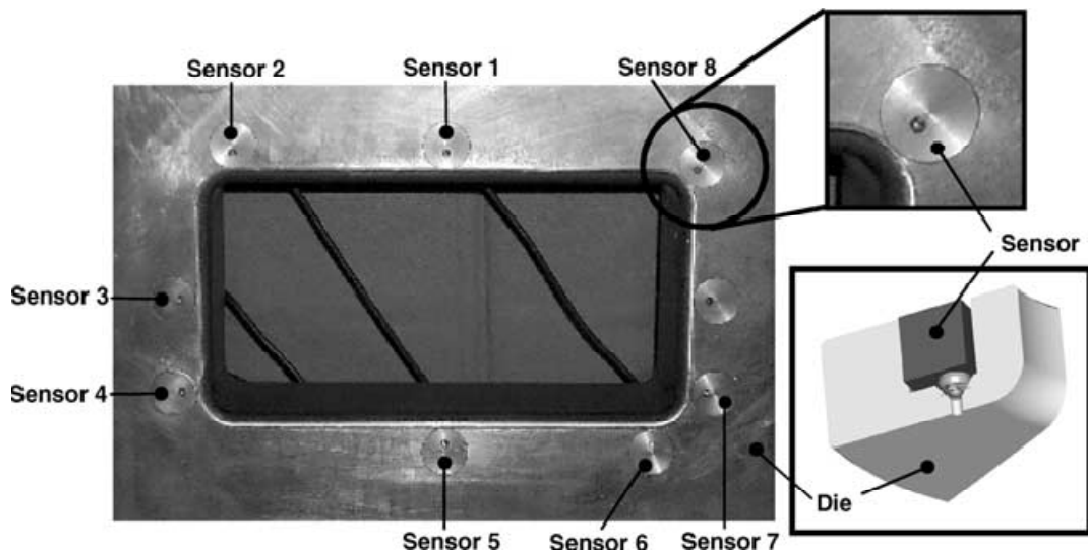


Figure 2.8: Utilization of the Optical Sensor in a Deep Drawing Tool

Fernando, et al [15, 16] presented an online machine vision system for split detection in sheet metal forming process as shown in Figure 2.9 and Figure 2.10. The system employs a CCD camera and an illumination system mounted on a robot. The inspection robot displaces the image acquisition system over the workpieces proceeding from the sheet metal forming line. The recognition, positioning and the later inspection are realized as the workpieces are moving on a conveyor belt. The acquired images are

then restored using a Markov random field model to eliminate spurious features. The split detection is then carried out using a valley detection algorithm. To realize the recognition and to determine the precise position, a two phase appearance-based method is used. In the first phase, the training image set is acquired by moving the image acquisition system around the desired workpiece position. The second phase of recognition and position estimation then is going to find the defect image closest to the training image set obtained in the visual learning process.



Figure 2.9: The Automatic Inspection System for Flow Detection on Car-body Parts

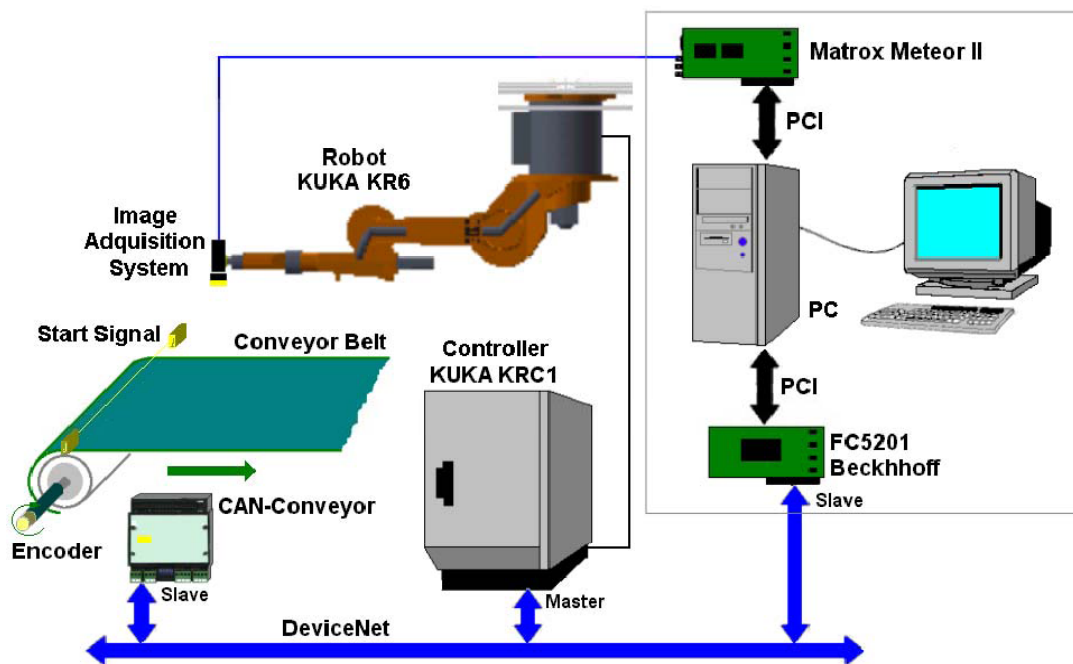


Figure 2.10: The Automatic Inspection System Diagram

However, this online machine vision system is only demonstrated on offline components with simple flat geometry and limited inspection coverage. While splits are more frequent on complicated geometries. Furthermore, the author indicates that the system deployment is also hindered by limited space availability, press-line vibration levels, grease and lubricant contamination, variable ambient luminosity and temperature.

Ng et al [17, 18] presented a diagnosis system based on thermal distribution of the workpiece in order to diagnose sheet metal stamping process. Because most of the plastic deformation energy converts to heat energy during the stamping process, it is possible to detect defects by analyzing thermal energy distribution. The thermal energy distribution can be acquired using an infrared camera as shown in Figure 2.11. The proposed method

consists of three steps as shown in Figure 2.12 to utilize the thermal energy distribution of the workpiece to detect the defects. The first step is to build an ideal strain FEA model of the workpiece based on its thermal energy distribution as shown in Figure 2.13. Next, several thermal images are acquired by an infrared camera right after the stamping to obtain 3D thermal distribution of the workpiece as shown in Figure 2.14. Finally, by comparing the FEA thermal distribution to the experimental thermal distribution, the diagnosis can be carried out.



Figure 2.11: The Thermal Distribution Acquisition System

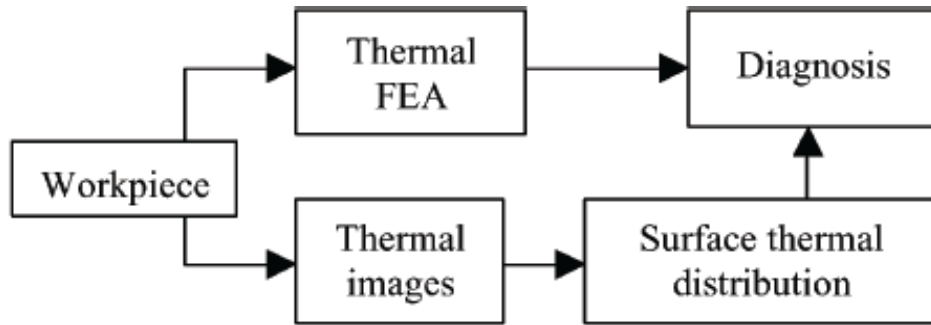


Figure 2.12: Block Diagram of the Thermal Energy Distribution based Diagnosis

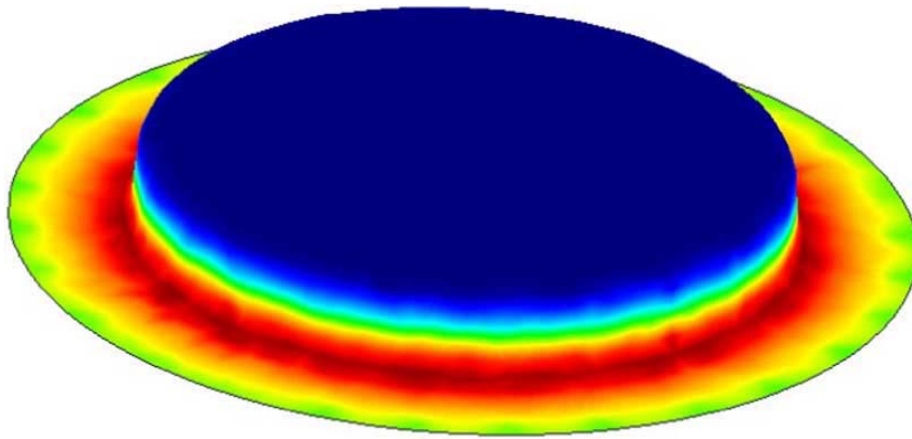


Figure 2.13: Thermal FEA of a Deep Drawing Cup

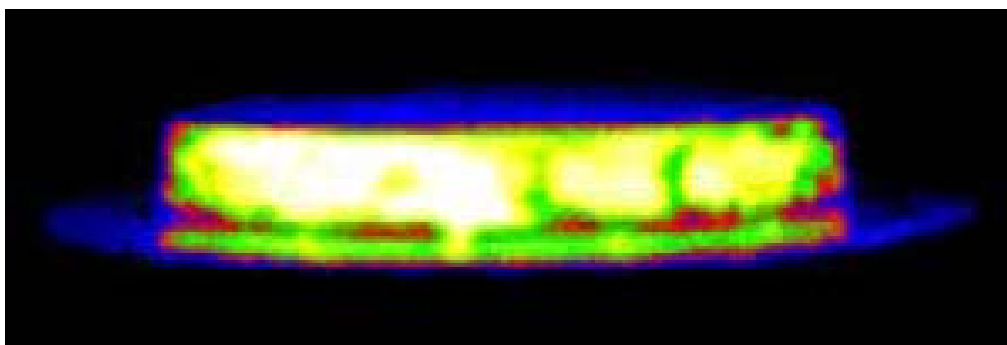


Figure 2.14: Thermal Image of the Deep Drawing Cup

To sum up, the stamping tool oriented contact method basically utilizes contact sensors to measure force, pressure, displacement, and velocity of the tonnage or the draw die. The sensors are either installed on the tonnage to measure controllable stamping parameters or embedded inside the draw to measure critical stamping parameters relative to the quality of the workpiece. By detecting the discontinuous or abnormal force, pressure distribution, or displacement, the defect can be recognized and located.

However, due to the existence of contact sensors inside the draw die, the integrity of the draw die is affected and the mechanical properties of the stamping system are also deviated. To reduce this affection, the size and number of the sensor are constrained and the validation and accuracy of the entire inspection system is also compromised. Furthermore, since only few sample signals for certain points are acquired from the stamping process, a time-consuming signal reconstruction is necessary to build the model for the whole workpiece by using interpolation or FEA. Moreover, all the analysis is performed on the stamping tools instead of the stamping workpiece. Even discontinuous or abnormal signals are detected and analyzed, the specification of the defects are still unknown. All these drawbacks make the stamping tool oriented indirect method only capable for offline stamping improvement, but not suitable for online stamping inspection.

On the contrary, the stamping part oriented non-contact method basically employs non-contact sensors to inspect the workpiece directly. Optical and thermal methods are widely used. After capturing visible or thermal images of the workpiece, image processing algorithms are utilized to directly inspect the workpiece and detect the defects.

The implementation of optical and thermal inspection systems is also convenient compared to contact sensors. Since non-contact sensors are utilized, there is no constraint on sensor location, shape, size and mounting. Therefore, optical and thermal methods are quite suitable for online inspection of stamping process. However, optical method is also hindered by the illumination and reflection problem. The problem in quantifying stamping surface texture using light reflection technique is due to its complicated geometries, contamination or surface wrinkles[19, 20]. Additionally, the visual-surface interrogation methods for highly reflective surfaces are still under development [21, 22].

Finally, the thermal method ends up to be a potential method for online stamping defect inspection applications. First, it's non-contact, non-intrusive and non-destructive that directly inspects the workpiece. By using thermal camera, the thermal energy distribution of the workpiece is easily captured and the defects are apparently detected. Additional, since there is no illumination needed and no reflection problem, the experiment setup is also relatively simple compared to optical systems. Moreover, after digitizing thermal image, advanced image processing algorithms can be employed to perform complicated inspection and analysis in real time manner.

2.2 Thermography Introduction

Thermography is the thermal (Thermo-) mapping (-graphy) of object's surfaces through acquiring its infrared emission. Thermography has a non-contact scanning nature due to its dependence on infrared emission. It also accommodates different materials

because all materials emit or conduct heat. And, the heat conduction is well understood and can be easily simulated.

Thermography is also known as infrared Thermography or thermal imaging that captures the temperature variations using a radiation detector. The captured radiation can be analyzed to retrieve information about the thermal resistance of material surfaces that is used to understand its internal configuration.

From the angle of image processing, Thermography can be classified into two categories: static Thermography and dynamic Thermography. In static Thermography, thermal images are processed on image by image basis. Pixel relationships to its neighbors are important. It focuses on the instantaneous pixel temperature governed by surrounding contributions. In dynamic Thermography, thermal image processing is finished on image sequences. Each pixel is processed individually to its neighbors with no correlations. It focuses on the temperature-time history of each pixel governed by properties of material under inspection.

From the angle of energy excitation, Thermography can also be classified into another two categories: active Thermography and passive Thermography. In active Thermography, an external energy excitation is utilized to excite the test sample thus creating temperature variation between the defective and non-defective areas within the test sample. The excitation can be achieved through optical, electromagnetic, mechanical, thermoelastic, or convection based heating or cooling. In passive Thermography, the un-excited infrared radiation or natural emission is utilized to inspect the sample quality and

detect defects in its structure. The temperature difference between the defect and its surroundings is utilized to distinguish the defect [23].

Since passive Thermography is natural emission based and thus less sensitive to the metallic surfaces specular effect, it is widely used in automotive manufacturing application. It is used in automotive night vision application to locate and identify passing pedestrian and vehicle in low light driving conditions [24]. It is also successfully used for thickness evaluation of automotive fuel tank protective coatings and impurity detection on painted car shells [25, 26].

Thermography has been coupled to thermoelastic and thermoplastic behaviors of solid materials under loading. The thermomechanical coupling [27, 28] with plastic heat dissipation has been investigated for the case of tension loading for fatigue testing. The thermoelastic effect has been applied to predict the stress pattern in roll-bearings [29] and for welded joints [30, 31].

A brief review of thermoelasticity technique is conducted as follows [32]. In forming process, the heat is naturally generated while the metal is being formed [33] due to the metal plastic deformation as described in Equation (2.1).

$$\rho c \dot{T} = \text{div}[k \cdot \text{grad}(T)] + \sigma : \dot{\varepsilon}^p + T \frac{\partial \sigma}{\partial T} : \dot{\varepsilon}^e \quad (2.1)$$

Where, ρ is the density of sheet metal; c is the specific heat; T is the temperature; k is the conductivity; σ, ε are the stress and strain; the superscripts e, p represent the elastic and plastic deformations.

Equation (2.1) can be further simplified to Equation (2.2) by neglecting the elastic strain rate tensor, because only very small part of the elastic deformation is converted into thermal energy. Furthermore, η is added to represent the amount of plastic deformation converted into heat.

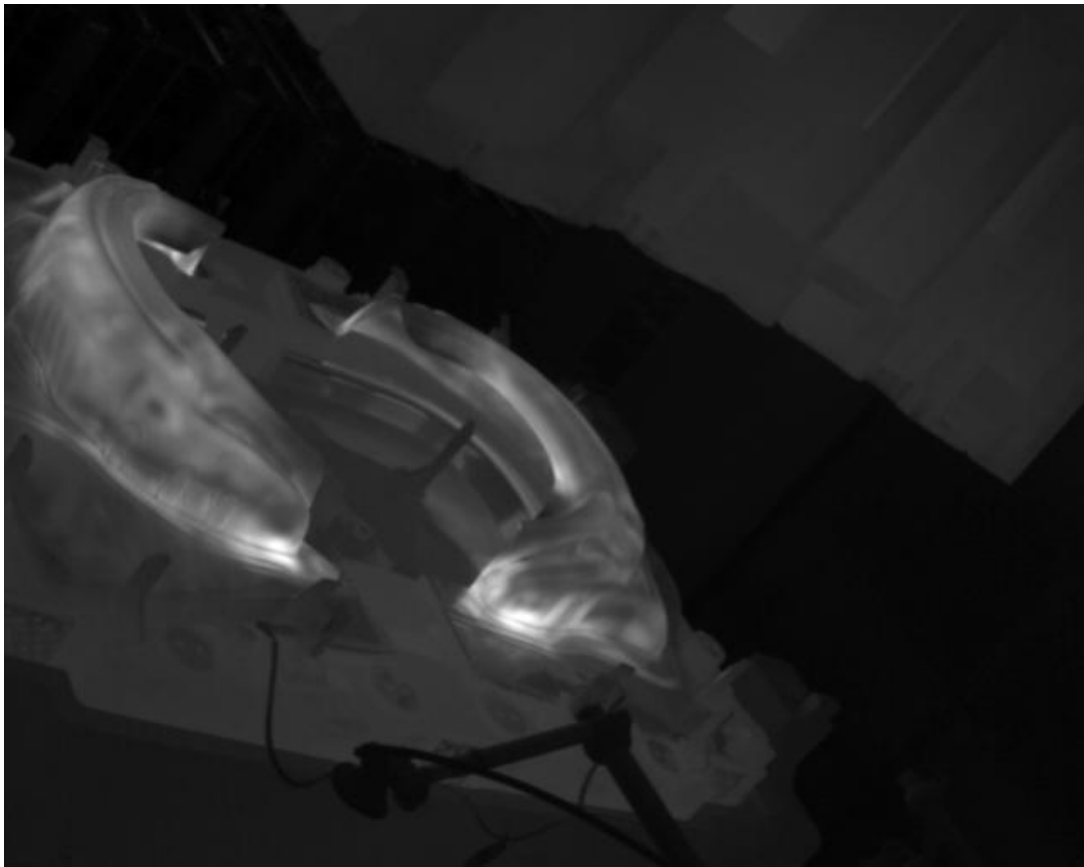
$$\rho c \dot{T} = \text{div}[k \cdot \text{grad}(T)] + \eta \sigma : \dot{\varepsilon}^p \quad (2.2)$$

Online testing results on an OEM stamping line also proved that the stamping die wrinkling pressure can be correlated to the work piece temperature [30, 31, 34].

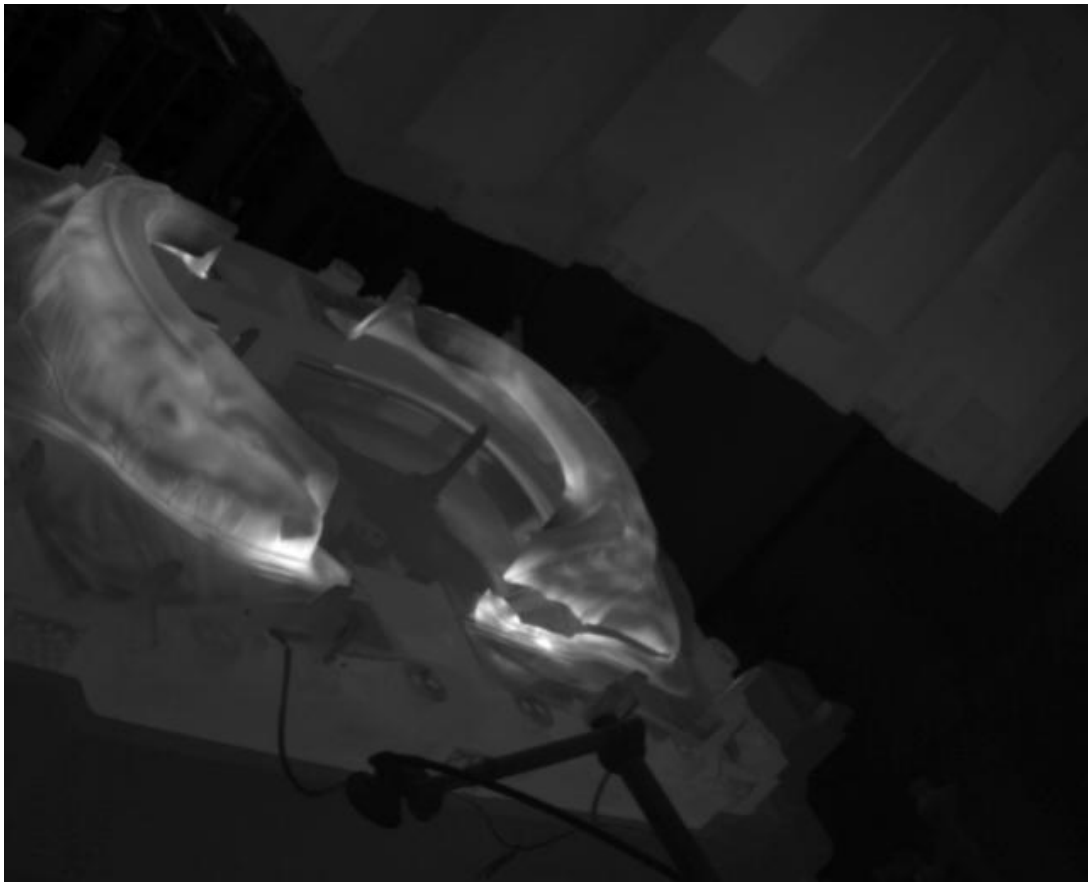
2.3 Thermography in Stamping Split Detection

A passive Thermography based inspection system is developed to detect online automotive stamping splits [35, 36]. This system scans temperature maps of highly reflective steel panels to locate abnormal temperature readings caused by metal splitting. A new image processing routine named “dynamic-template” is developed to retrieve the split’s shape and identify its location. The template is computed through a Region of Interest (ROI) approach with a dynamic threshold accounting for spatial deviations. The developed system is implemented on an automotive press line and the online thermal acquisitions are processed to illustrate performance and success. Different split shapes and sizes are detected under actual operating conditions.

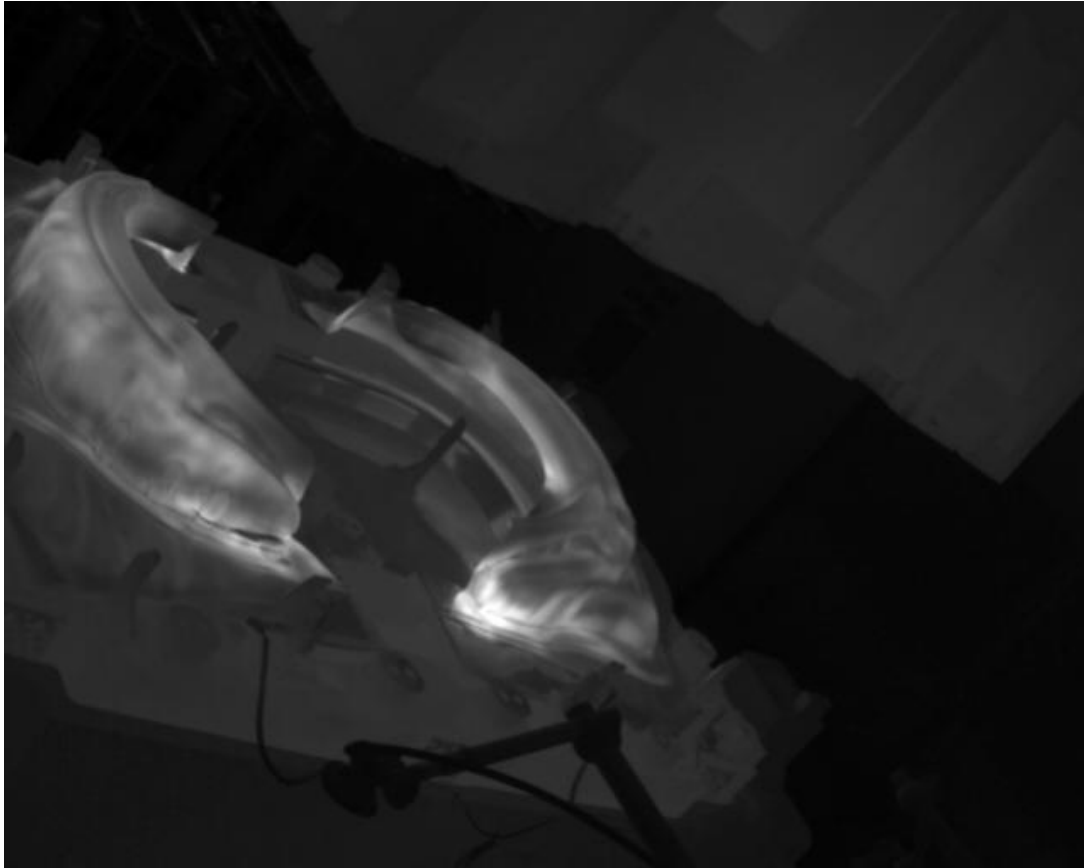
A cooled thermal detector (FLIR Phoenix DTS, FLIR Systems Inc., MA) is installed on an automotive press line to acquire the stamping metal temperature maps. The thermal detector is InSb (Indium Antimonide) based with spatial resolution 640×512 , acquisition frame rate up to 120Hz, and Minimum Resolvable Temperature Difference (MRTD) in the order of 100mK. Figure 2.15 displays thermal images of three stamping samples: split-free, major split and minor split.



(a)



(b)



(c)

Figure 2.15: Sample Thermal Images (a) Split-free; (b) Major Split; (c) Minor Split

2.3.1 Template Preprocessing

The template preprocessing is utilized to create the template ROI image that describes the stamping part's boundary and shape. The thermal image of split-free part shown in Figure 2.15 (a) is utilized as the template image to create the template ROI for further processing.

First, the raw template image is convolved with a 5×5 Gaussian kernel to reduce random spikes and noises as described mathematically in Equation 2.3.

$$G(x, y) = \frac{1}{2\pi\sigma^2} e^{-\frac{x^2+y^2}{2\sigma^2}}$$

$$S(x, y) = I(x, y) * G(x, y)$$
(2.3)

Where $G(x, y)$ is the Gaussian kernel; $I(x, y)$ is the raw image; and $S(x, y)$ is the convolution of $G(x, y)$ and $I(x, y)$.

After that, a thresholding process is utilized to eliminate the background and recognize the shape of the part as shown in Figure 2.16. The thresholding criterion is mathematically described in Equation (2.4). It has been applied successfully for detecting dynamic and static discrete features such as dents and seeds in thermal images [37].

$$|T_{pix} - T_{avg}| \geq \eta \cdot \sigma_{surr(x,y)}$$
(2.4)

Where T_{pix} is the temperature of central pixel in a kernel; T_{avg} is average temperature of the kernel; η is a scaling factor dependant on the Signal-to-noise Ratio (SNR); and $\sigma_{surr(x,y)}$ is the standard deviation of the kernel centered at (x, y) .



Figure 2.16: Template Image after Thresholding

Next, a region detection process based on flood fill algorithm is utilized to detect localized regions and eliminate small regions as shown in Figure 2.17. Later on, morphological operations are utilized to fill and remove “pepper and salt” like holes to create the template ROI image as shown in Figure 2.18.

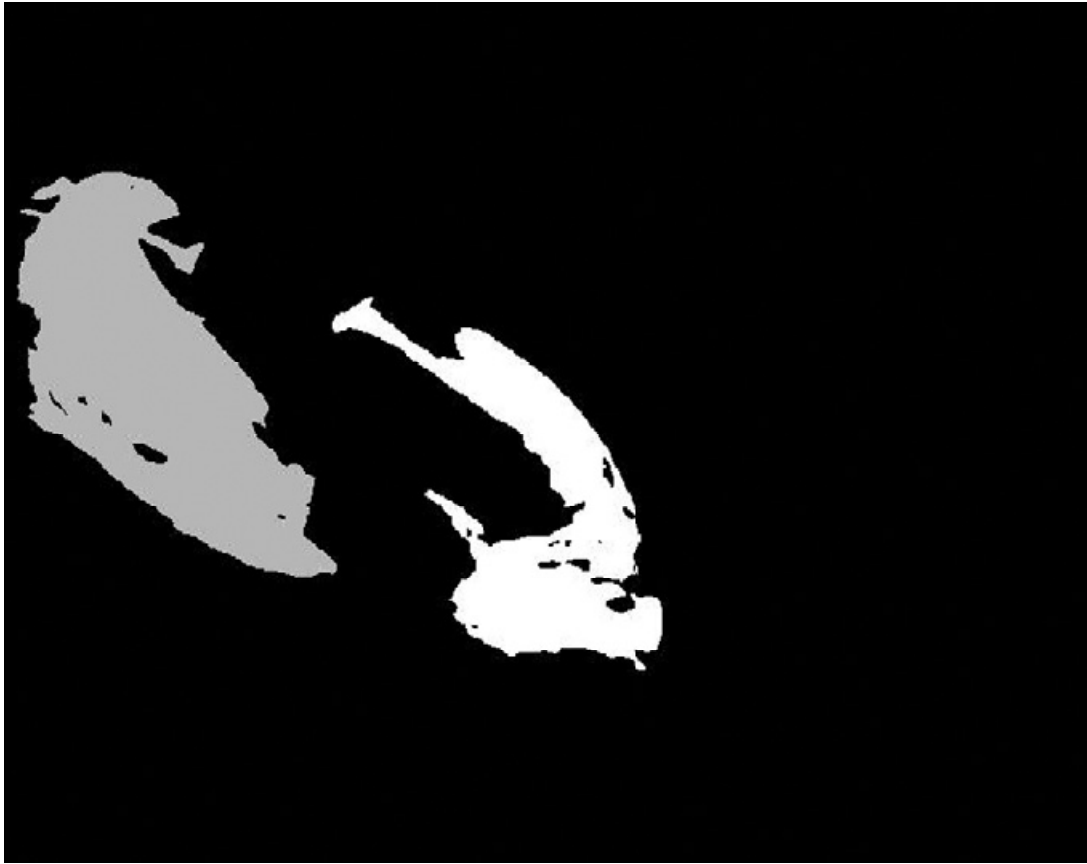


Figure 2.17: Template Image after Region Detection

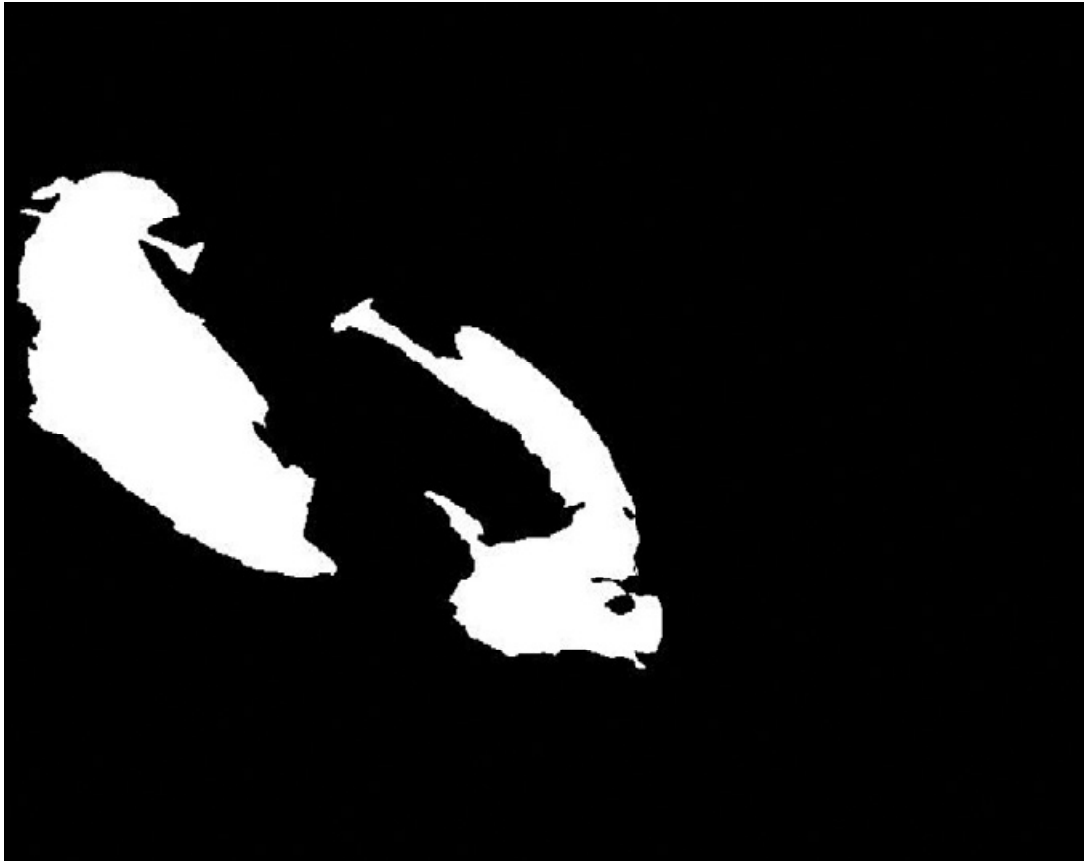


Figure 2.18: Template ROI Image

2.3.2 Split Detection

The template ROI image is utilized to compare with the split image for split detection. Figure 2.19 illustrates the flow chart of the split detection sequence. First, trigger detection is applied on the raw image in the template ROI to calculate the average temperature. When the average temperature is over a threshold value, the punch is up and the split detection window is open for detection.

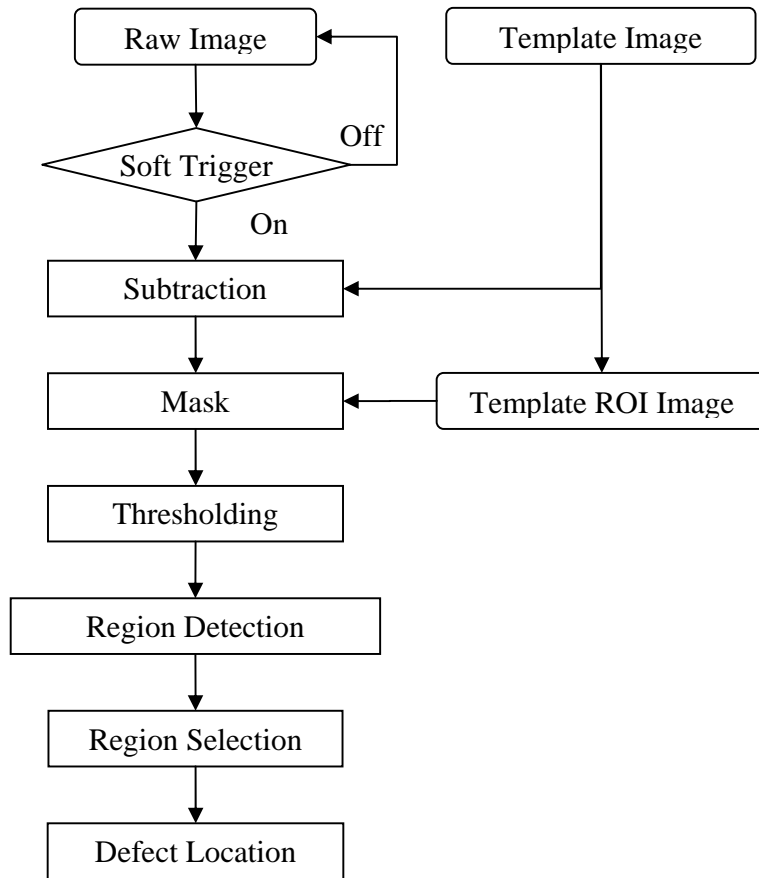


Figure 2.19: Flow Chart of Split Detection

Then, a subtraction is performed between the raw image and the template ROI image to remove split-free regions as shown in Figure 2.20.

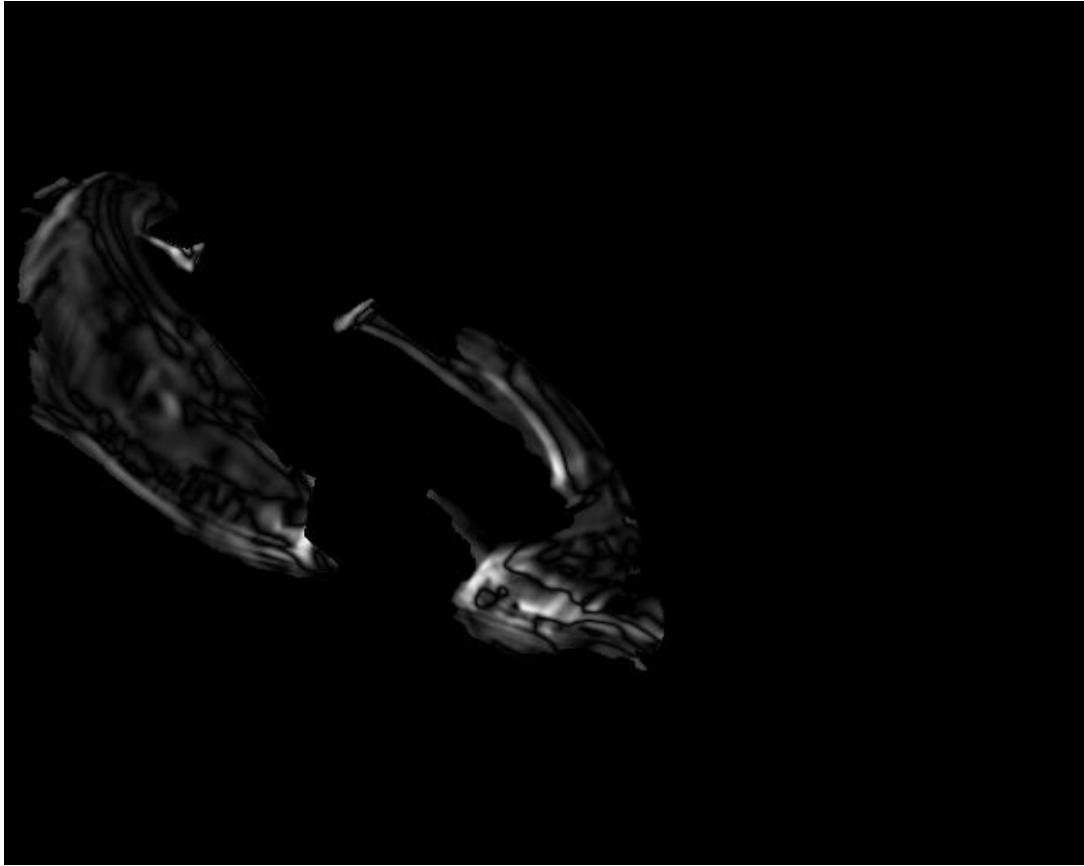


Figure 2.20: Contrast in ROI between Raw Image and Template Image

Next, the split detection algorithm first employs a thresholding to highlight the regions with large contrast and then utilizes morphological operations like erosion and dilation to close slightly separated regions and indicates split regions shown in Figure 2.21.

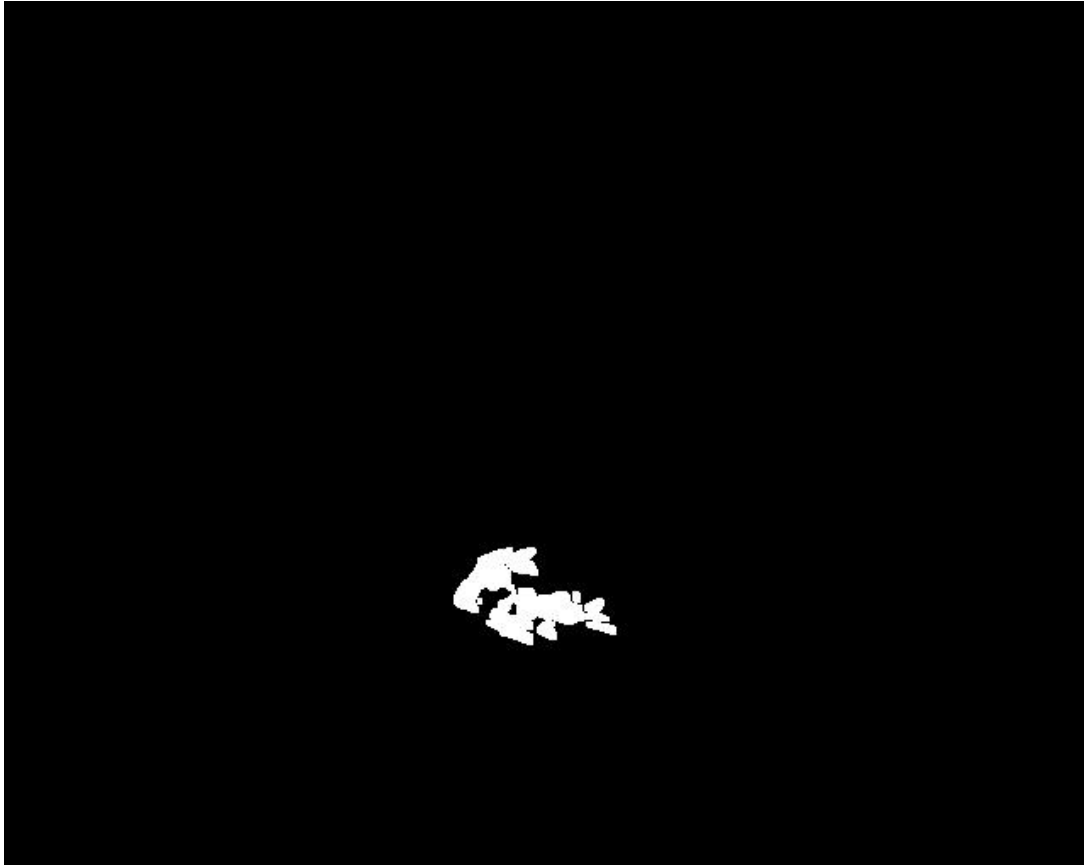


Figure 2.21: Large Contrast Regions in Template ROI

Finally, the specifications of the split region are investigated and its geometry information including centroid, location and size is calculated using Equation (2.5):

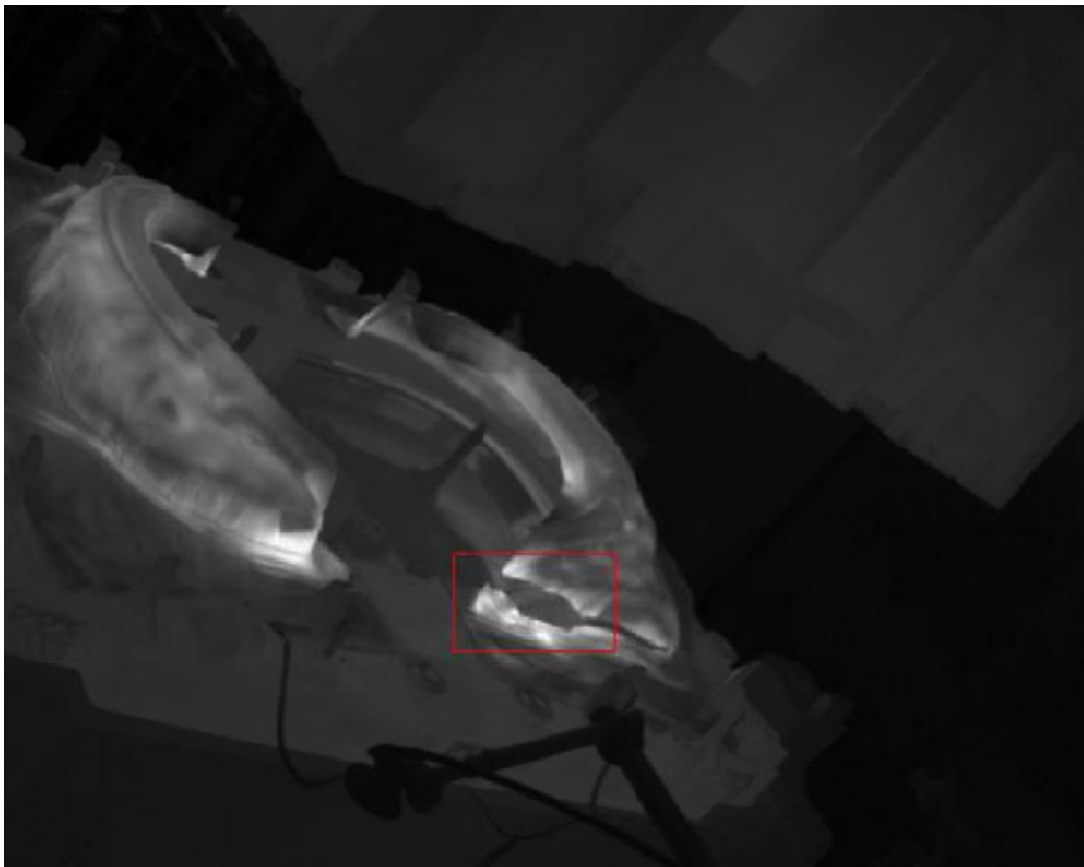
$$M_{pq} = \sum_y \sum_x x^p y^q I(x, y)$$

$$X_c = \frac{m_{10}}{m_{00}}, Y_c = \frac{m_{01}}{m_{00}}$$

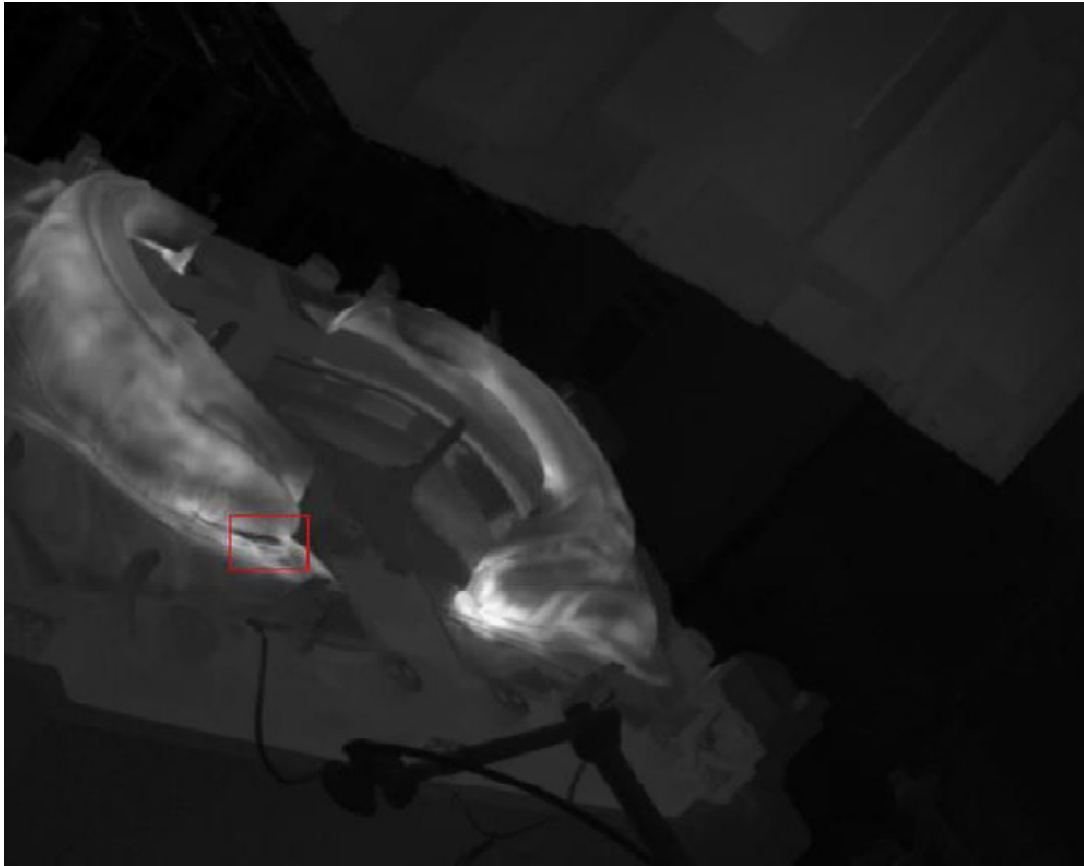
(2.5)

Where $I(x, y)$ is the pixel intensity at location (x, y) ; m_{00} is the summation of the intensity of all pixels; m_{10} is the summation of the x moment of all pixels; m_{01} is the summation of the y moment of all pixels; (X_c, Y_c) is the centroid location.

Figure 2.22 displays the results after running Figure 2.15(b) and Figure 2.15(c) through the above discussed processing sequence. Both of the major split and minor split with different shape and size are successfully detected.



(a)



(b)

Figure 2.22: Split Detection Results: (a) Major Split; (b) Minor Split

The above described split detection routines are further integrated into Graphical User Interface (GUI) to enable convenient setting, control and display for online application as shown in Figure 2.23.

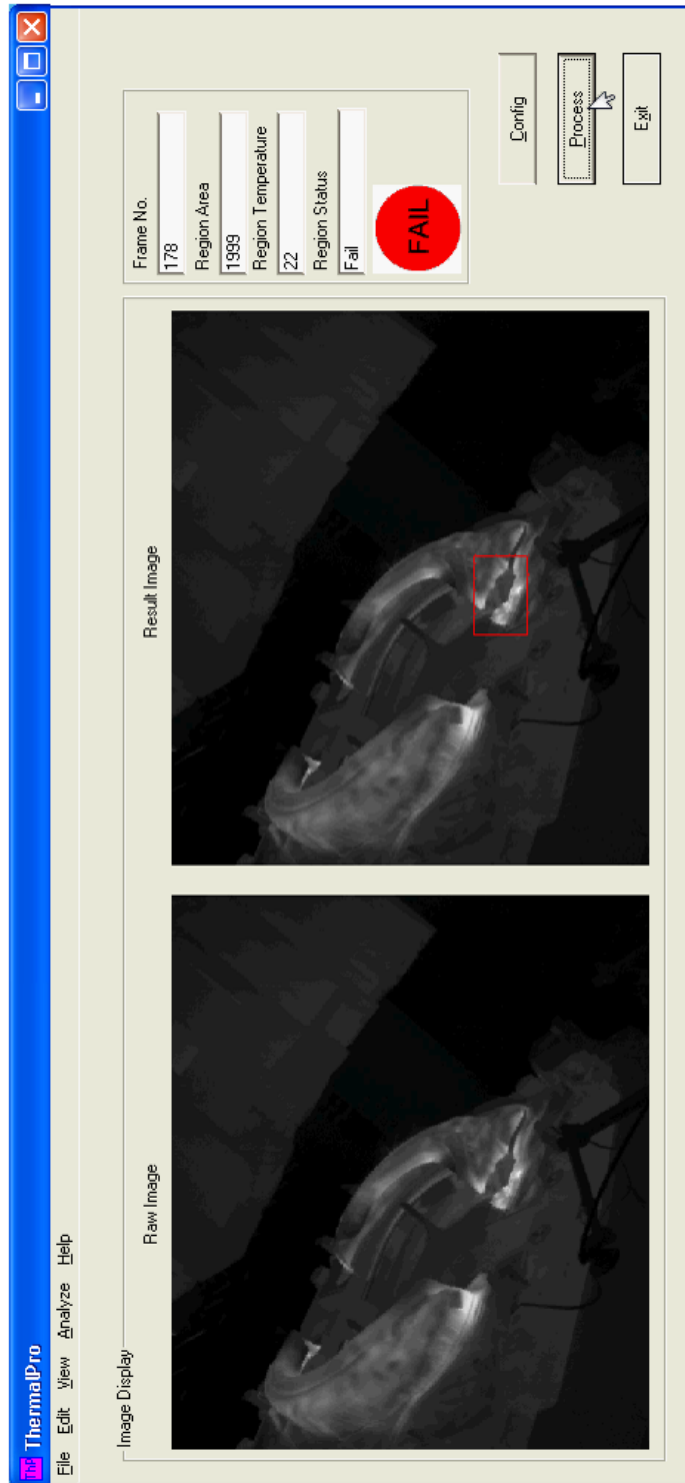


Figure 2.23: Graphical User Interface of Stamping Split Detection Routines

2.4 Thermography Limitations and Image Fusion

Although the emission-based passive Thermography is effective in split detection application, surrounding heat contribution and heat diffusion affects are not trivial. General challenges in Thermography include its sensitivity to emissivity variations and sensitivity to the surrounding thermal contribution. Surrounding heat contribution and heat diffusion affect the sensitivity and spatial resolution of the thermal imaging, especially for geometrically complex surfaces. The heat diffusion across the surface through conduction and heat losses to the surroundings through convection blur the thermal imagery and severely decrease the quality of thermal acquisitions. Therefore, a single Thermography based split detection system is not reliable enough to meet the tough application requirements in harsh industrial environment.

To offset the limitations of Thermography, another image source from a visible channel is utilized to be fused with the thermal image to enhance features of the stamping part from both thermal and visible domains. The thermal image contains temperature maps related to critical strains to locate abnormal temperature readings indicative of high local wrinkling pressure. At the mean time, the visible image provides higher spatial resolution and more detailed information about the complex geometry of the stamping part.

Therefore, a thermal and visible image fusion based inspection system for stamping process control is proposed and is to be presented in the next chapter to take good advantage of both thermal and visible channels for online stamping split detection.

2.5 Summary

This chapter first presents a literature review of stamping process control including contact method and non-contact method. Through summarizing the advantages and disadvantages of each method, Thermography based method is introduced and relative mathematical model is also presented to show the capability of Thermography in stamping split detection. After that, a stamping split detection application is investigated and demonstrated with technical details. Finally, the limitations of Thermography are discussed. A solution to offset these limitations using image fusion of thermal and visible images is proposed and is to be presented in the next chapter.

CHAPTER THREE

IMAGE FUSION

3.1 Image Fusion Introduction

Image fusion is the process of combining relevant information from two or more images into a single image [38] that is more informative than any of the original images. Image fusion can be categorized into three categories: pixel level, feature level, and decision level [39].

In pixel level fusion, the input images are fused pixel by pixel followed by the information extraction. To implement the pixel level fusion, arithmetic operations are widely used in time domain and frequency transformations are used in frequency domain.

The main goal of pixel level fusion is to enhance the raw input images and provide an output image with more useful information than either input image. Pixel level fusion is effective for high quality raw images but not suitable for images with unbalanced quality level because information from one physical channel might be impeded by the other. The scheme of pixel level fusion is shown in Figure 3.1.

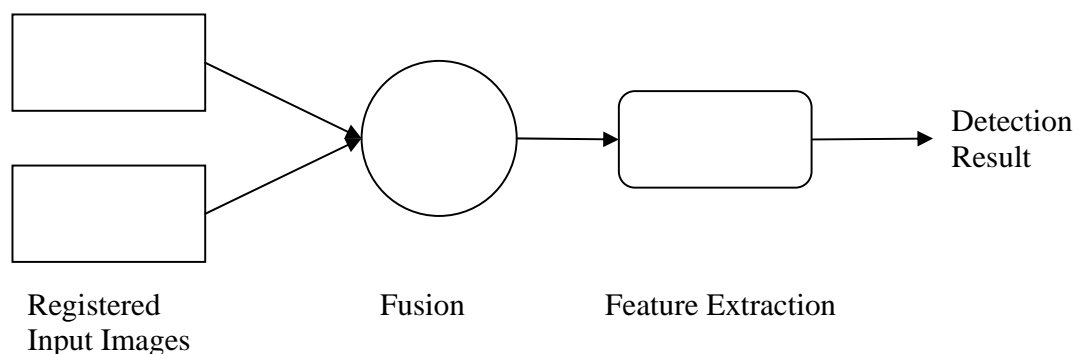


Figure 3.1: Scheme of Pixel Level Fusion

In feature level fusion, the information is extracted from each input image separately and then fused based on features from input images. The feature detection is typically achieved through edge enhancement algorithms, artificial neural networks, and knowledge based approaches. Feature level fusion is effective for raw images with unbalanced quality level. It requires a feature-extraction algorithm effective for both physical channels. The scheme of feature level fusion is shown in Figure 3.2.

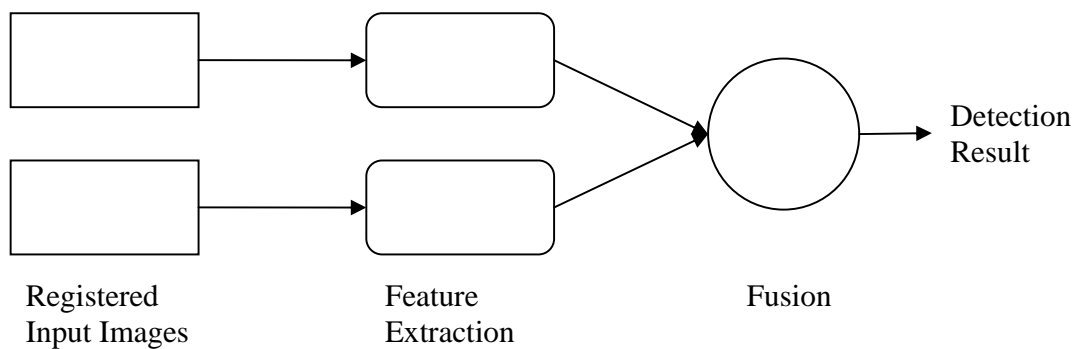


Figure 3.2: Scheme of Feature Level Fusion

In decision level fusion, the information is extracted from each input image separately and then decisions are made for each input channel. Finally, those decisions are fused to form the final decision. Decision level fusion is effective for complicated systems with multiple true or false decisions but not suitable for general applications. The scheme of decision level fusion is shown in Figure 3.3.

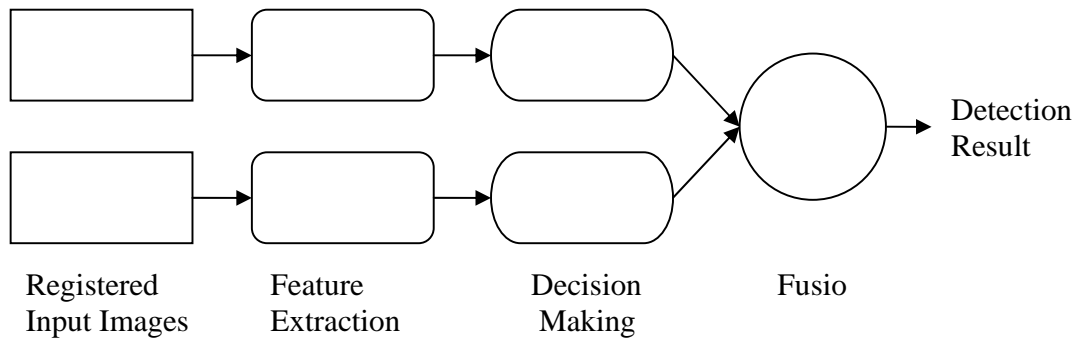


Figure 3.3: Scheme of Decision Level Fusion

Based on the fusion mechanism, decision level and feature level fusions are high level fusions that require more complex algorithms and more intensive computation. Considering the 30Hz image frame rate of online split detection, they are not efficient enough for real time application. On the contrary, pixel level fusion is the lowest level fusion that fuses raw images from different physical channels pixel by pixel to enhance the features not complete in either channel. Therefore, it requires less processing time and is found suitable for time critical image fusion applications.

This dissertation focuses on pixel level grayscale image fusion techniques. And original images for image fusion have the same resolution and have been aligned and registered from hardware level.

3.2 Literature Review of Image Fusion

Pixel level image fusion can be implemented by two methods: arithmetic operations and Multi-scale Decomposition (MSD).

Typical arithmetic operations include weighted average and comparison.

In weighted average, the fusion is accomplished using weights assigned to each original image. The weight may be fixed or variable based on specific applications as described in Equation 3.1

$$\begin{aligned}
 I_F(x, y) &= \omega_T(x, y) \times I_T(x, y) + \omega_V(x, y) \times I_V(x, y) \\
 \omega_T(x, y) + \omega_V(x, y) &= 1
 \end{aligned}
 \tag{3.1}$$

Where, $I(x, y)$ is the pixel intensity at location (x, y) ; $\omega(x, y)$ is the weight at location (x, y) ; the subscripts F, T, V represent the fused, thermal and visible image.

In comparison based fusion, the maximum or minimum intensity at each pixel location is selected from input images for the output image as described in Equation 3.2.

$$\begin{aligned}
 I_F(x, y) &= \text{Max}(I_T(x, y), I_V(x, y)) \\
 I_F(x, y) &= \text{Min}(I_T(x, y), I_V(x, y))
 \end{aligned}
 \tag{3.2}$$

Liu et al [40] presented an adaptive weighted image fusion rule based on image kernels. A convolution is first employed using a 3×3 image kernel as described in Equation 3.3.

$$\begin{aligned}
C(x, y) &= \sum_{i=-1}^{i=1} \sum_{j=-1}^{j=1} K(i+1, j+1)I(x+i, y+j) \\
K &= \begin{bmatrix} \frac{1}{16} & \frac{1}{16} & \frac{1}{16} \\ \frac{1}{16} & \frac{1}{2} & \frac{1}{16} \\ \frac{1}{16} & \frac{1}{16} & \frac{1}{16} \end{bmatrix} \\
\sum_{i=-1}^{i=1} \sum_{j=-1}^{j=1} K(i+1, j+1) &= 1
\end{aligned} \tag{3.3}$$

And then the adaptive weight coefficients are calculated using the convolution value of both thermal kernel and visible kernel as described in Equation 3.4.

$$\begin{aligned}
\omega_T(x, y) &= \frac{C_T(x, y)}{C_T(x, y) + C_V(x, y)} \\
\omega_V(x, y) &= 1 - \omega_T(x, y)
\end{aligned} \tag{3.4}$$

A more complex image fusion rule uses Equation 3.5 to calculate the weight coefficients based on the same kernel strategy. The match measure $M_{TV}(x, y)$ is a normalized correlation averaged over the image kernel centered at (x, y) . The α is a user defined threshold used to adjust the fusion rule according to specific application.

$$\begin{cases} \omega_T(x, y) = 0, \omega_V(x, y) = 1 & M_{TV}(x, y) < \alpha \\ \omega_T(x, y) = (1 - \left(\frac{1 - M_{TV}(x, y)}{1 - \alpha}\right))/2 & M_{TV}(x, y) > \alpha \\ \omega_V(x, y) = 1 - \omega_T(x, y) & M_{TV}(x, y) = \alpha \end{cases}$$

$$M_{TV}(x, y) = \frac{2 \sum_{i=-1}^{i=1} \sum_{j=-1}^{j=1} K(i+1, j+1) I_T(x+i, y+j) I_V(x+i, y+j)}{C_T^2(x, y) + C_V^2(x, y)}$$

(3.5)

The local variance can also be used to determine the adaptive weight coefficients of image fusion to highlight the unnatural objects against their neighborhood as described in Equation 3.6 [41, 42]. For thermal image, object either warmer or cooler than the background should be emphasized. And for visible image, objects having sharp edges need to be assigned larger weight coefficient.

$$\omega_T(x, y) = \left[\frac{1}{X \times Y} \sum_{i \in X, j \in Y} (I(x+i, y+j) - \bar{I}(x+i, y+j))^2 \right]^\alpha$$

$$\omega_V(x, y) = 1 - \omega_T(x, y)$$

(3.6)

Where $M \times N$ is the kernel size; $\bar{I}(x, y)$ is the kernel average centered at (x, y) .

In MSD [43], a Multi-scale Transform (MST) is applied on the original images to construct a composite representation followed by down-sampling. Then an image fusion rule is applied to fuse the images in the MST format. After that, an Inverse Multi-scale

Transform (IMST) is applied to create the fused image. The system block diagram of MST based image fusion is shown in Figure 3.4.

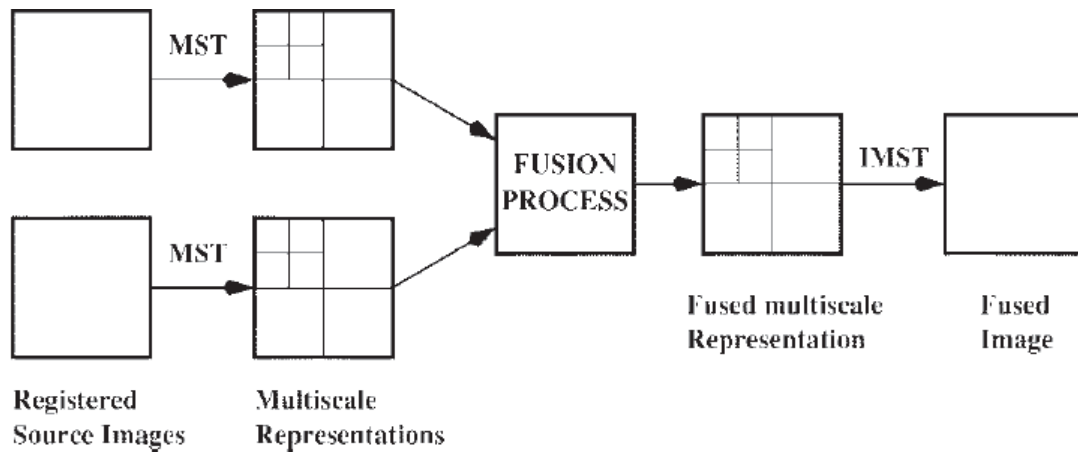


Figure 3.4: Scheme of MST based Image Fusion

Most widely used MSTs in image fusion are Pyramid Transform (PT) and Discrete Wavelet Transform (DWT) [44].

The PT down-samples the original images to represent them in different scales and then uses the fusion rules discussed in arithmetic operation section to obtain the fusion coefficients and finish the fusion. Finally an inverse PT is employed to obtain the fused image. Laplacian Pyramid is the most commonly used PT in image fusion [43, 45]. In each level of the Laplacian Pyramid, four basic procedures are conducted recursively: blurring (low-pass filtering), downsampling (size reduction), interpolation (size expansion) and differencing (subtraction).

In DWT [41, 46-48], a wavelet transform is applied on both original images. The DWT first horizontally blurs and downsamples each row of the image $I(x, y)$ using a low pass filter L and a high pass filter H to create coefficient matrices, $I_L(x, y)$ and $I_H(x, y)$. Then, it vertically blurs and downsamples each column of $I_L(x, y)$ and $I_H(x, y)$ to create four coefficient matrices: $I_{LL}(x, y)$, $I_{LH}(x, y)$, $I_{HL}(x, y)$ and $I_{HH}(x, y)$. After that, one level of DWT is accomplished and follow the same procedure to obtain next level of DWT. $I_{LL}(x, y)$ is a blurred and downsampled version of the original image $I(x, y)$. $I_{LH}(x, y)$, $I_{HL}(x, y)$ and $I_{HH}(x, y)$ are detail subimages representing the horizontal, vertical and diagonal directions of the original image $I(x, y)$. Figure 3.5 shows an example of one level of DWT. Next, an image fusion decision criterion is generated based on the wavelet coefficients. Finally, an inverse wavelet transform is used to generate the fused image.

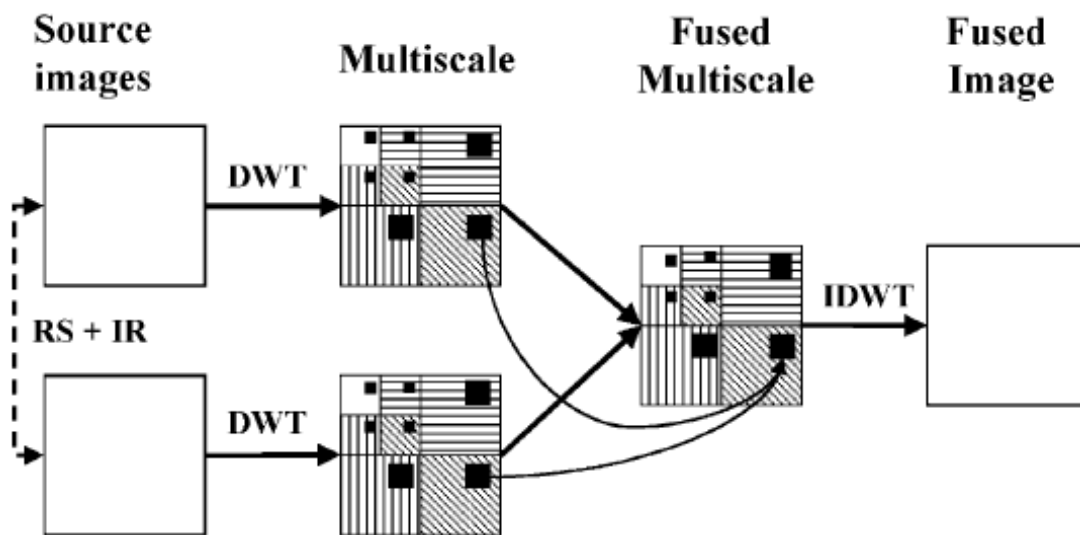


Figure 3.5: Scheme of Generic DWT Fusion

3.3 Image Fusion in Night Vision

An image fusion application research in night vision has been accomplished to track pedestrians and vehicles and then increase the driving safety in night or low light driving scenarios [24, 49].

In order to increase night-time driving safety, most automotive Original Equipment Manufacturers (OEMs) have introduced different techniques to provide night vision capabilities to their vehicles. Such techniques can be classified into [50]: laser based system, Far-infrared (FIR) passive system, and Near-infrared (NIR) active system. The laser based and NIR system are limited in 500 feet range and don't offer classifying ability for detected objects. While, the passive FIR system can provide up to 5000 feet range with high resolution for thermal emitting (warm) objects. However, FIR system only detects thermal emitting (warm) objects but missing reflective (cold) objects such as head lamps and road signs. This might influence the drivers' awareness of heavily clothed pedestrians, traffic signs and other obstacles. Therefore, FIR modules combined with visible cameras provides an enhanced solution for tracking vehicles, pedestrians and non-emitting road features.

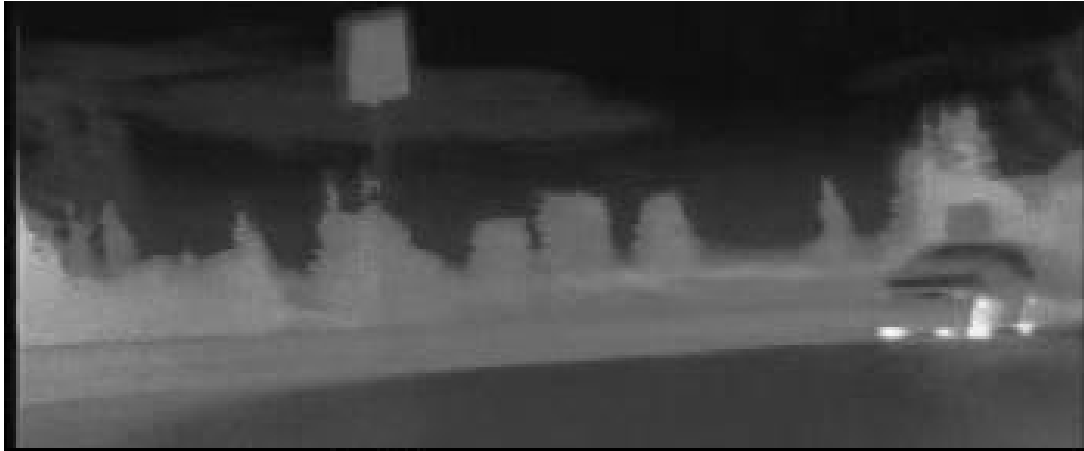
An investigation is accomplished based on fusion of Long-Wave Infrared (LWIR) with wavelength from 7.5 to 13.5 μm and visible light with wavelength from 0.38 to 0.78 μm to retrieve the shape of emitting and reflective objects in night or low light driving scenarios. A pixel level fusion algorithm and a feature level fusion algorithm are developed and applied on two driving scenarios, a passing vehicle scenario and an approaching vehicle scenario, to quantify their strengths and weaknesses for dynamic

scenarios. The image fusion algorithms coupled with object tracking routines provide complete detection of both reflective and emitting objects with good shape and orientation extraction.

The input image sequences are from two channels, LWIR and visible. The LWIR thermal image sequence is acquired from an uncooled, micro-bolometric array with 352×144 resolution and 30 Hz frame rate (PathFindIR, FLIR Systems Inc, MA). The visible image sequence is acquired from a Charged Coupled Device (CCD) detector with the same resolution and frame rate.

Two important scenarios for night time driving, a passing vehicle scenario and an approaching vehicle scenario, are selected and displayed in Figure 3.6 and Figure 3.7 in both thermal and visible perspectives. In Figure 3.6 (a) and Figure 3.7 (a), the thermal images highlight the vehicle tires while missing head lamps and traffic signs. While, in Figure 3.6 (b) and Figure 3.7 (b), the visible images show the traffic sign and the lane paint markings but saturated by bright glare of the approaching vehicle.

These two night vision acquisitions are selected due to their dynamic nature with moving vehicle on varying backgrounds and speed. Also, the features encountered are pedestrians, vehicles and surroundings with different shapes and thermal signatures. All these features help in challenging the pixel level and feature level image fusion algorithms in testing the feature extraction accuracy and reliability.



(a)



(b)

Figure 3.6: Passing Vehicle Scenario: (a) Thermal Image; (b) Visible Image



(a)



(b)

Figure 3.7: Approaching Vehicle Scenario: (a) Thermal Image; (b) Visible Image

3.3.1 Pixel Level Image Fusion

The pixel level fusion algorithm is based on an adaptive weighted average algorithm that combines the thermal and visible images to synthesize a fused image. It is utilized to detect both emitting and reflective objects with good shape retrieval, orientation prediction and object recognition. The pixel level fusion algorithm is composed of three steps as follow and its flow chart is shown in Figure 3.8:

- (1) Preprocessing that includes intensity stretching based on 8-bit grayscale and Gaussian convolution for smoothing;
- (2) Image fusion that utilizes adaptive weighted average algorithm;
- (3) Tracking algorithm based on seed initiation and growth using morphological operations.

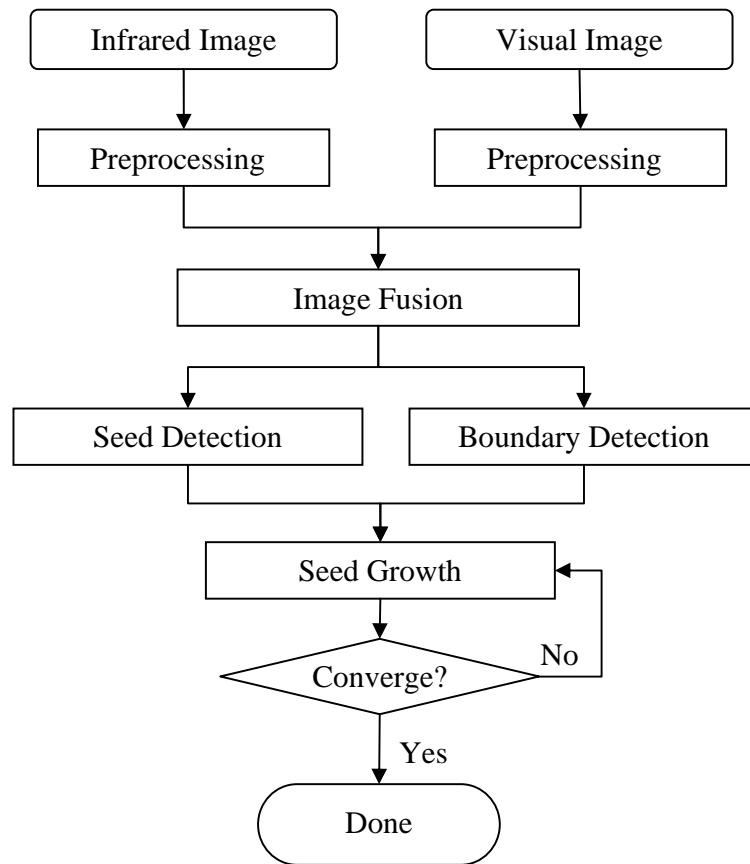


Figure 3.8: Flow Chart of Pixel Level Image Fusion Algorithm

Preprocessing

The preprocessing is applied on both thermal and visible images to enhance the raw images and prepare them for the fusion. The normalization process ensures the thermal and visible images in the same intensity range by stretching the raw pixel intensity range to the range of 0 to 255 based on 8-bit grayscale as described in Equation 3.7.

$$I(x, y) = \frac{I(x, y) - I_{min}}{I_{max} - I_{min}} \times 255 \quad (3.7)$$

Where $I(x, y)$ is the pixel intensity at location (x, y) ; I_{min} and I_{max} are the minimum and maximum pixel intensity in the image, respectively.

The next smoothing process reduces the background noise level for further processing. A Gaussian kernel is convolved with the raw image to attenuate the noises as described in Equations 3.8.

$$G(x, y) = \frac{1}{2\pi\sigma^2} e^{-\frac{x^2+y^2}{2\sigma^2}}$$

$$S(x, y) = I(x, y) * G(x, y) \quad (3.8)$$

Where $G(x, y)$ is the Gaussian kernel; $I(x, y)$ is the pixel intensity at location (m, n) ; $I(x, y)$ is the raw image, and $S(x, y)$ is the convolution of $G(x, y)$ and $I(x, y)$.

Pixel Level Fusion Algorithm

The pixel level image fusion combines the features of both emitting and reflective objects from the thermal and the visible images. An adaptive weighted average algorithm is developed as described in Equation 3.9.

$$I_F(x, y) = \frac{\alpha \times I_T(x, y) \times I_V(x, y)}{I_T^2(x, y) + I_V^2(x, y)} \quad (3.9)$$

Where, $I(x, y)$ is the pixel intensity at location (x, y) ; the subscripts F, T, V represent the fused, thermal and visible image, respectively. α is the coefficient to optimize the fusion result. For current sample images, α is found to be 2.

The pixel level fusion result image is shown in Figure 3.9.



Figure 3.9: Pixel Level Fusion Result Image of Passing Vehicle Scenario

Tracking Algorithm

The tracking algorithm contains a sequence of image processing subroutines implemented to trace the feature objects. The tracking sequence is based on seed initiation and growth in addition to object boundary detection described in [24].

The seed initiation is done through a double weighted thresholding based on the histogram of the fused image as shown in Figure 3.10. The pseudo code of the weighted double thresholding algorithm is shown below.

```
Initialize threshold_value to intensity average of the ROI  
while <threshold_value not convergence>{  
for <each pixel>{  
calculate the average of pixels less than threshold_value, average_low;  
calculate the average of pixels not less than threshold_value, average_high;}  
threshold_value = (average_low + average_high * weight)/(weight + 1);}
```

The threshold value from the histogram in Figure 3.10 is found to be 149. The result image after the double thresholding is displayed in Figure 3.11. The weighted double thresholding eliminates the temporal and spatial background and is found effective for the fused image.

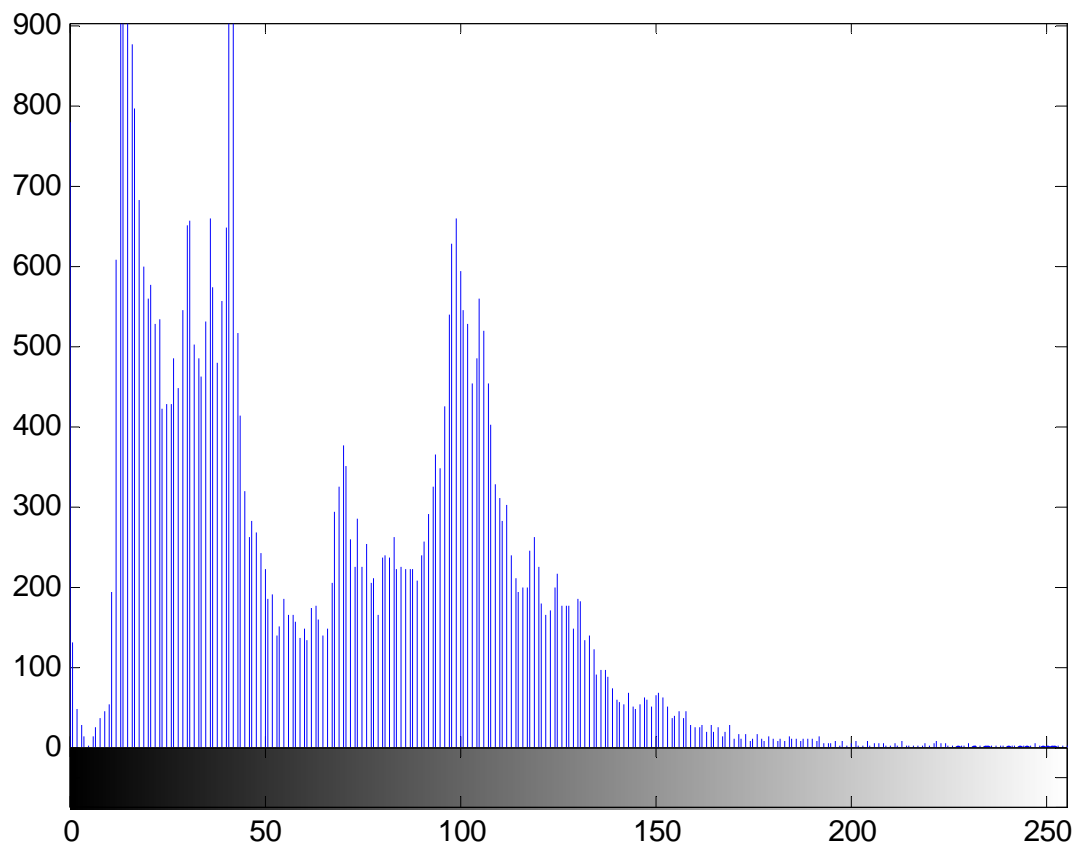


Figure 3.10: Histogram of Pixel Level Fusion Result Image of Passing Vehicle Scenario

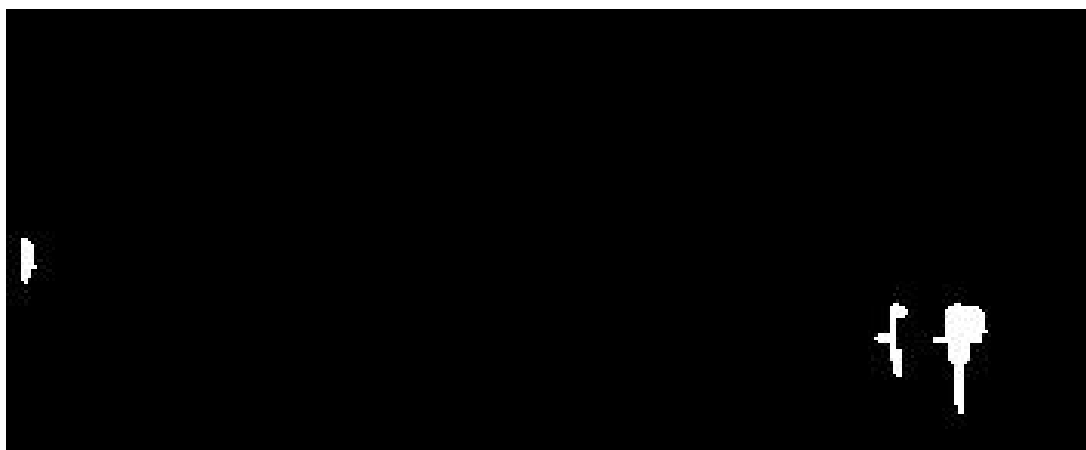


Figure 3.11: Result Image after Seed Initiation

The boundary detection computes the object edge and provides its boundary for the seed growth. The flow chart of boundary detection is shown in Figure 3.12.

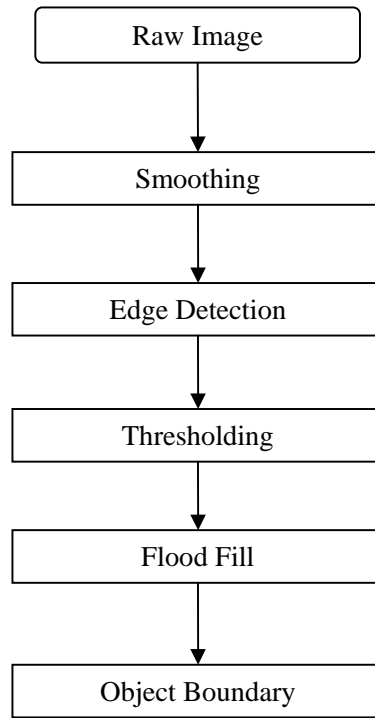


Figure 3.12: Boundary Detection Flow Chart

The boundary detection finds feature boundaries through edge detection using Sobel edge detector as described in Equations 3.10.

$$S(m, n) = \sqrt{S_x^2 + S_y^2}$$

$$\theta = \arctan (S_y/S_x)$$

$$S_x = \begin{bmatrix} -1 & -2 & -1 \\ 0 & 0 & 0 \\ +1 & +2 & +1 \end{bmatrix} * I$$

$$S_y = \begin{bmatrix} -1 & 0 & +1 \\ -2 & 0 & +2 \\ -1 & 0 & +1 \end{bmatrix} * I$$

(3.10)

Where $S(m,n)$ and θ are the amplitude and the angle of the Sobel edge at location (m,n) .

The result image after Sobel edge detection is shown in Figure 3.13.

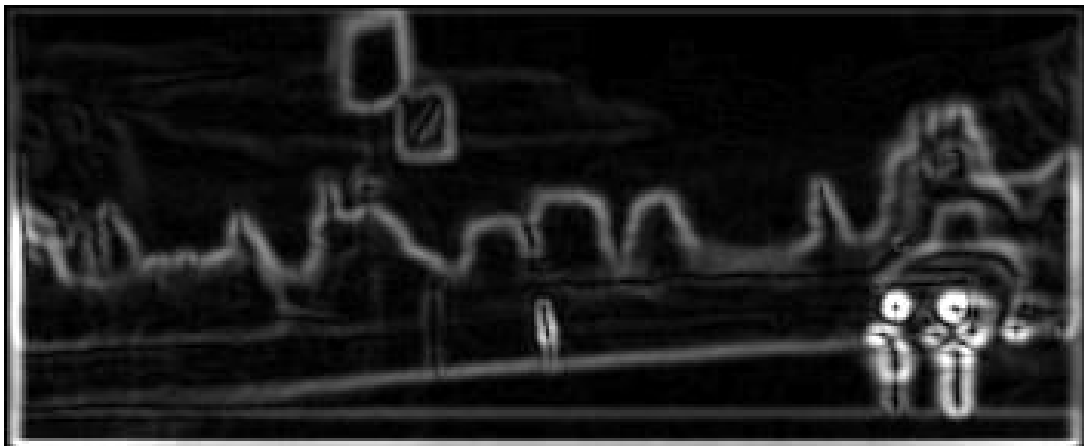


Figure 3.13: Result Image after Sobel Edge Detection

Furthermore, another thresholding is applied on Figure 3.13 to outline the edges of the objects as shown in Figure 3.14.

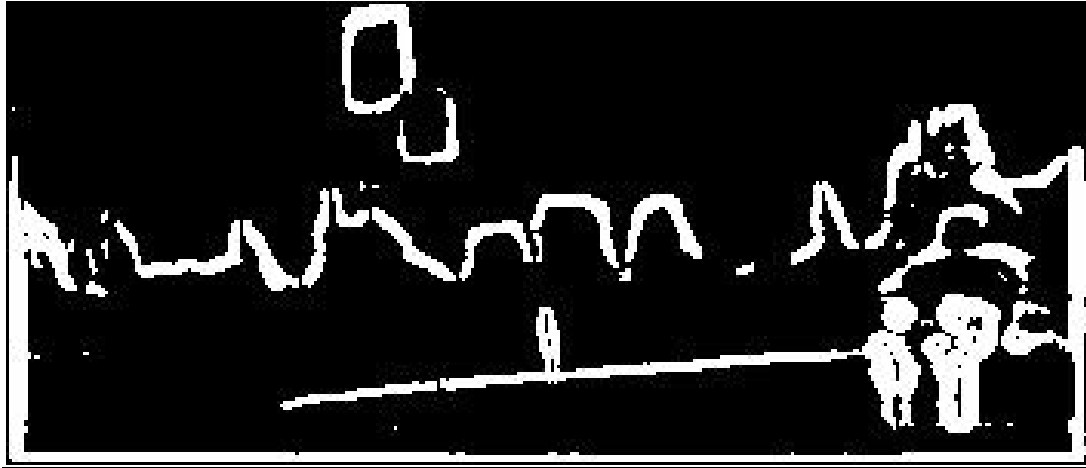


Figure 3.14: Result Image of Sobel Edge after Thresholding

Then a flood fill is utilized to fill the holes and remove small discontinuities in the object boundaries as shown in Figure 3.15. It displays connected boundaries and is used to control the growth of the seeds.

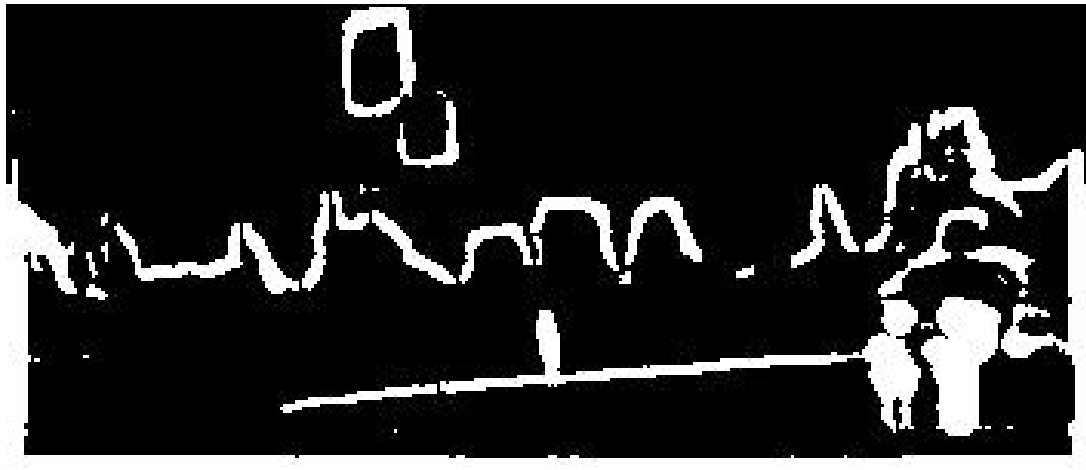


Figure 3.15: Result Image with Object Boundaries

The established object boundaries are now utilized to guide seed growth. The seed growth procedure is described in Figure 3.16.

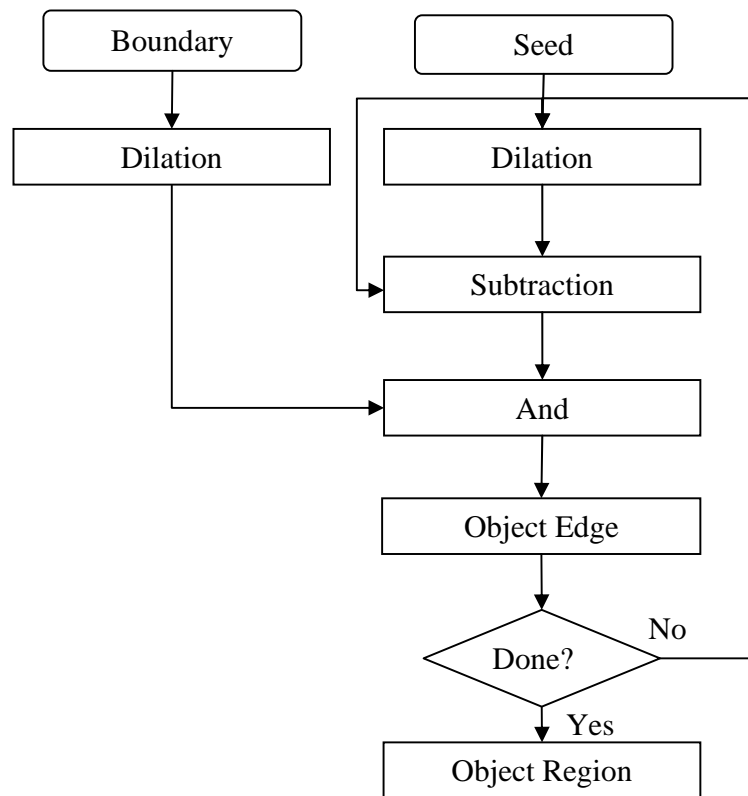


Figure 3.16: Flow Chart of Seed Growth

A series of morphological operations are applied using erosion and dilation to grow the seeds toward their boundaries and find the feature regions. The seed is first dilated by one pixel and then subtracted by the original seed before dilation to get its dilated edges. Next, the dilated edges are masked onto the boundary image in Figure 3.15 to get its actual edges in its boundaries. Repeat the growing process until converge when

the length of the actual edge stops increasing. Finally the seed after the growing process becomes the detected object.

The moment and centroid of the detected objects are calculated using Equation 3.11 and the lengths of the major and minor axes are calculated using Equations 3.12.

$$m_{pq} = \sum_x \sum_y x^p y^q I(x, y)$$

$$X_c = \frac{m_{10}}{m_{00}}, Y_c = \frac{m_{01}}{m_{00}}$$
(3.11)

Where $I(x, y)$ is the pixel intensity at location (x, y) ; m_{00} is the summation of the intensity of all pixels; m_{10} is the summation of the x moment of all pixels; m_{01} is the summation of the y moment of all pixels; (X_c, Y_c) is the centroid location.

$$a = \frac{\text{trace}_C + \sqrt{\text{trace}_C^2 - 4\text{det}_C}}{2}$$

$$b = \frac{\text{trace}_C - \sqrt{\text{trace}_C^2 - 4\text{det}_C}}{2}$$

$$\text{trace}_C = \text{cov}(x, x) + \text{cov}(y, y)$$

$$\text{det}_C = \text{cov}(x, x)\text{cov}(y, y) - \text{cov}(x, y)\text{cov}(y, x)$$

$$\text{cov}(x, y) = \frac{\sum_{i=1}^{i=n} (x_i - \bar{x})(y_i - \bar{y})}{n - 1}$$
(3.12)

Where a is the length of the major axis; b is the length of the minor axis.

The direction of the detected object is calculated as the angle between the major axis and the minor axis described in Equation 3.13.

$$\theta = \frac{1}{2} \arctan \frac{2cov(x,y)}{cov(x,x) - cov(y,y)} \quad (3.13)$$

Finally, the major and minor axes are used to draw a rectangle overlay showing the object with tracking information in the result image as shown in Figure 3.17.



Figure 3.17: Result Image with Tracking Information

3.3.2 Feature Level Image Fusion

The feature level image fusion routine is shown in Figure 3.18 [51]. First, the preprocessing is utilized on both thermal and visible images and prepares them for feature extraction. Next, feature extraction is applied separately to extract relevant

information from two images. After that, the feature level fusion criterion is applied abased on the logic relationships between those extracted features. Finally, the result image is constructed for further processing.

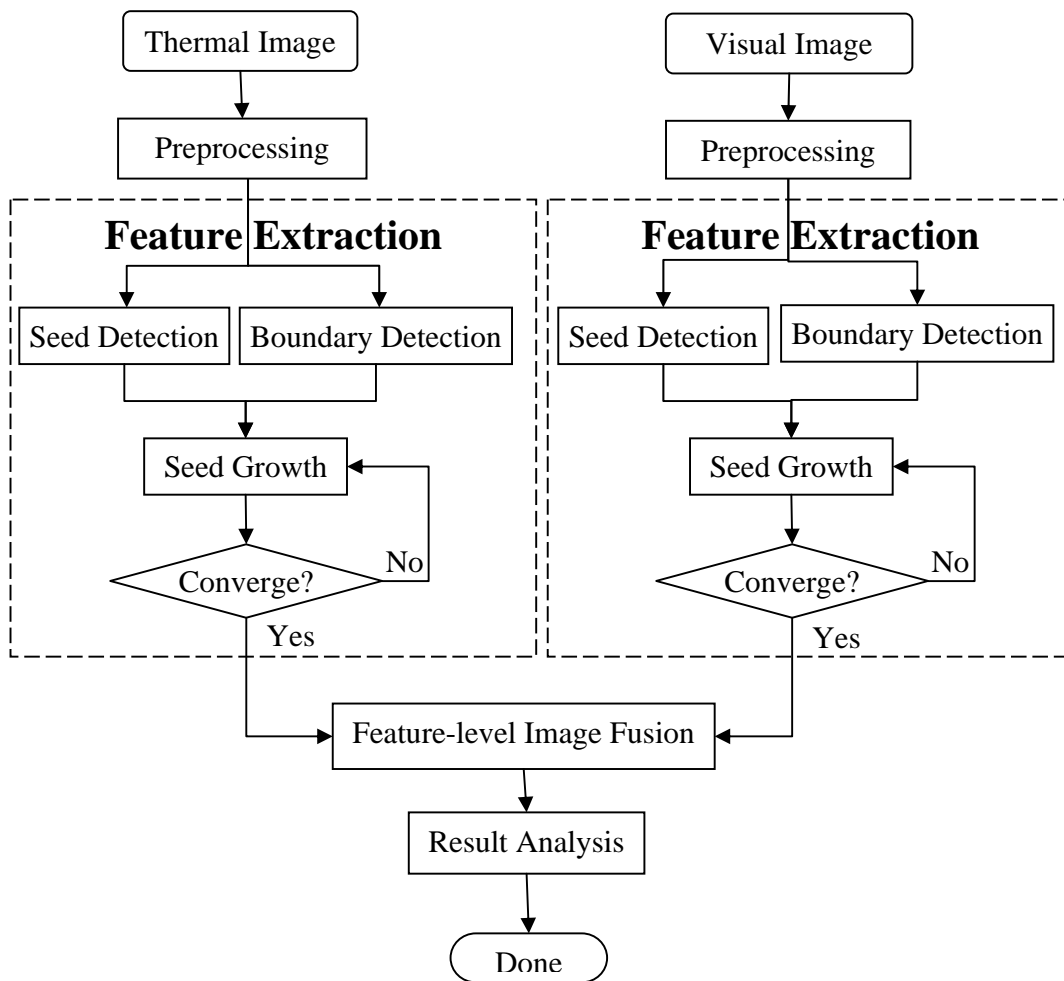


Figure 3.18: Flow Chart of Feature Level Image Fusion Routine

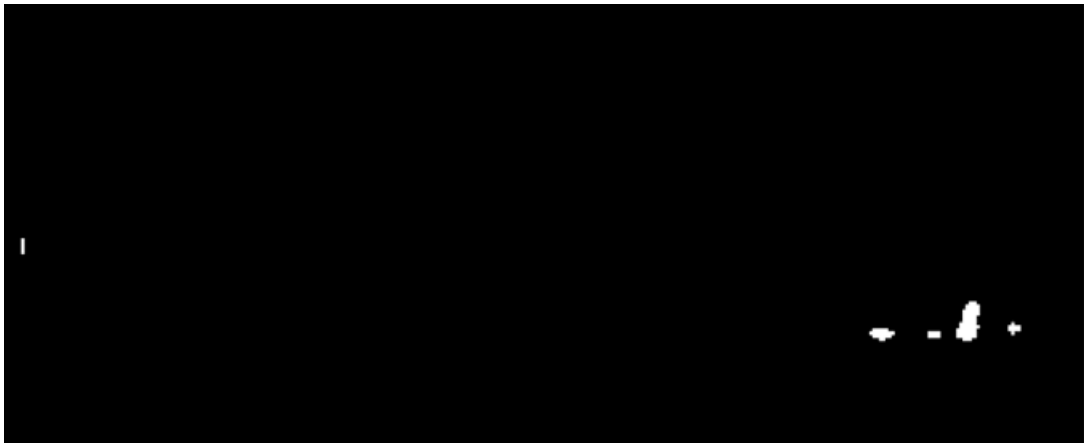
Preprocessing

The preprocessing is also applied on both the thermal and visible images to normalize their intensity to the range of 0 to 255 using Equation 3.7 and smooth both images using Gaussian kernel as described in Equation 3.8.

Feature Extraction

The feature extraction is also based on the seed initiation and growth algorithm described in tracking algorithm section in pixel level image fusion. It consists of three primary steps: seed initiation, boundary detection, and seed growth to find the object.

The seed initiation is accomplished through a double weighted thresholding based on the histogram of the thermal or visible image in Figure 3.6. The resulted images after double thresholding are displayed in Figure 3.19.



(a)



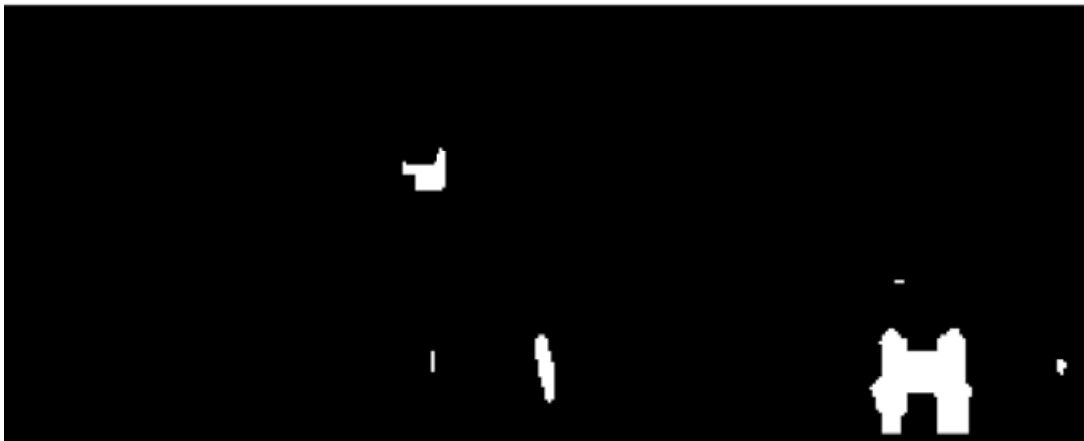
(b)

Figure 3.19: Seed Initiation Results: (a) Thermal Image; (b) Visible Image

The boundary detection is then implemented by using a Sobel edge detector coupled with a flood fill algorithm. Figure 3.20 shows the results after applying the boundary detection on Figure 3.6. In thermal result image, Figure 3.20(a), the detected objects are the vehicles tires and body due to the frictional heat generated. And in visible result image, Figure 3.20(b), the detected objects are the vehicle head lamps and the traffic signs. Thus, the feature extraction can detect relevant information from both channels that can be combined in the fusion step.



(a)

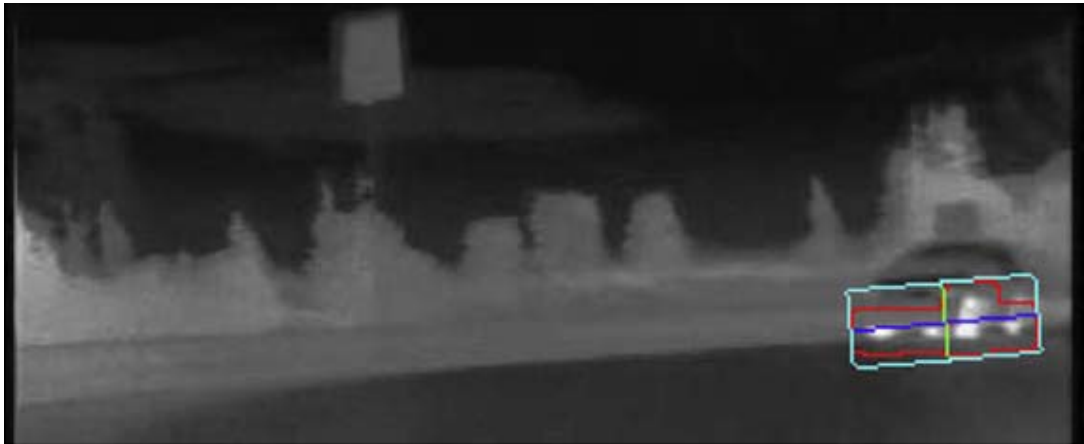


(b)

Figure 3.20: Boundary Detection Results: (a) Thermal Image; (b) Visible Image

Once the seed and boundary are obtained, a seed growth process is performed by using erosion and dilation to grow the seeds until convergence. Then a feature extraction process is utilized on both thermal and visible images to extract the object features or such as location, size, aspect ratio, and direction.

Finally, the detected objects are displayed by using a rectangle overlay on both of the raw images as displayed in Figure 3.21.



(a)



(b)

Figure 3.21: Feature Extraction Results: (a) Thermal Image; (b) Visible Image

Feature Level Fusion Algorithm

The feature level fusion algorithm operates on the features based on their relationships shown graphically in Figure 3.22, in which circle T represents thermal feature and rectangle V represents visible feature.

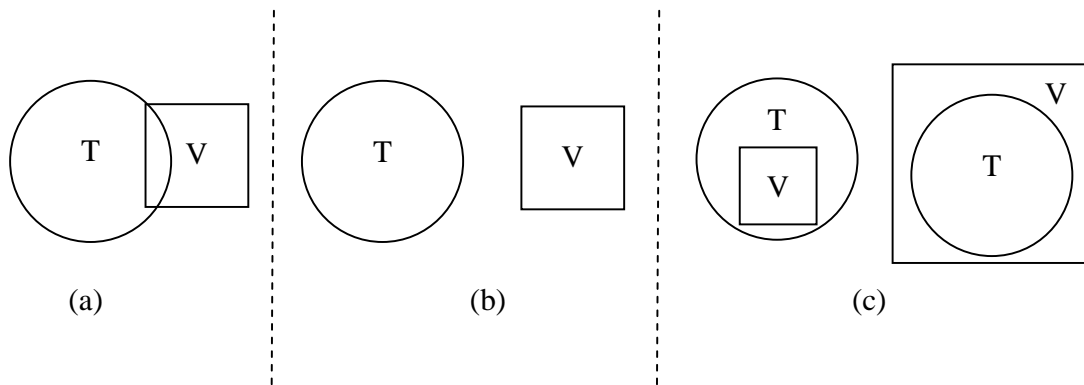


Figure 3.22: Feature Relationships: (a) Intersection; (b) Disjoint; (c) Inclusion

The feature level image fusion algorithm is shown in Equation 3.14 based on the feature relationships in Figure 3.22.

$$\begin{cases} F = T \cup V & \text{Intersection} \\ F = T \cup V & \text{Disjoint} \\ F = T \cap V & \text{Inclusion} \end{cases}$$

(3.14)

In Intersection condition, both detected features contain incomplete information of the same object. Thus, an OR operation is applied to keep complementary information

and remove redundant information. In Disjoint condition, each detected feature contains the information for different object. Thus, an OR operation is applied to keep both of them. In Inclusion condition, both detected features also contain the information of the same object. However, one feature includes the other one. Thus, an AND operation is applied to obtain more concise information of the object.

Because the wavelength of LWIR is from 7.5 to 13.5 μm and that of the visible light is from 0.38 to 0.78 μm , the detected features from thermal and visible images are inherently complementary.

The image fusion result of the passing vehicle scenario in Figure 3.6 is shown in Figure 3.23. Both the emitting objects such as the vehicle tires and body from the thermal image and the reflective objects such as the vehicle head lamps and the road sign from visible image are fused in the final result image.

For the approaching vehicle scenario with glare in Figure 3.7, the fused image is shown in Figure 3.24. The thermal image carries more emitting components like the vehicle but misses the reflective components from the ambient environment, mainly road signs and markings. While the visible image carries more reflective components about the road sign and lane markings but is saturated by the bright glare that hinders the detection of the object shape or orientation. The feature level fusion result retains emitting and reflective objects from both the thermal and visible channels and also attenuates the glare to show the vehicle in more details.

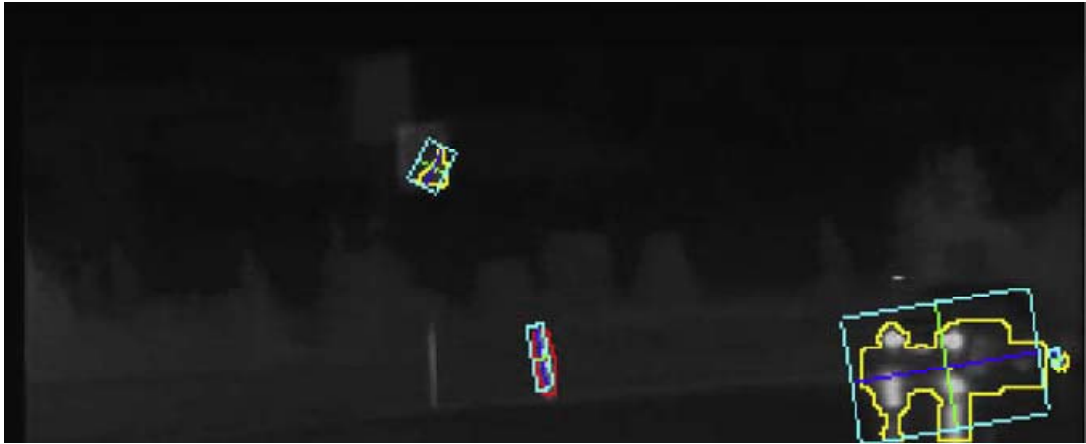


Figure 3.23: Feature Level Fusion Result of Passing Vehicle Scenario



Figure 3.24: Feature Level Fusion Result of Approaching Vehicle Scenario

3.3.3 Pixel Level Image Fusion vs. Feature Level Image Fusion

Pixel level fusion is considered to be lower level and of lower complexity than the feature level fusion, because it fuses raw images directly pixel by pixel to enhance the features. It shows good shape retrieval for vehicles and enables the detection of cold objects, such as traffic lights, lane, and road markers. However, it disregards the internal interconnection of related objects. For example, the tire extracted from the thermal channel and the head light extracted from the visible channel are treated as two separate objects, but they both are relative parts of the vehicle.

On the other hand, the feature level fusion is considered advantageous because it considers the internal interconnection of different objects and provides more comprehensive information of the object. It also requires a subroutine to distinguish the relationship between the features from different channels and perform according fusion operation. However, the feature level fusion requires complex intelligent algorithm and also extensive processing time.

The comparisons of pixel level and feature level image fusion results are shown in Figure 3.25 and Figure 3.26.



(a)



(b)

Figure 3.25: Image Fusion Results of Passing Vehicle Scenario: (a) Pixel Level; (b) Feature Level



(a)



(b)

Figure 3.26: Image Fusion Results of Approaching Vehicle Scenario: (a) Pixel Level; (b)
Feature Level

Both pixel level and feature level image fusion algorithms are successful in fusing relative information from thermal and visible channels for the final result image. However, for the passing vehicle scenario, feature level fusion result in Figure 3.25(b) describes more accurate shape of the vehicle and more ambient objects than pixel level fusion result in Figure 3.25(a). For the approaching vehicle scenario, the feature level fusion result in Figure 3.26(b) also beats the pixel level fusion result in Figure 3.26(a) by better vehicle shape retrieval and more road sign detection.

The comparison indicates that the feature level fusion produces result images with more relative features and more accurate detection. The pixel level fusion is more sensitive to the intensity scales of features from different channels, while the feature level fusion focuses more on their logic relationships regardless their pixel level intensity unbalance. That is why the feature level fusion can detect the accurate shape of the vehicle in the approaching vehicle scenario in Figure 3.26(b), but the pixel level fusion suffers from the bright glare and retrieves inaccurate shape of the vehicle in Figure 3.26(a). However, the feature level fusion performs feature extraction on both of the thermal and visible images and hence requires more processing time and resources, which makes it not competitive in time critical applications.

3.4 Summary

This chapter first introduces image fusion in three levels: pixel level, feature level and decision level. Then it focused on pixel level image fusion and related literature review is presented including weighted average, comparison, and MSD. After that, an image fusion application in night vision is demonstrated with technical details. Both pixel level image fusion and feature level image fusion are developed to enhance the original thermal image and visible images. Comparison between pixel level image fusion and feature level image fusion is made to show the advantages and disadvantages on both sides.

CHAPTER FOUR

PRINCIPAL COMPONENT ANALYSIS

4.1 PCA Introduction

Principal component analysis is a statistical analysis for dimension reduction. It basically projects data from its original space to its eigenspace to increase the variance and reduce the covariance by retaining the components corresponding to the largest eigenvalues and discarding other components. PCA helps to reduce redundant information and highlight the components with biggest influence so as to increase the signal-to-noise ratio.

PCA is also a linear transformation that is easy to be implemented for applications in which huge amount of data is to be analyzed. PCA is widely used in data compression and pattern matching by expressing the data in a way to highlight the similarities and differences without much loss of information.

4.2 Literature Review of PCA

4.2.1 PCA in Thermography

Rajic [52] proposed a Principal Component Thermography (PCT) technique to process the thermal image sequences acquired from composite structures testing and to enhance the contrast of the image sequences. The proposed technique is applied on flash thermographic inspection data of the composite structures. A set of orthogonal statistical modes are used to enhance the contrast of the captured thermal images. In PCT, the thermal image sequences are first normalized to reduce the effects caused by reflection

and disturbances from surroundings. After that, the PCT is applied on the image sequences and the first empirical orthogonal function is retained to obtain the enhanced image. Typically, the first two or three empirical orthogonal functions contain nearly 90 percent of the variability of the image data and the remaining variability is present in the rest functions that can be neglected. This method has produced higher contrast in result images compared to other available processing methods such as Pulse Phase Thermography (PPT) and image averaging.

Marinetti [53] presented a statistical analysis of thermographic sequences using PCT based on thermal contrast evaluation and the second order statistics. Since the image data captured by the thermal cameras consists of undesirable noises, the PCT first projects original data onto a system of orthogonal components and then eliminates the undesirable noises by discarding less important orthogonal components to enhance the useful thermal information. Singular Value Decomposition (SVD) technique is used in place of original PCT to reduce the amount of computation and increase the computation speed. The processing of the thermal images provides good performance in improving the image contrast for steel plate samples with circular holes and opaque plastic samples with square holes.

4.2.2 PCA in Image Fusion

Zheng and Miao et al [54, 55] proposed an image fusion algorithm using Finite Ridgelet Transform (FRIT) to decompose the raw images to low and high frequency components. The low frequency coefficients are fused by PCA using Equation 4.1.

Suppose $(x, y)^T$ is a vector of the eigenvectors of the image A and B, the weight value of image A and image B are ω_A and ω_B .

$$\omega_A = \frac{x}{x+y}, \omega_B = \frac{y}{x+y} \quad (4.1)$$

Then, the fusion is accomplished using a weighted average as described in Equation 4.2.

$$I_F = \omega_A I_A + \omega_B I_B \quad (4.2)$$

And the high frequency coefficients are fused by selecting maximum-method as described in Equation 4.3.

$$I_F = \max \{abs(I_A), abs(I_B)\} \quad (4.3)$$

Then a region consistency check is followed to finish the fusion process. In the consistency checking, if the center pixel is selected from image A but the neighbors are mostly from image B, the center pixel is to be selected from image B. The experiment results of the FRIT and PCA based algorithm outperform those of the wavelet transform

and the Laplacian pyramid in enhancing the edge and texture information. This fusion algorithm also overcomes the instability and discontinuity problem in multi-scale decomposition based image fusion.

Singha et al [56] developed a PCA based image fusion technique in face recognition using both thermal and visible images. The PCA is applied to linearly project face images in a low-dimensional space, the eigenspace. Then, each face image is represented as low-dimensional feature vector, containing the coefficients of the projection of the image in the eigenspace. Genetic algorithms are employed to calculate the coefficients for both original thermal and visible images for fusion. Then, instead of the original images the eigenfeatures computed from the original images are fused to combine important information from each eigenspace by selecting a subset of eigenfeatures from the eigenspace. Genetic algorithms are used again to decide which eigenfeatures to be select and from which eigenspace. Recognition is then performed by matching the coefficients of an unknown face image to the coefficients of a set of known images.

4.3 PCA Implementation

Three PCA implementation methods are presented in the order of original PCA, SVD based PCA and economical SVD based PCA.

4.3.1 Original PCA

In original PCA, the data is projected from its original space to its eigenspace to increase the variance and reduce the covariance so as to identify patterns in the data. The flow chart of original PCA is shown in Figure 4.1.

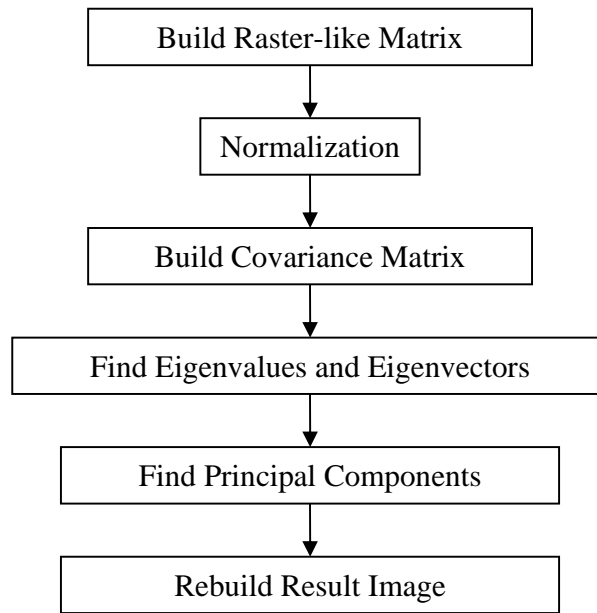


Figure 4.1: Flow Chart of Original PCA

In Thermography application, typically a sequence of thermal images is acquired from thermographic inspection. This thermal image sequence is similar to the image sequence shown in Figure 4.2. However, this thermal image sequence form a 3D matrix with frame number N_t , frame width N_x and frame height N_y in each image.

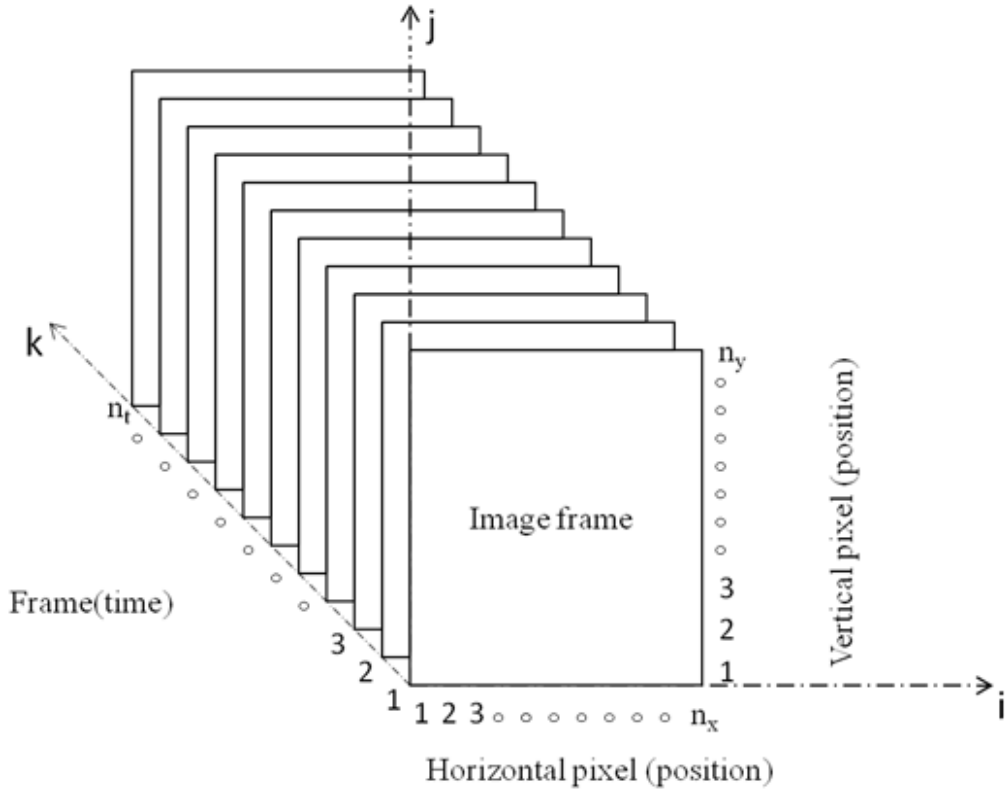


Figure 4.2: Sequence of N_t Image Frames with Width N_x and Height N_y

Before applying PCA, a matrix operation is needed to convert this 3D matrix into a 2D matrix and subtract mean value from each data point to create zero-centered data [52, 53].

Each image frame of width N_x and height N_y can be represented as a vector X with $N_x N_y$ elements as shown in Equation 4.4.

$$X = (x_1, x_2, \dots, x_{N_x N_y}) \tag{4.4}$$

The rows of pixels in an image frame are placed one after another to form the vector X . The first N_x elements in the vector X are pixels in the first row of the image and the next N_x elements are pixels in the second row of the image and so on. Eventually, the last N_x elements in the vector X are pixels in the last row of the image. Similarly, the same operation is performed on all the N_t frames in the captured image sequence. Then, a 2D image sequence matrix is generated by combining the N_t vectors.

There are two choices to create this kind of 2D matrix also known as raster-like matrix.

One is to combine the N_t vector X vertically as shown in Equation 4.5. This 2D matrix takes the image frame number N_t as the row number and the image frame size $N_x N_y$ as the column number. In this case, the data dimension is N_t and the number of case is $N_x N_y$. From physical point of view, each pixel location in an image frame is considered as a test sample and N_t tests are performed for $N_x N_y$ samples. Subtract off mean value of each row which is also the mean image from each element in the row of matrix A . Then the principal axes are $N_x N_y$ pixels in an image frame and the projected data are N_t temporal profiles.

$$A = \begin{bmatrix} X_1 \\ X_2 \\ \vdots \\ X_{N_t} \end{bmatrix} = \begin{bmatrix} x_{11} & \cdots & x_{1N_x N_y} \\ \vdots & \ddots & \vdots \\ x_{N_t 1} & \cdots & x_{N_t N_x N_y} \end{bmatrix}_{N_t \times N_x N_y} \quad (4.5)$$

The other one is on the opposite to combine N_t transposed vector X horizontally as shown in Equation 4.6. This 2D matrix takes the image frame size $N_x N_y$ as the row number and the image frame number N_t as the column number. While in this case, the data dimension is $N_x N_y$ and the number of cases is N_t . From physical point of view, each image frame is considered as a test sample and $N_x N_y$ tests are performed for N_t samples. Also, subtract off mean of each row which is also the mean temporal profile of each pixel from each element in the row of matrix A . Dimensionally speaking, the principal axes are N_t temporal profiles and the projected data are $N_x N_y$ pixels to form an image frame.

$$A = [X_1^T \quad X_2^T \quad \dots \quad X_{N_t}^T] = \begin{bmatrix} x_{11} & \dots & x_{1N_t} \\ \vdots & \ddots & \vdots \\ x_{N_x N_y 1} & \dots & x_{N_x N_y N_t} \end{bmatrix}_{N_x N_y \times N_t} \quad (4.6)$$

Physically, these two 2D matrices in Equation 4.5 and Equation 4.6 have different meanings. One uses the mean image to remove spatial constant and the other one uses the mean temporal profile to remove temporal constant. However, mathematically, these two 2D matrices are interchangeable through a matrix transpose operation and subtraction off the mean value of each row or the mean value of each column.

A normalization operation is applied to reduce the side effects caused by uneven heating and noises and create a zero centered data in each dimension as described in Equation 4.7.

$$\hat{A}(m, n) = \frac{A(m, n) - \mu_n}{\sigma_n}$$

$$\mu_n = \frac{1}{M} \sum_{m=1}^M A(m, n)$$

$$\sigma_n = \sqrt{\frac{1}{M-1} \sum_{m=1}^M (A(m, n) - \mu_n)^2}$$
(4.7)

Then the covariance matrix of the normalized raster-like matrix is calculated using Equation 4.8.

$$C = \frac{1}{N} \hat{A} \hat{A}^T$$
(4.8)

Where \hat{A} is the normalized raster-like matrix; C is the covariance matrix.

The eigenvalues and eigenvectors can be found using matrix diagonalization described in Equation 4.9.

$$C_D = P^{-1} C P$$
(4.9)

Where C is the covariance matrix; C_D is the diagonalized covariance matrix with eigenvalues on the diagonal; P is the matrix with eigenvectors as its columns.

Then sort the diagonalized covariance matrix C_D to make the eigenvalues in a descending order and also sort the matrix P in the same order. To reduce the dimension of the original matrix, retain the first K columns in matrix P to form matrix P_K . And then convert the original matrix to the new basis using Equation 4.10.

$$C_P = P_K^T C \quad (4.10)$$

Finally, reconstruct the result image using the dimension reduced raster-like matrix C_P . The choice of K is based on the amount of the variance proportion desired to be retained in the first K eigenvalues described in Equation 4.11. In many cases more than 95% of variance is contained in the first three to five components.

$$r = \frac{\sum_{i=1}^K e_i}{\sum_{i=1}^M e_i} \quad (4.11)$$

Where e_i is the i th eigenvalue of the diagonal matrix C_D .

However, since a covariance matrix of dimension $D \times D$ is built in PCA, it can only be used when the size of the raster-like matrix D is small. When D becomes large, PCA becomes very slow. To solve this problem, SVD based PCA is developed to reduce the amount of computation and save processing time.

4.3.2 SVD based PCA

The SVD based PCA uses SVD transformation to find the eigenvalues and eigenvectors. Generally, a matrix with dimension $M \times N$ can be decomposed to three smaller matrices using Equation 4.12.

$$A = U\Sigma V^T \tag{4.12}$$

Where if $M \geq N$, U is an $M \times M$ matrix; Σ is an $M \times N$ diagonal matrix with non-negative elements representing the singular values of matrix A ; V is an $N \times N$ matrix.

And each column of U gives coordinates of matrix A in the space of principal component. By retaining the first few columns of matrix U and reconstructing the result image, it's convenient to reduce redundant data in the original image sequence.

Similarly, once the raster-like matrix A is built and normalized, the SVD transformation is applied to find the eigenvalues and eigenvectors using Equation 4.12. The flow chart of SVD based PCA is shown in Figure 4.3.

Once the three matrices U , S and V^T are obtained, the first few columns of matrix U which are the empirical orthogonal functions give the coordinates of matrix A in the space of principal component. The result image reconstructed using the empirical orthogonal functions from matrix U shows enhanced contrast between the target object

and background as well as the redundant data reduction from the original image sequence.

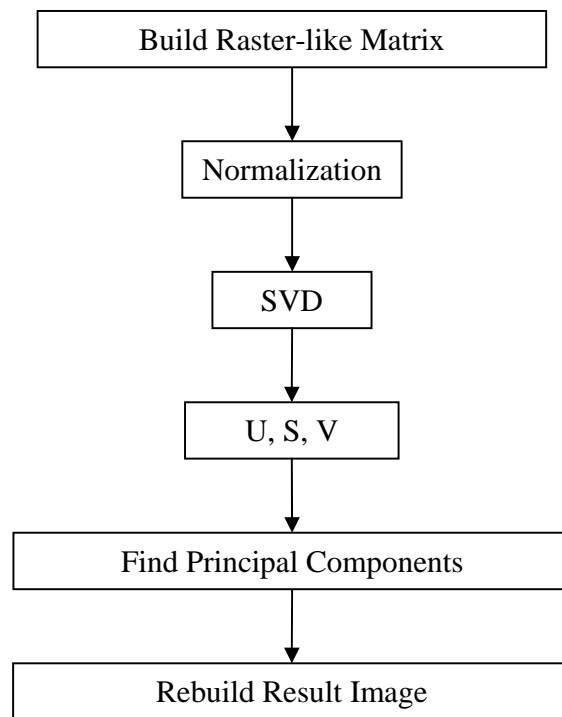


Figure 4.3: Flow Chart of SVD Based PCA

4.3.3 Economical SVD based PCA

Since only the first few columns of matrix U are retained for reconstructing the result image, an economical SVD based PCA is developed to increase efficiency and save time.

To use the economical SVD based PCA, the second case to build the raster-like matrix is selected using Equation 4.6. The same normalization operation is applied to create a zero centered data in each dimension using Equation 4.7.

Next, the economical SVD is applied on the normalized matrix \hat{A} using Equation 4.12. When the size of normalized matrix \hat{A} is $M \times N$, where $M = N_x \times N_y$, $N = N_t$, $M \gg N$, the economical SVD computes only the first N columns of matrix U and the size of matrix Σ is $N \times N$ instead of $M \times M$. Finally, the result spatial image is rebuilt by using the first few empirical orthogonal functions from the matrix U representing nearly 80 to 90 percent of the variation of the original image sequence.

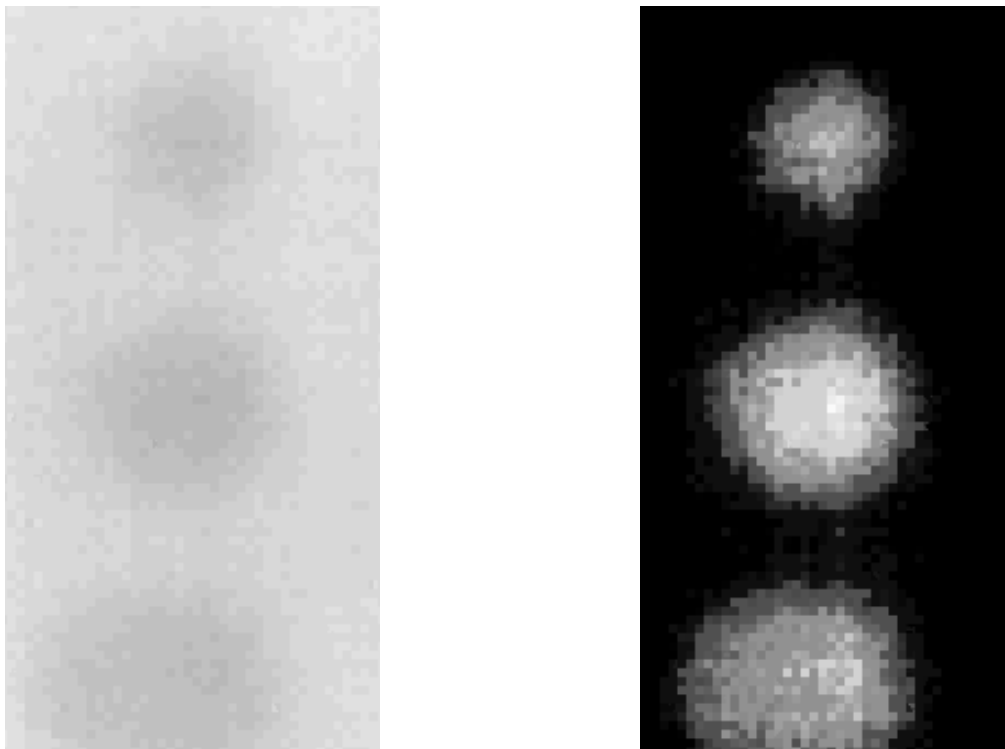
4.4 PCA Application in Thermography

To show the versatility of PCA based image processing method, thermographic experiments conducted using different energy excitations are investigated. And the results obtained by applying the economical SVD based PCA algorithm are presented and discussed as follows.

Test samples are thermal image sequences containing three circular adhesive spots of different dimensions between two thin galvanized steel panels. These test samples are similar to the hemming joints used in automotive industry. Two thermal cameras tested are FLIR ThermoVision A40M uncooled thermal camera and FLIR Phoenix DTS cooled thermal camera. Three heat sources tested are 3000 watts flash ring, 1000 watts induction heater and 4000 watts halogen lamp. Once the samples are heat

excited their responses are captured using thermal cameras and the thermal image sequences are processed by using the economical SVD based PCA.

In flash ring case, the test sample is thermally excited using flash ring lamps and the thermal image sequence is captured by using the FLIR Phoenix DTS cooled thermal camera due to the fast frame rate needed. The raw thermal image in Figure 4.4 (a) is then processed by using the economical SVD based PCA to get the result image in Figure 4.4 (b).The result image effectively highlights three separate spots against the background between the galvanized panels and also has better edge visibility than the original one. The intensity variation observed in the result image is also much higher than that of the original image.



(a)

(b)

Figure 4.4: Result of Flash Ring Sample: (a) Raw Image; (b) Result Image

In induction heater case, the test sample is thermally excited using the induction coil. The thermal image sequence of the test sample is captured by using the FLIR ThermoVision A40M uncooled thermal camera due to the slow frame rate. The captured raw image is shown in Figure 4.5 (a). The result image of economical SVD based PCA is shown in Figure 4.5 (b). The economical SVD based PCA also enhances the contrast between the adhesive spots and steel background in this sample. However, due to the slow speed of the induction heating, heat transfer effect starts in the relatively long heating process causing the upper two bigger spots connecting to the edge of the sample. This problem can be solved by using faster heating source such as halogen lamp discussed next.

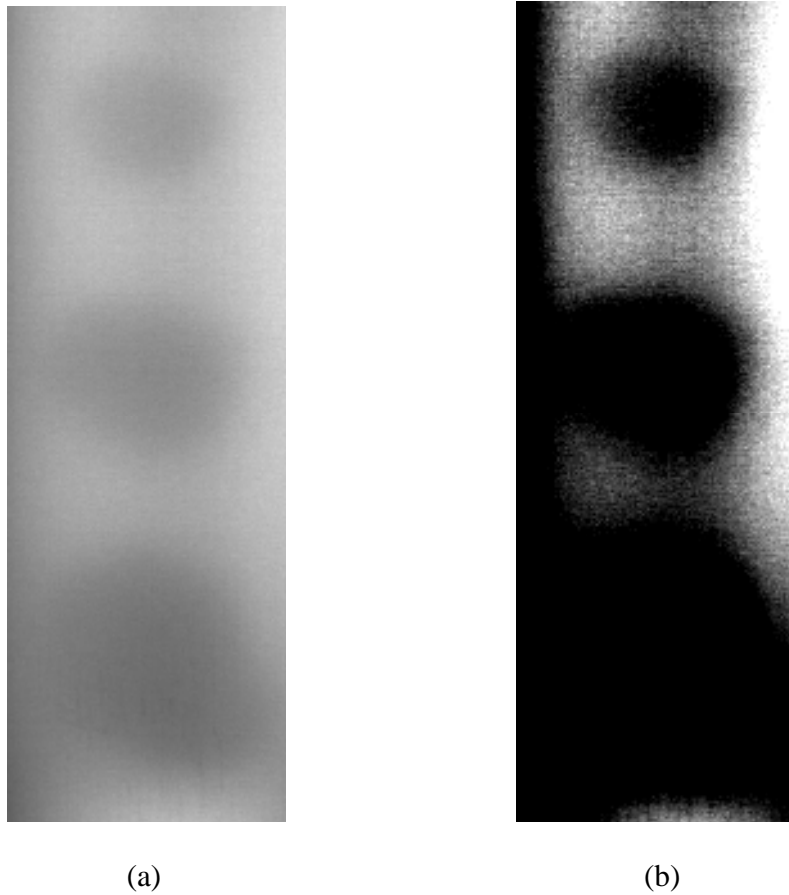


Figure 4.5: Result of Induction Heater Sample: (a) Raw Image; (b) Result Image

In halogen lamp case, the test sample is thermally excited using halogen lamps. The thermal image sequence of the test sample is also captured using ThermoVision A40M uncooled thermal camera. The captured raw image is shown in Figure 4.6 (a). The result image of economical SVD based PCA is shown in Figure 4.6 (b). The result image effectively increases the contrast between the three adhesive spots and the steel background. And the edges of the spots are also enhanced and sharpen for inspection.

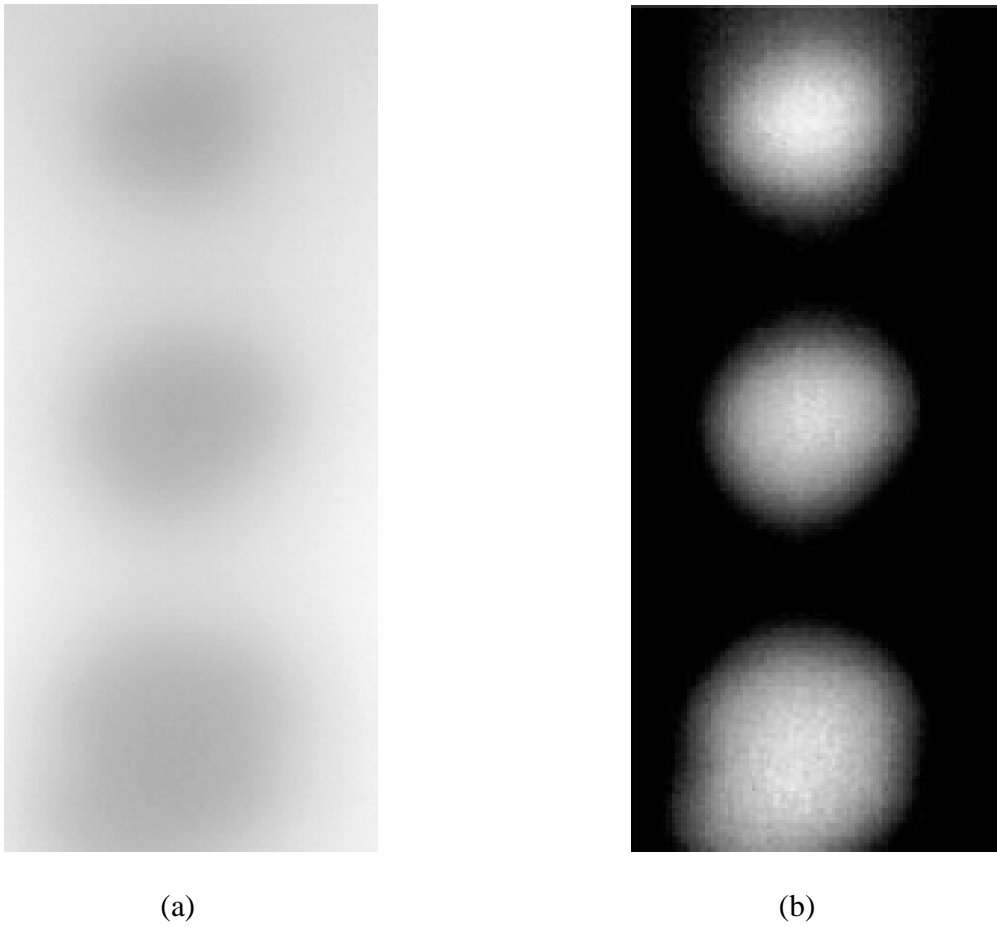


Figure 4.6: Result of Halogen Lamp Sample: (a) Raw Image; (b) Result Image

From Figure 4.4 to Figure 4.6, the raw images and result images are presented for various heating sources: flash ring, induction heater and halogen lamp, respectively. From the spatial images shown above, the economical SVD based PCA method is proved to be an efficient method for SNR increase, contrast improvement and edge enhancement. Additionally, the processing time needed is reduced to seconds depending on the size of the thermal image sequences, which enables its potential for online inspection

application. For the three heating cases, sequences containing 10 frames are tested and processing time is less than 5 seconds.

4.5 PCA Application in Image Fusion

The economical SVD based PCA is also utilized in image fusion application to reduce the complexity of the raw image, decrease noises and highlight key features. The flow chart of PCA based image fusion is shown in Figure 4.7. The economical SVD based PCA is applied on both thermal and visible images separately to highlight the features and reduce noises. And then, a pixel level image fusion is applied to obtain the PCA based fusion results. The image fusion rules can be comparison, fixed average or adaptive average.

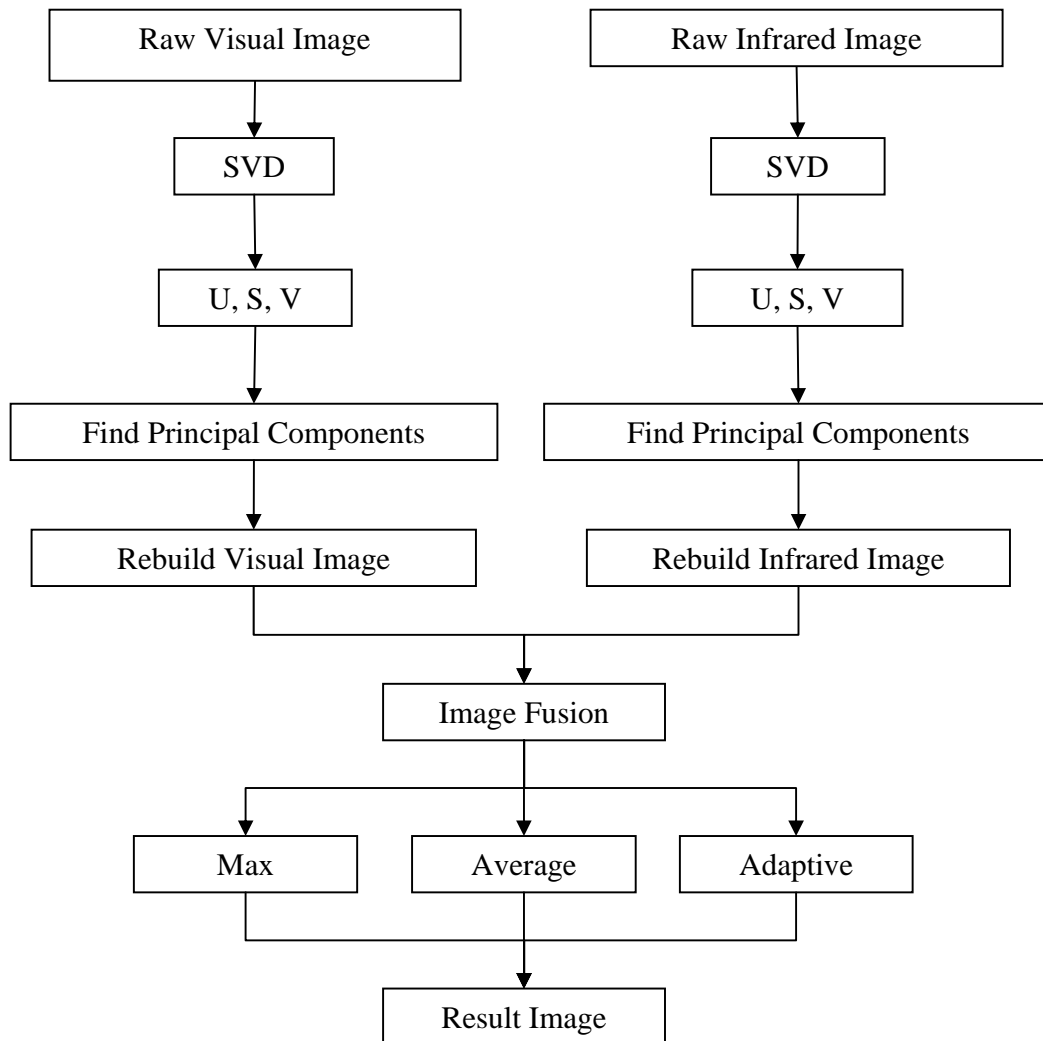
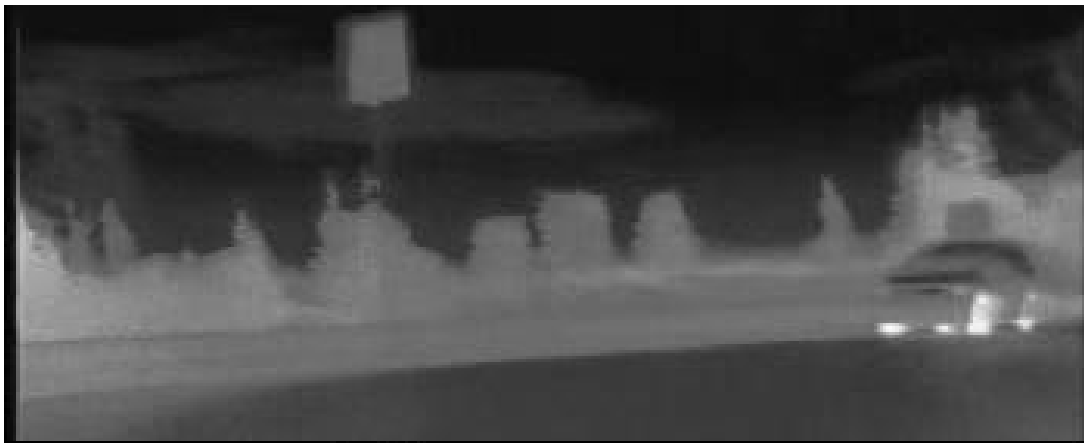


Figure 4.7: Flow Chart of PCA based Image Fusion

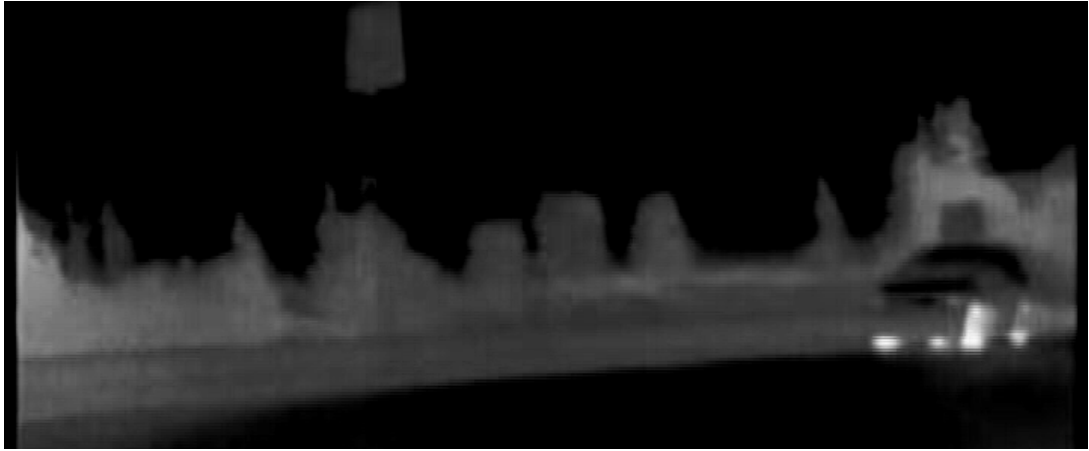
To show the effect of PCA based image fusion, the same night vision experimental samples are utilized which are passing vehicle scenario and approaching vehicle scenario.

For the passing vehicle scenario shown in Figure 4.8 and Figure 4.9, the PCA eliminates the undesired background objects such as the cloud and the far forest and

retains the key features such as the vehicle, the road sign and near forest in the thermal images as shown in Figure 4.8 (b) and Figure 4.9 (b). At the mean time, the contrasts between the key features and the background are increased. The edges of the key features are also enhanced to facilitate later fusion and tracking processing. In the visible result images shown in Figure 4.8 (d) and Figure 4.9 (d), the white noises introduced by the visible cameras are greatly decreased. And the key features and their edges are also enhanced. The pixel level image fusion is accomplished by using a simple 50% and 50% fixed weighted average to make comparison between image fusion result without PCA and that with PCA as shown in Figure 4.8 (e)(f) and Figure 4.9 (e)(f). Through comparison, the PCA based image fusion successfully retains all key features as well as increases the SNR and enhances the edges and contours of the key features.



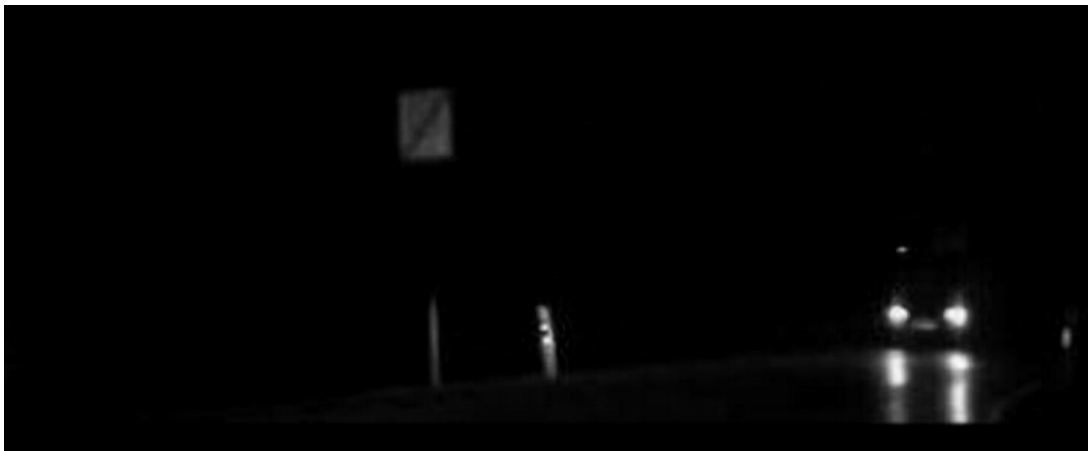
(a)



(b)



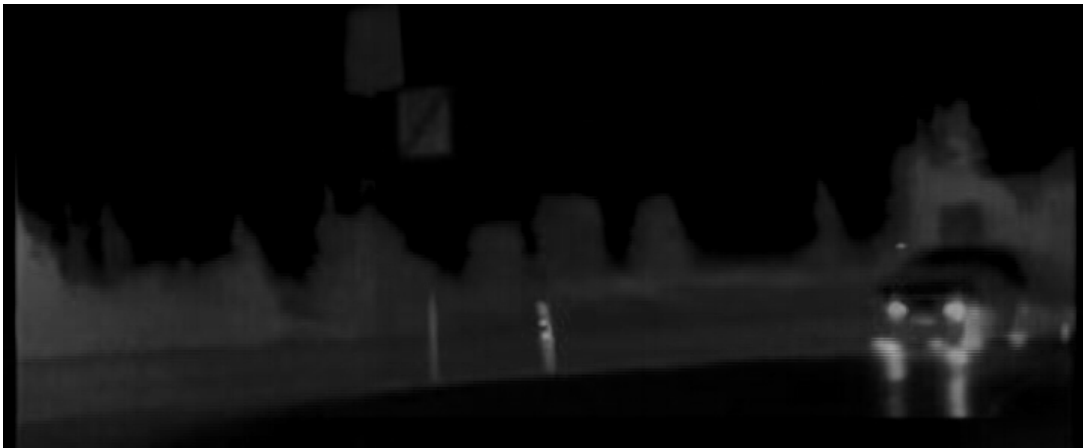
(c)



(d)



(e)



(f)

Figure 4.8: Passing Vehicle Scenario 1: (a) Raw Thermal Image; (b) Thermal Image after PCA; (c) Raw Visible Image; (d) Visible Image after PCA; (e) Fused Image without PCA; (f) Fused Image with PCA



(a)



(b)



(c)



(d)



(e)



(f)

Figure 4.9: Passing Vehicle Scenario 2: (a) Raw Thermal Image; (b) Thermal Image after PCA; (c) Raw Visible Image; (d) Visible Image after PCA; (e) Fused Image without PCA; (f) Fused Image with PCA

For the approaching vehicle scenario case, the PCA based image fusion also fulfills the task to outline key features, selectively remove undesired information and reduce noises. In PCA processed thermal image shown in Figure 4.10 (b), the PCA cleans the background by darken the sky and road as well as brighten the vehicle and near forests. In PCA processed visible image shown in Figure 4.10 (d), the edge of the glare is sharpened and white noises introduced by the visible camera are also reduced. Finally in the PCA processed fused image shown in Figure 4.10 (f), the entire image is smoother and the background and the vehicle details are clearer than the raw fused image shown in Figure 4.10 (e).



(a)



(b)



(c)



(d)



(e)



(f)

Figure 4.10: Approaching Vehicle Scenario: (a) Raw Thermal Image; (b) Thermal Image after PCA; (c) Raw Visible Image; (d) Visible Image after PCA; (e) Fused Image without PCA; (f) Fused Image with PCA

4.6 Summary

This chapter first presents the literature review of PCA in Thermography and image fusion. Then it focuses on the implementation of PCA from mathematical angle. Three kind of implementation methods are introduced in sequence, original PCA, SVD based PCA and economical SVD based PCA. After that, PCA application in Thermography is demonstrated to show the image enhancement for product inspection. Also PCA application in image fusion in night vision is demonstrated to show the improvement in noise reduction and the SNR increase.

CHAPTER FIVE

PCA BASED FUSION IN STAMPING SPLIT DETECTION

In order to fulfill the goal of this dissertation to develop a non-contact, non-intrusive online inspection system to evaluate automotive stampings and improve stamping process control, a system integration of Thermography, image fusion and PCA is designed and developed to provide online objective stamping split detection.

5.1 System Overview

The PCA based image fusion system for stamping split detection is built on a Dell Latitude E6500 laptop equipped with Intel Mobile Core 2 Duo P8400 CPU at 2.26GHz, 4GB DDR2-800 SDRAM, NVIDIA Quadro NVS 160M Video Card with 512 MB RAM, Seagate Momentus 250 GB HDD at 7200RPM, Ricoh IEEE1394 Controller and StarTech CardBus 1394a FireWire Adapter Card.

The operating system is Microsoft Windows XP Professional with Service Pack 3. MathWorks MATLAB R2009a is utilized to as the integrated development environment to communicate with both thermal and visible cameras, initiate image acquisition, analyze acquired image data, display and save analysis results, and provide Graphical User Interface (GUI). The FLIR ThermoVison SDK 2.6 is utilized to control the thermal camera and the MATLAB embedded Image Acquisition Toolbox is utilized to control the visible camera. The PCA and image processing algorithms are developed by using MATLAB Signal Processing Toolbox and Image Processing Toolbox. The image fusion algorithm is developed by using MATLAB scripts and functions in M-files Editor. The

GUI interface is created in MATLAB Graphical User Interface Development Environment (GUIDE). The system configuration is shown in Figure 5.1.

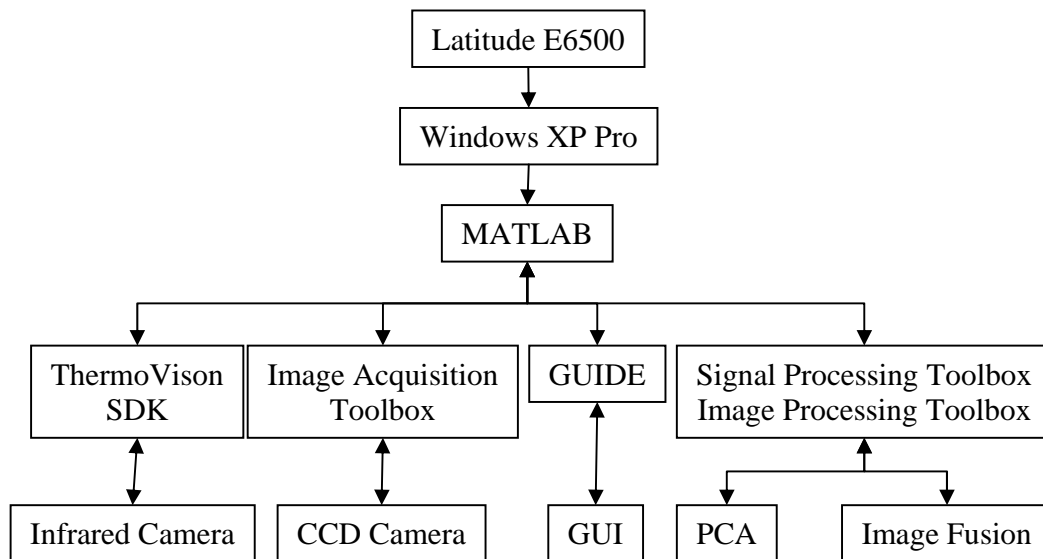


Figure 5.1: Configuration of PCA based Fusion System for Stamping Split Detection

The system setup is shown in Figure 5.2. The PCA based image fusion system utilizes a thermal acquisition head based on Long-wave Infrared (LWIR) micro-bolometric infrared staring array and a visible acquisition head based on Charged Coupled Device (CCD). The registration of the two detectors is implemented from hardware level through proper selection of lenses and setup orientation. Both cameras are connected to a Windows XP based laptop through high speed FireWire connection. And MATLAB based software program utilizes FLIR ThermoVison SDK and MATLAB Image Acquisition Tool Box to manage the thermal and visible image acquisitions as well as the PCA based image fusion algorithm.



Figure 5.2: Experimental Setup of PCA based Image Fusion System

Figure 5.3 shows stamping split sample of vehicle wheelhouse part. The stamping material is draw quality steel. The dimension of the split is about 40×10 mm at the corner of the part. The task of this stamping split detection system is to detect the split and find its location in an online application.


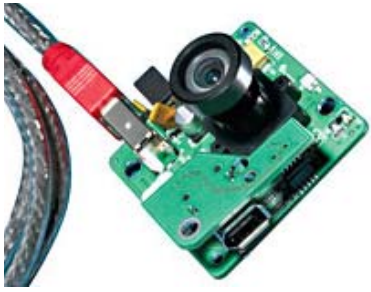


Figure 5.3: Stamping Split Sample of Vehicle Wheelhouse Part

5.2 Camera System

The specifications of the thermal and visible cameras are shown in Table 5.1.

Table 5.1: Specifications of Thermal and Visible Cameras

Description	Thermal Camera	Visible Camera
Camera Type	Focal Plane Array (FPA) uncooled microbolometer	Charge Coupled Device (CCD)
Model Name	FLIR ThermoVison A40M	Unibrain FireWire VGA Board Level Camera
Camera Image		
Resolution	320 × 240	640 × 480
Field of View	24° × 18°	25° × 25°
Thermal Sensitivity	0.08°C at 30°C	N/A
Spectral Sensitivity	7.5-13.5 μm (LWIR)	0.38-0.78 μm (Visible)
Frame Rate	30 Hz	30 Hz
Image Output	8-bit monochrome digital image	8-bit monochrome digital image
Interface	FireWire (IEEE-1394)	FireWire (IEEE-1394)
Transfer Speed	400Mbps	400Mbps

The ThermoVision A40M [57] uncooled thermal camera provides precise non-contact temperature measurement with high image quality. It is able to distinguish temperature difference down to 0.08°C in a range from -40°C to +500°C. It produces digital images with 320×240 resolution at frame rate of 30Hz. And real-time imaging and fast data transfer of fully radiometric 8-bit images can be achieved through IEEE-1394 FireWire digital output. The ThermoVision A40M calibrated measurement output can be easily acquired by using ActiveX based ThermoVision SDK.

The Unibrain [58] FireWire VGA Board Level CCD Camera has full frame electronic shutter, standard M12×0.5 lens mount, uncompressed VGA frame 640 × 480 up to 30Hz and DCAM compliant. It utilizes FireWire technology to provide VGA resolution at low cost. It is also designed to integrate micro video lenses complies with IIDC DCAM 1.04 specifications for industrial uncompressed VGA image acquisition.

5.3 Image Acquisition

A MATLAB based software program is developed to manage image acquisition of thermal and visible cameras. The FLIR ThermoVision SDK is used to control the FLIR ThermoVision A40M thermal camera and the integrated MATLAB Image Acquisition Tool Box is used to control the Unibrain FireWire VGA Board Level CCD Camera.

5.3.1 FLIR ThermoVision SDK

ThermoVision SDK [59, 60] is a System Developers Kit based on ActiveX technology that enables access control and image data manipulation from FLIR thermal

cameras. The SDK accelerates application programming with FLIR thermal camera for end user or system integrator who needs to build customized system utilizing thermal cameras.

The description of each API in ThermoVision SDK is shown in Table 5.2.

Table 5.2: ThermoVision SDK Summary of API

Method	Description
AboutBox Method	You can use the AboutBox method to bring up the About box of the camera Control
Connect Method	Connect with the camera using the specified device, communication interface and port.
Disconnect Method	Disconnect the camera and exit the digital transfer mode.
DoCameraAction Method	Perform a specific camera action as listed below.
EmissCalc Method	Calculates a new emissivity factor for a specified pixel.
GetAbsLUT Method	Obsolete.
GetObjLUT Method	Get a pixel translation table. The table translates absolute image pixels to object pixels.
GetCameraProperty Method	Get specific camera property.
GetError Method	Converts a status code or error code to a formatted error string.
GetImage Method	Get a row-oriented image from the camera.
GetImages Method	Get a sequence of images from the camera.
GetLUT Method	Get a temperature translation table. The table translates absolute image pixels to temperature.
MLGetImages	Get a sequence of images. Used by MatLab.
SetCameraProperty Method	Set specific camera property.
SetDistanceMap Method	Set a distance correction map.
SetEmissMap Method	Set an image emissivity correction map.
SetImage Method	Set an image with absolute image pixel data. The image should be row-oriented.
SubmitCamCommand Method	Submits a user command to the camera.
ToTemperature Method	Converts a given absolute pixel value to temperature in Kelvin.

The ActiveX control module contains one interface named FLIR SDK Camera Control. The control object name exposed to applications is “CAMCTRL.LVCamCtrl.3”. To connect the thermal camera, the ActiveX Control Module is invoked using instructions shown in Figure 5.4.

```

% Open a figure for the Active-X Control
cc_fig = figure('Position',[0,0,188,252],'MenuBar','none',...
               'name','Active-X Camera Control','tag',...
               'CamCtrl_ActiveX','CloseRequestFcn',...
               'camctrl(''exit_camctrl_Callback'','gcbo,[],guidata(gcbo))')

% Set the property of the figure
set(cc_fig,'Color',get(0,'defaultUicontrolBackgroundColor'));

% Display the figure
figure(cc_fig);

% Launch the Active-X control!
CamCtrl = actxcontrol('CAMCTRL.LVCamCtrl.3', [0 0 186 252],...
                    cc_fig,{'CameraEvent' 'CamCtrl_CameraEvent';...
                             'CamCmdReply' 'CamCtrl_CamCmdReply'});

% Infrared Camera Connection: FLIR ThermoVision A40M
invoke(CamCtrl, 'Connect', 5, 0, 3, 3, 'localhost');

% INFRARED Acquire image
Img = invoke(handles.CamCtrl_activeX_h, 'GetImage', imageType)';

% Disconnect infrared camera
invoke(handles.CamCtrl_activeX_h, 'Disconnect');

```

Figure 5.4: Example Instructions using FLIR SDK Camera ActiveX Control Module

First, a MATLAB “figure” function is invoked to create a figure graphic object named “cc_fig” for the ActiveX Control Module with specific properties, such as “menu bar”, “name”, “tag” and “close request function”. And then, a MATLAB “set” function is

invoked to set the color property of the figure. After that, another MATLAB “figure” function is invoked to make current figure “cc_fig” visible and above all other figures on the screen. Once figure “cc_fig” is created, a MATLAB “actxcontrol” function is invoked to create ActiveX control in figure window using the FLIR SDK Camera ActiveX Control Module named “CAMCTRL.LVCamCtrl.3” as shown in Figure 5.5(a). Next, a “Connect” method is invoked to connect to the camera as shown in Figure 5.5(b). Finally, a 'GetImage' method is invoked to acquire an image from the thermal camera. Once the image acquisition is complete, a “Disconnect” method is invoked to close this session and release the thermal camera.



(a)



(b)

Figure 5.5: FLIR SDK Camera ActiveX Control Module: (a) Camera Disconnected; (b)

Camera Connected

5.3.2 MATLAB Image Acquisition Tool Box

The MATLAB Image Acquisition Toolbox [61, 62] is an object-oriented programming library that enables image acquisition directly into MATLAB from PC-compatible imaging hardware. It provides a full solution for image acquisition to detect hardware automatically, configure hardware properties, preview an acquisition, and acquire images. Due to its object-oriented programming features, methods and properties are mainly used to control the camera and acquisition. Specifically, the end user can set up connection between MATLAB and image acquisition devices by using toolbox methods and also control various aspects of the acquisition process by using properties of the object. Once a connection to an imaging device is established, image acquisition is then initiated by a trigger. When the required image frames are acquired, the toolbox first stores them in a memory buffer and then brings them to the workspace for further processing. To enhance image acquisition application, the toolbox also supports event callbacks. By defining certain occurrences as events such as the triggering of an acquisition, it's convenient to build event driven program to execute a particular function by a particular event.

The toolbox uses components called hardware device adaptors to connect to devices through their drivers. The toolbox includes adaptors that support devices produced by different image acquisition equipment vendors. Figure 5.6 shows these components and their relationships.

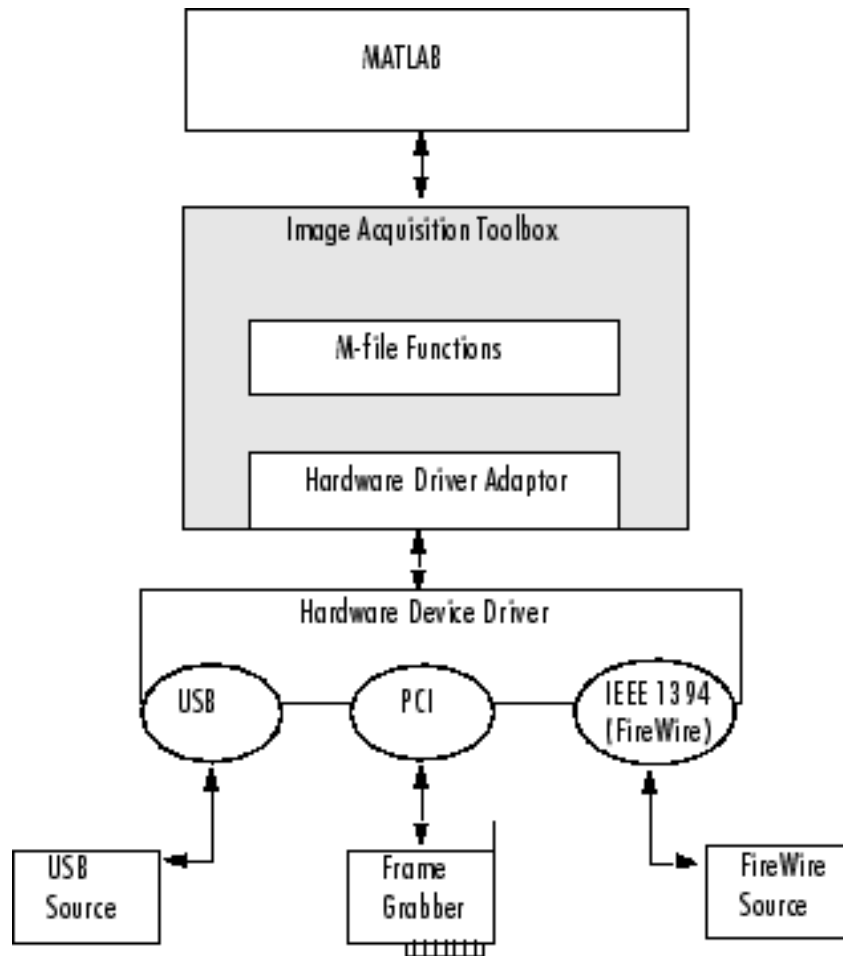


Figure 5.6: Image Acquisition Toolbox Software Components

MATLAB Image Acquisition Toolbox and Image Processing Toolbox provide a complete environment for developing customized image acquisition and image processing applications. The end user can acquire images, visualize data, develop processing algorithms and analysis techniques, create graphical user interfaces, and model real-time embedded imaging systems.

Example instructions using MATLAB Image Acquisition Toolbox is shown in

Figure 5.7. First, a MATLAB “videoinput” function is invoked to create video input object “vid_1”. A video input object represents the connection between MATLAB and a particular image acquisition device. “vid_1” is a text string that specifies the name of the adaptor used to communicate with the device. And then, three MATLAB “set” functions are invoked sequentially to set the property of trigger, frame interval and frame rate, respectively. Finally, a MATLAB “getsnapshot” function is invoked to acquire image from the visible camera. Once the image acquisition is complete, a “delete” function is invoked to close this session and release the visible camera.

```
% Visual Camera Connection: Unibrain Fire-iBoard BW
vid_1 = videoinput('dcam', 1, 'Y8_640x480');

% Set trigger property
set(vid_1, 'TriggerRepeat', Inf);

% Set frame interval property
set(vid_1, 'FrameGrabInterval', 5);

% Set frame frame property
set(vid_1, 'FrameRate', 30);

% VISUAL Aquire image
img_visual = getsnapshot(handles.vid_1);

% Disconnect visual camera
delete(handles.vid_1)
```

Figure 5.7: Example Instructions using MATLAB Image Acquisition Toolbox

5.4 Graphical User Interface

A graphical user interface [63] is a graphical display in one or more windows containing controls and indicators that enable the end user to perform interactive tasks. The user of a GUI doesn't need to understand the technical details of how the tasks are performed or how to create a script or type commands at the command line to accomplish the tasks. GUI components include menus, toolbars, push buttons, radio buttons, list boxes, sliders and so forth. GUIs created using MATLAB can also perform any type of computation, read and write data files, communicate with other GUIs, and display results as tables or as plots.

The GUI based programming is referred to as event-driven programming. In event-driven programming, callback execution is triggered by events external to the software. The GUI waits for the end user to manipulate a control and then responds to each action in turn. Each control of the GUI has one or more user-written routines known as callbacks. The execution of each callback is triggered by a particular user action such as pressing a screen button, clicking a mouse button, selecting a menu item, and so forth. The GUI then responds to these events and executes corresponding callbacks.

The MATLAB Graphical User Interface Development Environment, GUIDE [64], provides a set of tools for creating GUIs.

The GUIDE Layout Editor enables users to populate a GUI by clicking and dragging GUI components into the layout area. Once the GUI layout is finished, GUIDE automatically generates a file of MATLAB code for controlling the way the GUI works. This file contains code to initialize the GUI and organizes the GUI callbacks. Callbacks

are functions that execute in response to user-generated events, such as a mouse click. Using the MATLAB editor, users can add code to the callbacks to perform customized functions.

The GUI of PCA based image fusion system is developed using MATLAB GUIDE, as shown in Figure 5.8.

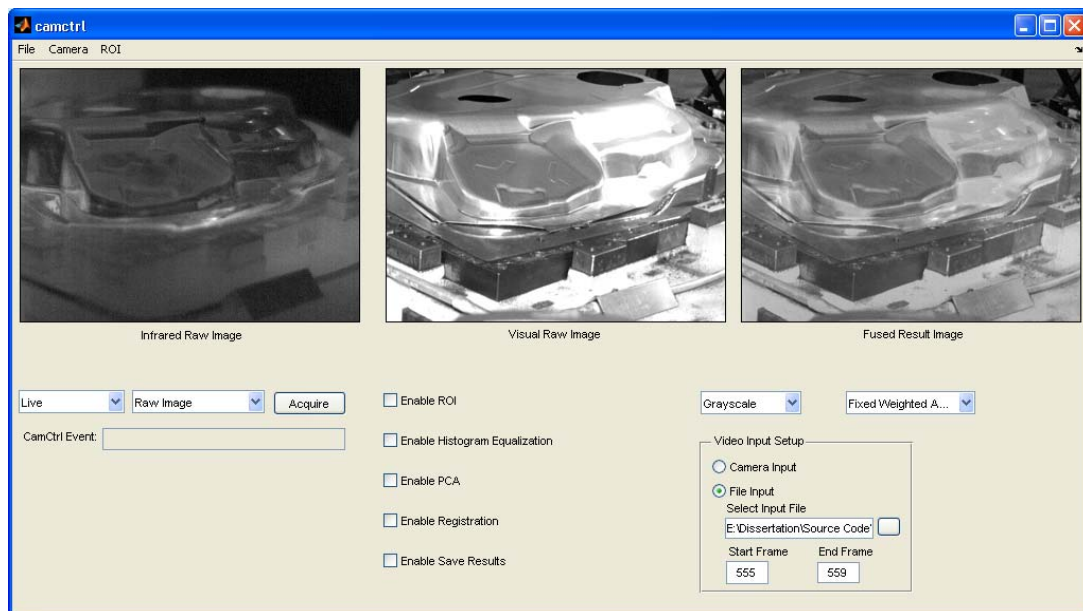


Figure 5.8: GUI of PCA based Image Fusion System

There are three menus, “File”, “File” and “Connect”, at the top left corner of the GUI

In the “File” menu, there is a function named “Exit CamCtrl” to disconnect the cameras and exit the program as shown in Figure 5.9.

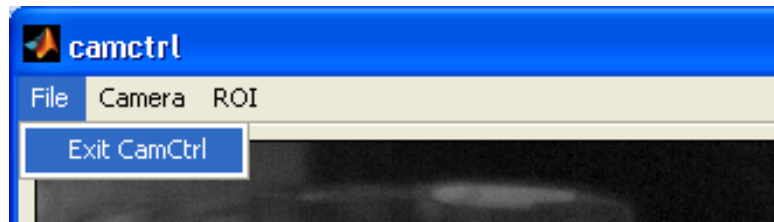


Figure 5.9: File Menu of PCA based Image Fusion System GUI

In the “Camera” menu, there are five functions: “Connect”, “NUC”, “Auto Focus”, “Near Focus” and “Far Focus” as shown in Figure 5.10.

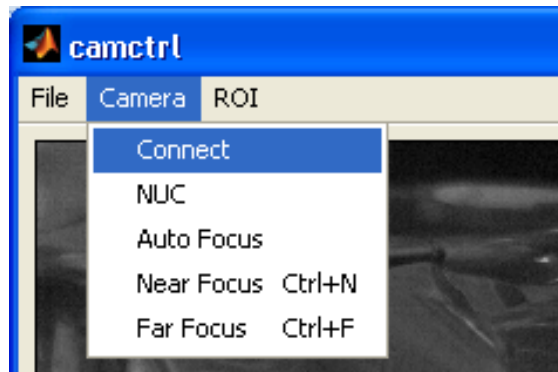


Figure 5.10: Camera Menu of PCA based Image Fusion System GUI

The “Connect” function is used to connect the thermal camera and the visible camera. For the thermal camera, once the “Connect” function is executed, the FLIR SDK Camera ActiveX Control Module shown in Figure 5.5 appears to set up the connection. For the visible camera, functions in the MATLAB Image Acquisition Toolbox are executed to set up the connection.

The “NUC” function which stands for Non Uniformity Correction is used to calibrate the thermal camera and remove bad pixels.

The “Auto Focus” function is used to adjust the focus of the thermal camera automatically. Relatively, the “Near Focus” function and the “Far Function” are used to adjust the focus of the thermal camera closer and farther manually. However, for the visible camera, since the lens is fixed, the focus can only be adjusted by hand.

In the “ROI” menu, there is a function named “Select ROI” as shown in Figure 5.11. Once the “Select ROI” menu item is clicked, a standard dialog box will pop up for retrieving template file. After selecting the template file, a window named “Select ROI” will pop up and the user can select a rectangle ROI on the image by dragging and click mouse as shown in Figure 5.12. Once ROI selection is complete, double click the ROI to exit. Then when the program runs again only image pixels in ROI will be processed.

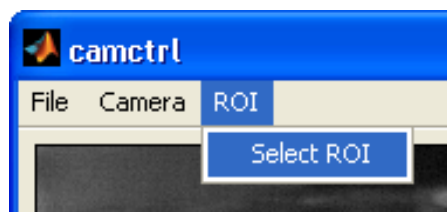


Figure 5.11: ROI Menu of PCA based Image Fusion System GUI

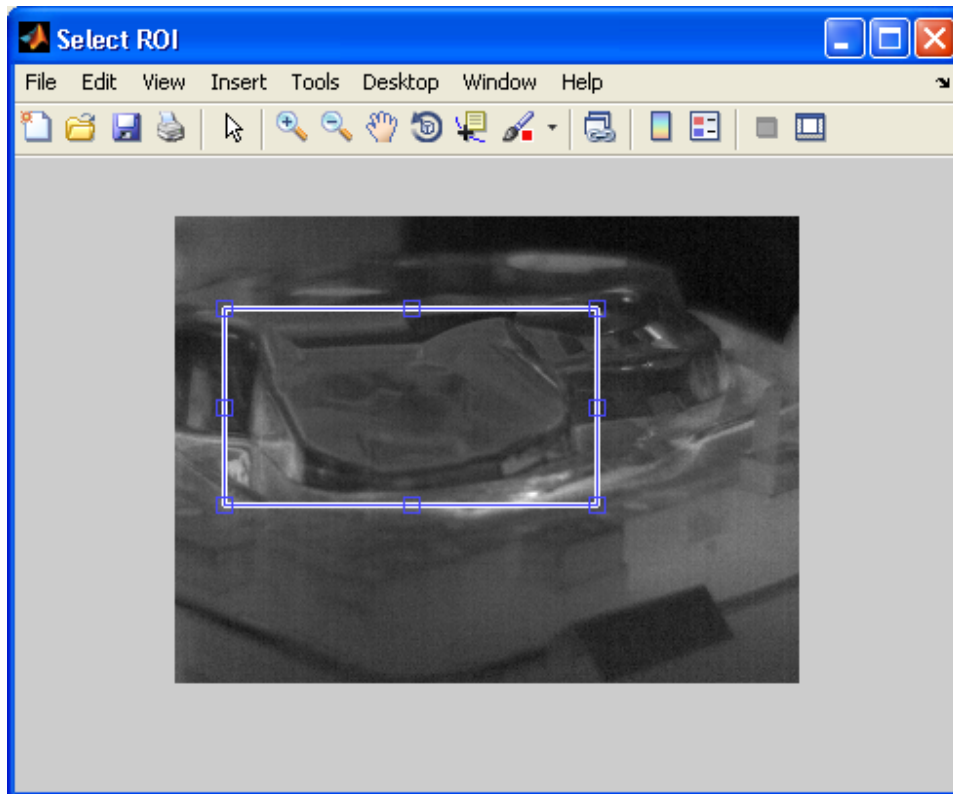


Figure 5.12: ROI Selection of PCA based Image Fusion System GUI

Below the menu, there are three display images, “Thermal Raw Image”, “Visible Raw Image” and “Fused Result Image”, from left to right. They display the original thermal image, original visible image and result fusion image of previous two.

Below image displays, there are three function groups indicated by three red rectangles as shown in Figure 5.13.

The left function group is the “Image Acquisition Control” group. In the “Image Acquisition Control” function group, the left popup menu contains two items, “Single” and “Live”, which are used to acquire one single image frame and continuous live image frames, respectively. In the right popup menu, there are four items, “Raw Image”,

“Absolute Image”, “Object Signal Image” and “Temperature Image”, which are used to control the type of image acquired. The “Raw Image” mode acquires original images from the thermal camera without any conversion. The “Absolute Image” mode acquires image pixels in the format of unsigned integer. The “Object Signal Image” mode acquires image pixels in format of single precision float. The “Temperature Image” mode acquires image pixels in absolute temperature in format of single precision float. The “Acquire” button is used to start the image acquisition and the “CamCtrl Event” textbox is used to display the communication information from the camera.

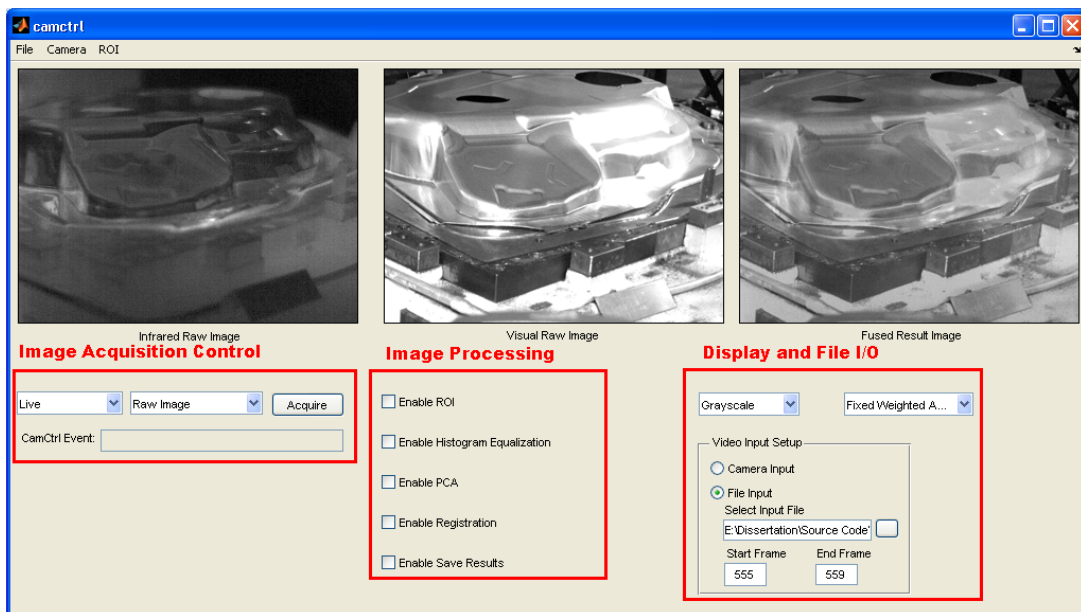


Figure 5.13: Functions of PCA based Image Fusion System GUI

The middle function group is the “Image Processing” group that contains five enable checkboxes to control the image processing as shown in Figure 5.13. The “Enable

ROI” checkbox enables ROI selection and the program only processes the image pixels inside of the ROI. The “Enable Histogram Equalization” checkbox enables image histogram equalization on both thermal and visible raw images to make sure that they are in the same intensity range. The “Enable PCA” checkbox enables PCA analysis on the acquired thermal and visible images. The “Enable Registration” checkbox enables image registration between the thermal image and visible image to remove slight misalignment. And the “Enable Save Results” checkbox enables result saving after processing.

The right function group is the “Display and File I/O” group including “Display Type”, “Image Fusion Method” and “Video Input Setup” as shown in Figure 5.13. The “Display Type” popup menu consists of two items, “Grayscale” and “Pseudocolor”, for image display settings. The “Image Fusion Method” popup menu consists of several image fusion methods, such as “Fixed Weighted Average”, “PCA Weighted Average” and “Max Selection”. The “Video Input Setup” group contains of two video input sources, “Camera Input” and “File Input”. “Camera Input” setting enables image acquisition from the imaging cameras for online applications. “File Input” setting enables image file reading from local storage for off line analysis. The end user may also select image file folder and the start and end frame numbers.

5.5 Principal Component Analysis

The PCA function is implemented using economical SVD as described in chapter 4.3. Since the stamping process is a dynamic process containing fast moving objects, if a few number of image frames are used to build the raster-like matrix and execute the PCA,

the result will show the gradient movement of the object in a blurred image. Therefore, each single image frame is used to build the raster-like matrix for PCA.

The raster-like matrix is built using Equation 4.4 and Equation 4.6. But in this case the number of image frame is one. Therefore, Equation 4.6 can be rewritten as Equation 5.1.

$$A = [X_1^T] = \begin{bmatrix} x_1 \\ \vdots \\ x_{N_x N_y} \end{bmatrix}_{N_x N_y \times 1} \quad (5.1)$$

After that, normalization is applied to reduce the effects caused by reflection and disturbances from surroundings and create a zero centered data in each dimension described in Equation 4.7.

Then, an economical SVD based PCA is applied on the thermal and visible images to enhance features and reduce noises. Figure 5.14 shows the comparison of image results without using PCA and with using PCA. There is a small split at the location marked by a red circle. In the raw thermal image (a), the split area is slightly bright on the dark background but the contrast is poor due to small size. In the raw visible image (b), the split is totally concealed by the bright reflection. The small split in the PCA processed thermal image (c) is sharply enhanced. However other details of the part such as the dents on the top are blurred because the intensity is too close to the

background. While in the PCA processed visible image (d), the split area is also concealed in dark because of the reflection but the dents are displayed in good details.

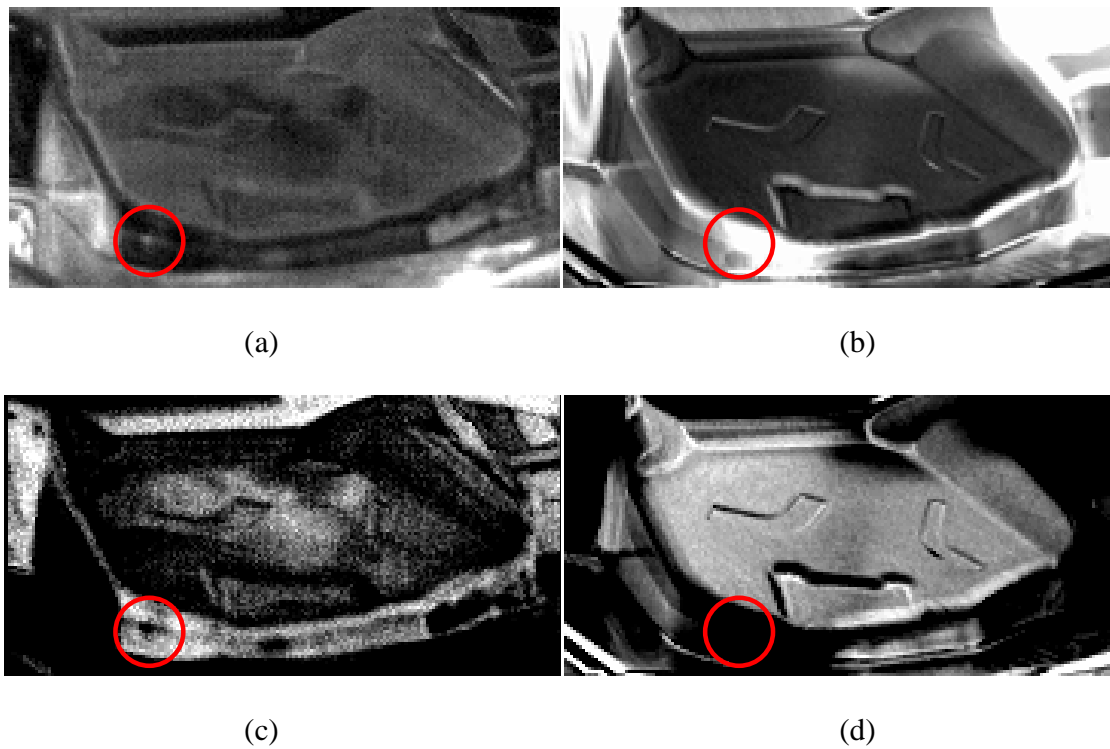


Figure 5.14: Result Images with and without PCA: (a) Raw Thermal Image; (b) Raw Visible Image; (c) Thermal Image after PCA; (d) Visible Image after PCA

5.6 Image Fusion

The image fusion function is used to combine information from both thermal and visible image channels and form a more informative fused image to facilitate split detection. The image fusion methods used in this split detection application are all pixel level based.

There are three pixel level image fusion methods included in this stamping split detection system: Fixed Weighted Average, PCA Weighted Average, and Max Selection.

In the Fixed Weighted Average, the image fusion algorithm utilizes the weight assigned to each image source and adds the weighted raw images together to form the fused image as described in Equation 3.1. The weights for both thermal image and visible image are fixed to 0.5.

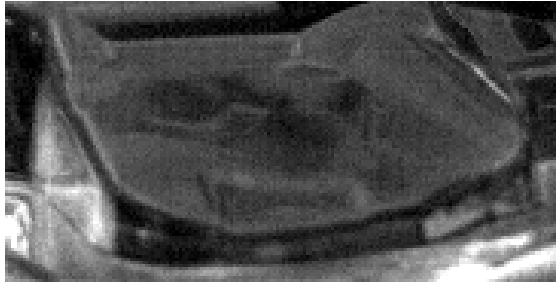
In PCA Weighted Average, Equation 3.1 is also applied. However, the weights for both thermal image and visible image are not fixed. Instead, a practical way to decide the value of ω_T, ω_V is to use the eigenvalues of raster-like matrices of the thermal image and visible image as described in Equation 5.2.

$$\omega_T = \frac{E_T}{E_T + E_V}, \omega_V = \frac{E_V}{E_T + E_V} \quad (5.2)$$

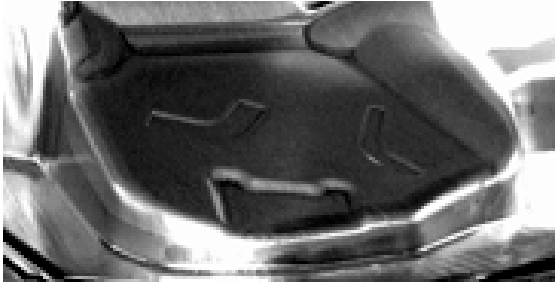
Where E_T is the eigenvalue of thermal image and E_V is the eigenvalue of visible image.

In Max Selection image fusion, the maximum intensity of each pixel location in thermal and visible images is selected as the output as described in Equation 3.2.

The raw thermal image, raw visible image and intermediate result images using different image fusion algorithms and PCA are shown in Figure 5.15.



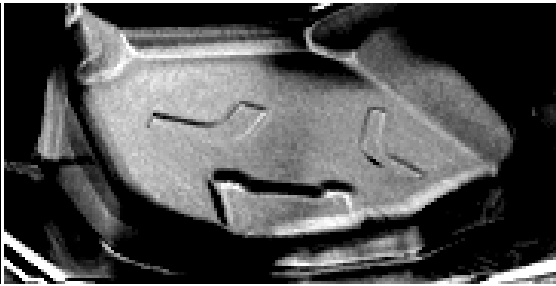
(a)



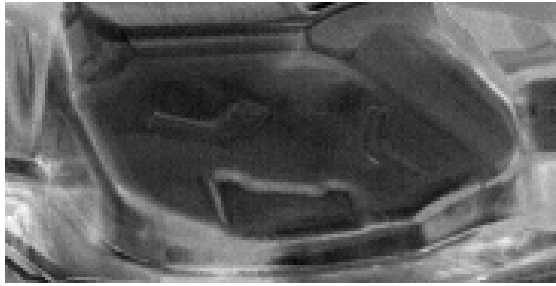
(b)



(c)



(d)



(e)



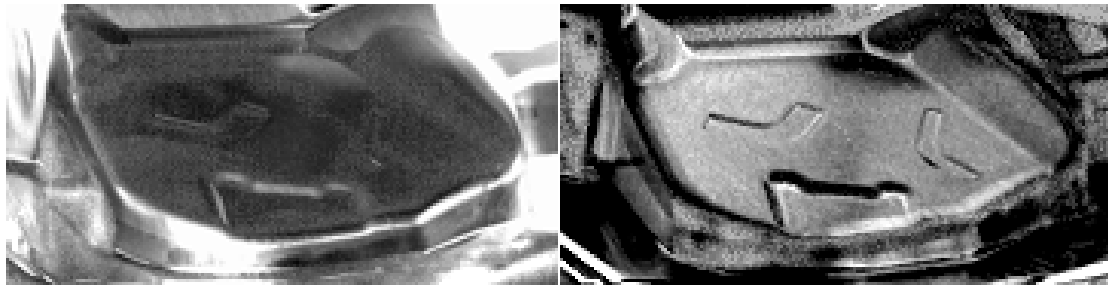
(f)



(g)



(h)



(i)

(j)

Figure 5.15: Image Fusion Results with and without PCA: (a) Raw Thermal Image; (b) Raw Visible Image; (c) Thermal Image after PCA; (d) Visible Image after PCA; (e) Fixed Weighted Average without PCA; (f) Fixed Weighted Average with PCA; (g) PCA Weighted Average without PCA; (h) PCA Weighted Average with PCA; (i) Max Selection without PCA; (j) Max Selection with PCA

5.7 Image Fusion Evaluation

Image fusion evaluation methods can be classified into two types: statistics based method and feature based method [65, 66]. The statistics based method employs standard quality metrics such as standard deviation, SNR and entropy. The feature based method employs image feature quality metrics such as cross entropy and mutual information.

5.7.1 Standard Deviation

Standard deviation is used to evaluate the strength of the signal intensity probability distribution. For a image with size of $M \times N$, the standard deviation is described in Equation 5.3.

$$\sigma_n = \sqrt{\frac{1}{XY} \sum_{x=1}^X \sum_{y=1}^Y (I(x, y) - \mu_n)^2}$$

$$\mu_n = \frac{1}{XY} \sum_{x=1}^X \sum_{y=1}^Y I(x, y)$$
(5.3)

Where σ_n is the standard deviation and μ_n is the mean value of the image.

5.7.2 SNR

SNR is defined as the ratio of the image mean value to its standard deviation described in Equation 5.4. Image with low level of noises tends to have a high SNR.

$$SNR = \frac{\mu_n}{\sigma_n}$$

$$\sigma_n = \sqrt{\frac{1}{XY} \sum_{x=1}^X \sum_{y=1}^Y (I(x, y) - \mu_n)^2}$$

$$\mu_n = \frac{1}{XY} \sum_{x=1}^X \sum_{y=1}^Y I(x, y)$$
(5.4)

5.7.3 Entropy

Image entropy represents the average information content in an image and the complexity of an image. Typically, image with lots of noises has large entropy value. Image entropy is described in Equation 5.5.

$$H_e = - \sum_{i=0}^G P(i) \log_2(P(i))$$
$$r = b - H_e$$
(5.5)

Where G is the number of gray levels; $P(i)$ is the probability of gray level i ; r is the information redundancy; b is the number of bits of the image.

5.7.4 Cross Entropy

The cross entropy of the source images and the fused image is defined in Equation 5.6.

$$CE = \frac{CE(T, F) + CE(V, F)}{2}$$
$$CE(T, F) = \sum_{i=0}^G P_T(i) \log_2\left(\frac{P_T(i)}{P_F(i)}\right)$$
$$CE(V, F) = \sum_{i=0}^G P_V(i) \log_2\left(\frac{P_V(i)}{P_F(i)}\right)$$
(5.6)

Where T, V, F stand for the raw thermal image, raw visible image and fused image, respectively; $CE(T, F)$ is the cross entropy of the raw thermal image and fused image; $CE(V, F)$ is the cross entropy of the raw visible image and fused image.

5.7.5 Mutual Information

Mutual information is defined by using the joint histogram of the source image and the fused image as described in Equation 5.7. Larger mutual information represents better image quality.

$$\begin{aligned}
 MI &= MI_{FT}(f, t) + MI_{FV}(f, v) \\
 MI_{FT}(f, t) &= \sum_{f, t} P_{FT}(f, t) \log_2 \frac{P_{FT}(f, t)}{P_F(f)P_T(t)} \\
 MI_{FV}(f, v) &= \sum_{f, v} P_{FV}(f, v) \log_2 \frac{P_{FV}(f, v)}{P_F(f)P_V(v)}
 \end{aligned}
 \tag{5.7}$$

Where $P_{FT}(f, t)$ is the joint histogram of the raw thermal image T and the fused image F ; $P_{FV}(f, v)$ is the joint histogram of the raw visible image V and the fused image F .

The comparison results of different image fusion methods are shown in Table 5.3.

Table 5.3: Comparison Results of Different Image Fusion Methods

Fusion Method	PCA	STD	SNR	Entropy	Cross Entropy	MI
FWA	Y	51.9485	1.3485	6.2068	1.266	2.1648
PWA	Y	54.8881	1.2992	6.5927	2.0164	2.3609
Max	Y	69.2429	1.4221	5.5991	0.53525	2.3995

Amazingly, the simplest fusion method, “Max Selection”, is the best choice for this application. This is because the PCA analysis transforms the original thermal image and visible image into their principal component spaces, in which the contrast between valuable signals, such as the split and geometrical details, and the background are effectively enlarged and the SNR is also successfully enhanced.

5.8 Split Detection

The split detection routine is similar to the one described in Chapter 2.3 as shown in Figure 5.16.

The fused image is first subtracted by a fused split-free template image. The subtracted image contains potential split contrast information. Then a ROI image is masked onto the subtracted image to highlight the region to be analyzed. After that, a double thresholding algorithm is applied to get the threshold value and to convert the masked image to black and white for split detection. The separate regions are detected one by one for further analysis. Since the detected regions may have holes and small disconnections, a close operation is utilized to remove them. Based on the size of splits, a size thresholding value is selected to determine whether a region is a split or just noise. The size thresholding value is found to be 15 to 20 in this application. Finally, regions

larger than the size thresholding value are treated as splits and their size and location information is calculated. Finally, red rectangular overlays are applied onto the original image to show the detection of the split.

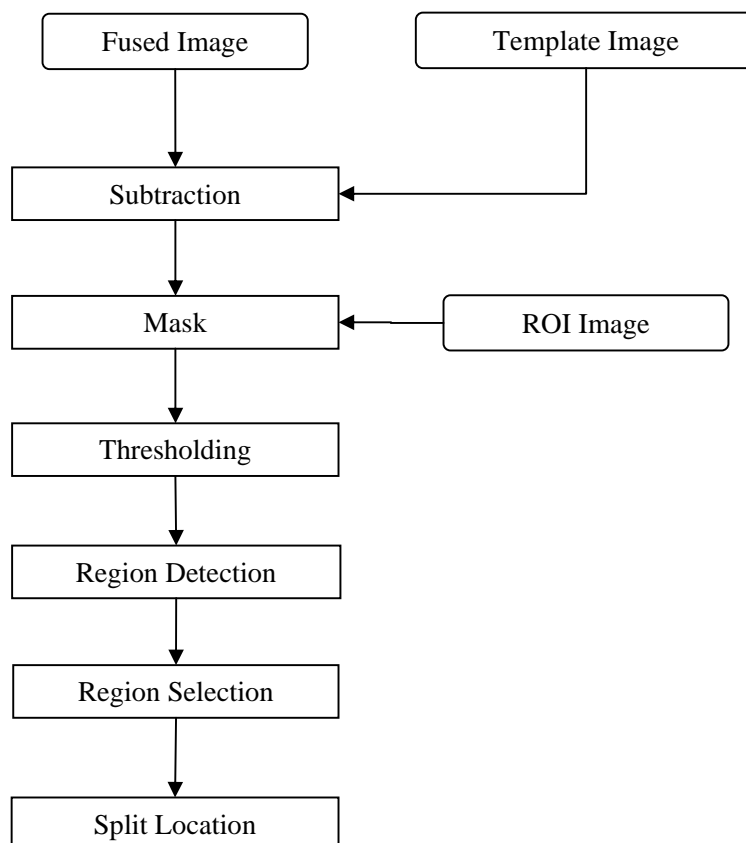
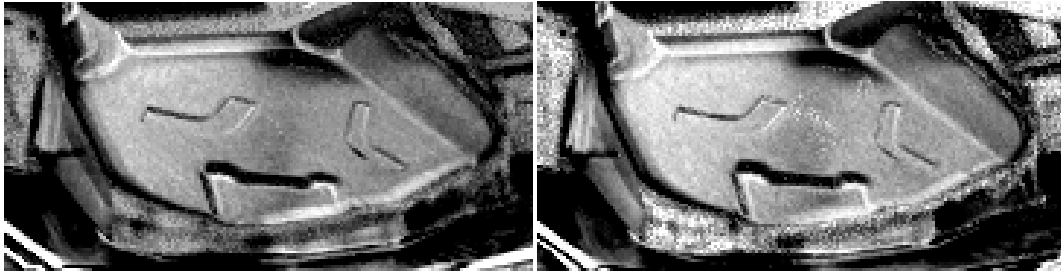


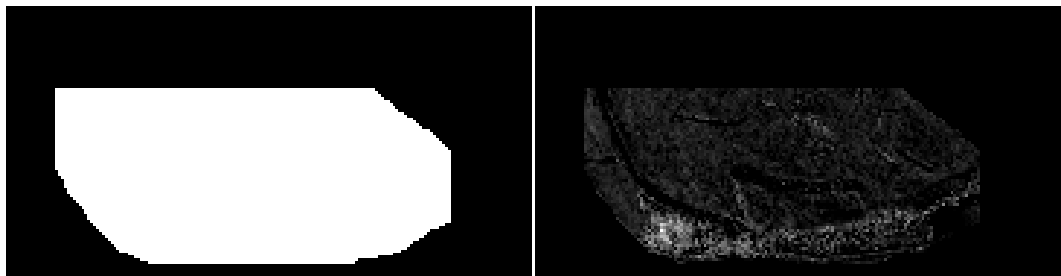
Figure 5.16: Flow Chart of Stamping Split Detection

Two typical stamping split samples of an automotive stamping production line are utilized to test the split detection system. The intermediate results of the split detection process are shown in Figure 5.17 and Figure 5.18. This split detection system precisely detected small split, large split and multiple splits.



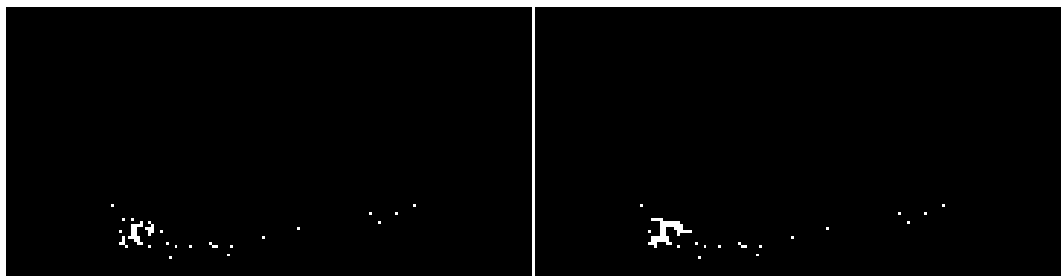
(a)

(b)



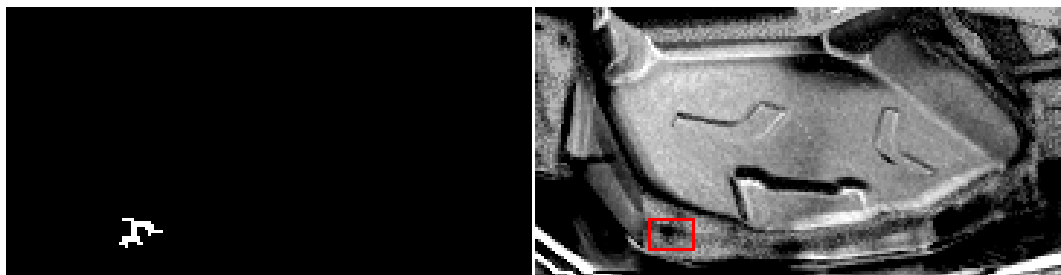
(c)

(d)



(e)

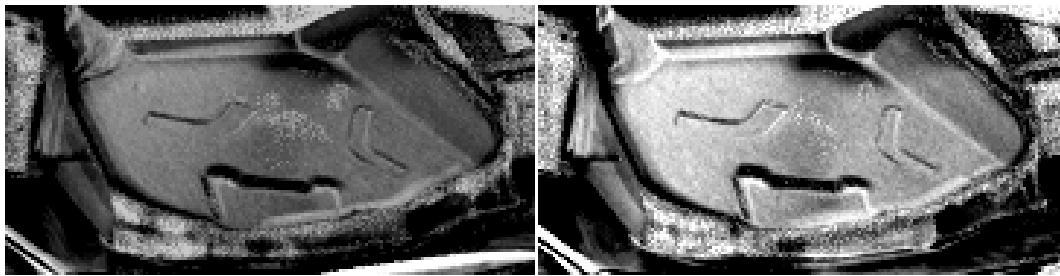
(f)



(g)

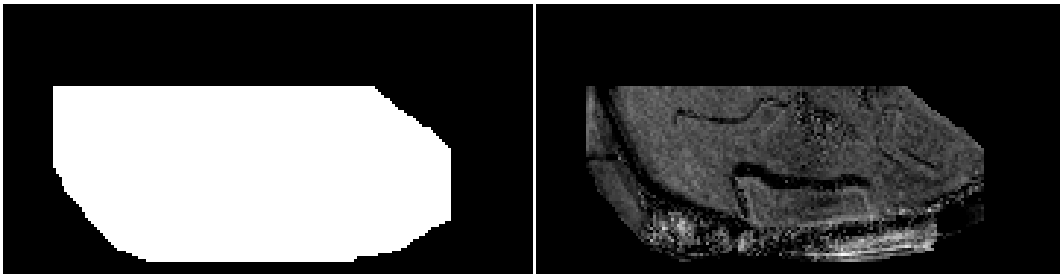
(h)

Figure 5.17: Stamping Split Detection Intermediate Results of Sample 1: (a) Fused Image; (b) Template Image; (c) ROI; (d) Masked Contrast Image; (e) Detected Regions; (f) Regions after Closing; (g) Split Region; (h) Original Image with Split Detection



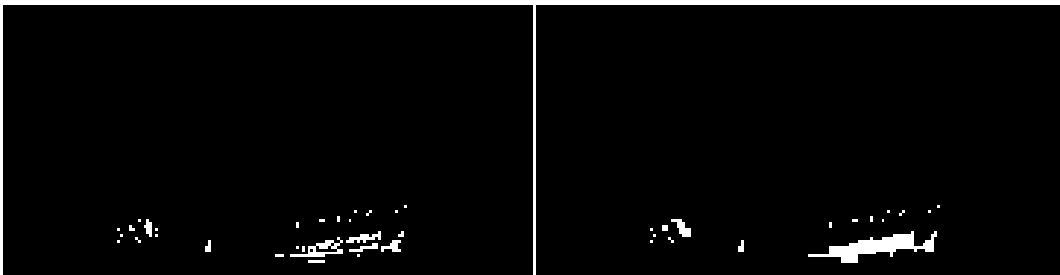
(a)

(b)



(c)

(d)



(e)

(f)



(g)

(h)

Figure 5.18: Stamping Split Detection Intermediate Results of Sample 2: (a) Fused Image; (b) Template Image; (c) ROI; (d) Masked Contrast Image; (e) Detected Regions; (f) Regions after Closing; (g) Split Region; (h) Original Image with Split Detection

5.9 Summary

This chapter integrated Thermography, image fusion and PCA to build an integrated system for online stamping split detection. First, the system overview is presented including the hardware and software architecture. Then, design and implementation of the camera system, image acquisition, GUI, PCA, image fusion and split detection are presented in sequence with technical details. Later on, test results are evaluated using various evaluation criteria and compared with the original images to show the significant enhancement of PCA and image fusion. Finally, the split detection algorithm is tested using typical split samples and shows precise detection of small split, large split and multiple splits.

CHAPTER SIX

CONCLUSION

6.1 Conclusion

This dissertation presented a novel scheme for PCA based image fusion with application in stamping split detection. A thermal and visible imaging based vision system is developed to provide online objective evaluation of stampings and to improve automotive stamping process control. This system utilizes a thermal camera and a visible camera controlled by in-house software to integrate Thermography, PCA and image fusion for stamping split detection application. The Thermography system is capable of discovering the split from thermal emission to avoid the problem of reflection and illumination but missing geometry details due to the heat diffusion. The visible camera system is capable of acquiring high quality images with fine resolution and geometry details but suffers from the reflection and affects of the ambient environment. The fusion of thermal and visible camera systems provides a solution to retain useful information from both physical channels and provides more informative fusion results. To enhance the image fusion result, PCA is utilized on both thermal image and visible image to reduce noises and increase SNR. Result images show great enhancement of the split contrast to the background and the SNR is also effectively increased to facilitate split detection.

First, stamping process control methods are presented with a comprehensive literature review. And then, Thermography is introduced in stamping split detection with theory and applications. Furthermore, an application research using Thermography for

stamping split detection is demonstrated in technical details including the Thermoelasticity theory, the image processing algorithms, and the split detection and tracking algorithms. Finally, split detection results show good accuracy and stability on detection of split with various size and shape.

Next, the image fusion techniques are employed to combine thermal and visible camera systems to enhance the result image and offset the drawbacks of both sides. Image fusion techniques are introduced from three levels: pixel level, feature level and decision level. Pixel level image fusion is chosen as the topic of this dissertation due to its fast speed merit for time critical applications. And then, a literature review is presented including weighted average, comparison, and MSD. Furthermore, an image fusion application in night vision is demonstrated with technical details. Both pixel level image fusion and feature level image fusion are designed and implemented to enhance the original thermal image and visible image. Comparison between pixel level image fusion and feature level image fusion is also made to show the advantages and disadvantages on both sides.

Later on, PCA is introduced with literature review in both Thermography and image fusion. Then the implementation of PCA is presented from mathematical angle and three implementation methods are shown in sequence, original PCA, SVD based PCA and economical SVD based PCA. Furthermore, an application research using PCA in Thermography is demonstrated to show the feature enhancement for product inspection. And another application research using PCA in night vision is also demonstrated to show the image enhancement and noise reduction in fusion results.

Finally, a system integration of Thermography, PCA and image fusion is accomplished to build an integrated PCA based image fusion system for stamping split detection. System overview is first presented including the hardware and software architecture. Then the development of each system module is presented one by one including, the camera system, image acquisition, GUI, PCA, image fusion and split detection. Image fusion results are evaluated using statistics based and feature based criteria and compared with the original images to show the enhancement due to PCA and image fusion. Finally, the split detection algorithm shows precise detection of small split, large split and multiple splits.

6.2 Contributions

An integrated automatic stamping split detection system is developed for online application. The key technical contributions are thermal and visual camera system control and communication, PCA implementation, image fusion algorithm development, and GUI development for data input & output, settings, and display. The integrated stamping split detection system is also tested on real stamping line and capable of detecting split with various size, shape and number.

This work is among the first few researches in building online objective stamping split detection application. Previously related works usually focus on mechanical characteristic analysis of stamping die system using sophisticated mathematical model which consumes tons of time and doesn't meet the requirements of industry online application. These limitations make them still on the phase of experimental research and

experiment. While, this work adopted advanced image processing techniques on direct split detection and is capable of finishing the evaluation in seconds which makes it stands out of other related works.

The fusion of thermal and visible camera systems is innovative in stamping split detection application. Previous work utilized either thermal system or visible system but suffering from blurring problems of thermal system or illumination and reflection problems of visible system. This work fuses thermal and visible system to offset drawbacks of both sides and gets more informative results than either one. The employment of visible camera system overcomes the heat diffusion problem of Thermography and provides detailed geometrical information of the target object which also extends application horizon of Thermography and improves the accuracy and stability of the entire split detection system.

The employment of PCA is vital in highlighting features with strong influence, reducing noise level and also increasing the SNR which makes significant contributions to precise and reliable split detection. The economical SVD based PCA significantly decreases the scale of the matrix operations and shortens the precious processing time to seconds which makes it possible for online split detection application.

6.3 Limitations and Future Work

The resolution of the FLIR ThermoVison A40M uncooled thermal camera is only 320×240 with 8-bit depth that is far not fine enough. Especially in this application, the split is relatively small compared with the whole wheelhouse part and the low resolution

and high noise level almost cover the slight split for recognition or detection. Therefore, it's necessary to upgrade the ThermoVison A40M uncooled thermal camera to FLIR SC6000 cooled thermal camera or higher. The FLIR SC6000 cooled thermal camera has 640×512 resolution, 125Hz full frame rate and flexible FPA windowing. And it is also controllable through SDK for in-house program which makes the automatic detection possible.

The alignment of thermal camera and visible camera is so hard and time consuming especially when working onsite on the press line. First of all, the field of views of the thermal camera and visible camera do not well match. For a typical dual camera system, a stereo camera system, two identical cameras are utilized to avoid the problem of field of view variations. However, in this image fusion system, it is impossible to use identical cameras because the thermal camera and visible camera are made by different vendors and physically different. Therefore, sophisticated optical lenses and precise optical mounting system are necessary to compensate the slight deviations. However, perfectly fit lenses are also not available in the market. Therefore, the lens closest to the requirements is purchased. An experimental mounting system is customized but still not precise enough for fine alignment of these two cameras.

The frame rate of this system is about 5 to 10 Hz depending on whether saving the acquired image frames at the mean time of processing. A faster hard disk drive is also necessary to accelerate the performance of the entire system. Solid state drive is a good choice for the hard disk drive upgrade. Other upgrades including CUP, RAM and motherboard bandwidth are also helpful.

This stamping split detection system is based on the thermal emission and visible light. Therefore, it is only capable of detecting split on the surface facing to the system. For geometry complex part having splits at the back or on hidden surfaces, another split detection system might be needed. To send out the feedback to the press line system, an interface to the stamping station needs to be developed. The detection results should also be presented to the operators in a convenient way and integrated into their stamping control system.

Finally, although, current system is capable of detecting typical online stamping splits, the accuracy, reliability, repeatability and other specifications are still not available and need to be evaluated by time. Systematical evaluation and validation need to be employed to evaluate this system before employed in real application. Other evaluation items are also necessary including the pass and fail rate, the split size limit, the environment effects, and so forth.

REFERENCES

- [1] M. B. Silva, *et al.*, "Stamping of automotive components: a numerical and experimental investigation," *Journal of Materials Processing Technology*, vol. 155-156, pp. 1489-1496, 2004.
- [2] K. D. Majeske and P. C. Hammett, "Identifying Sources of Variation in Sheet Metal Stamping," *International Journal of Flexible Manufacturing Systems*, vol. 15, pp. 5-18, 2003.
- [3] A. S. De Ruyter, *et al.*, "Estimating quality costs in an automotive stamping plant through the use of simulation," *International Journal of Production Research*, vol. 40, pp. 3835 - 3848, 2002.
- [4] GOM mbH, "Modern measuring tools in stamping applications for complex and simple parts," ed, 2009.
- [5] C. P. Lai, *et al.*, "Grids Reformation for Effective Strain Measurement of Forming Titanium Tailor-Welded Blanks at Elevated Temperatures," in *Experimental Analysis of Nano and Engineering Materials and Structures*, ed, 2007, pp. 459-460.
- [6] N. Mahayotsanun, *et al.*, "Tooling-integrated sensing systems for stamping process monitoring," *International Journal of Machine Tools and Manufacture*, vol. 49, pp. 634-644, 2009.
- [7] S. Sah and R. X. Gao, "Process monitoring in stamping operations through tooling integrated sensing," *Journal of Manufacturing Systems*, vol. 27, pp. 123-129, 2008.
- [8] P. Sun, *et al.*, "Control system of a mini hydraulic press for evaluating springback in sheet metal forming," *Journal of Materials Processing Technology*, vol. 176, pp. 55-61, 2006.
- [9] J. A. Ferreira, *et al.*, "Close loop control of a hydraulic press for springback analysis," *Journal of Materials Processing Technology*, vol. 177, pp. 377-381, 2006.
- [10] S.-W. Lo and G.-M. Jeng, "Monitoring the Displacement of a Blank in a Deep Drawing Process by Using a New Embedded-Type Sensor," *The International Journal of Advanced Manufacturing Technology*, vol. 15, pp. 815-821, 1999.
- [11] S.-W. Lo and T.-C. Yang, "Closed-loop control of the blank holding force in sheet metal forming with a new embedded-type displacement sensor," *The*

- International Journal of Advanced Manufacturing Technology*, vol. 24, pp. 553-559, 2004.
- [12] H. Zheng, *et al.*, "Automatic inspection of metallic surface defects using genetic algorithms," *Journal of Materials Processing Technology*, vol. 125-126, pp. 427-433, 2002.
- [13] E. Doege, *et al.*, "Contactless on-line measurement of material flow for closed loop control of deep drawing," *Journal of Materials Processing Technology*, vol. 130-131, pp. 95-99, 2002.
- [14] E. Doege, *et al.*, "Development of an Optical Sensor for the Measurement of the Material Flow in Deep Drawing Processes," *CIRP Annals - Manufacturing Technology*, vol. 52, pp. 225-228, 2003.
- [15] G. Fernando, "On-line machine vision system for detect split defects in sheet-metal forming processes," 2006, pp. 723-726.
- [16] E. de la Fuente, *et al.*, "Detection of small splits in car-body manufacturing," in *SPPRA'03: 3rd IASTED International Conference on Signal Processing, Pattern Recognition and Applications, 30 June-2 July 2003*, Anaheim, CA, USA, 2003, pp. 354-9.
- [17] Y.-M. H. Ng, *et al.*, "Diagnosis of sheet metal stamping processes based on thermal energy distribution," in *2005 IEEE International Conference on Automation Science and Engineering (CASE), 1-2 Aug. 2005*, Piscataway, NJ, USA, 2005, pp. 191-6.
- [18] Y.-M. H. Ng, *et al.*, "Diagnosis of sheet metal stamping processes based on 3-D thermal energy distribution," *IEEE Transactions on Automation Science and Engineering*, vol. 4, pp. 22-30, 2007.
- [19] J. Beyerer, "Model-based analysis of groove textures with applications to automated inspection of machined surfaces," *Measurement*, vol. 15, pp. 189-99, 1995.
- [20] G. A. Al-Kindi, *et al.*, "An application of machine vision in the automated inspection of engineering surfaces," *International Journal of Production Research*, vol. 30, pp. 241-53, 1992.
- [21] H. Hartmann, *et al.*, "Collector: A new software tool for the support of cell projection in combination with variable shape electron beam lithography for mask and direct write applications," *Microelectronic Engineering*, vol. 46, pp. 197-200, 1999.

- [22] N. Guid, *et al.*, "Surface interrogation methods," *Computers & Graphics*, vol. 19, pp. 557-74, 1995.
- [23] Materials & Manufacturing Directorate. (2008). *Passive Thermographic Imaging Shows Promise for Detecting Hidden Corrosion*.
- [24] M. Omar and Y. Zhou, "Pedestrian tracking routine for passive automotive night vision systems," *Sensor Review*, vol. 27, pp. 310-16, 2007.
- [25] M. Omar and K. Saito, "IR Thermography for the Nondestructive Evaluation of the Protective Coating Coverage on Steel Substrates," presented at the 3rd MENDT - Middle East Nondestructive Testing Conference & Exhibition, 2005
- [26] M. Omar, *et al.*, "Infrared seed inspection system (IRSIS) on painted car shells," *Infrared Physics and Technology*, vol. 48, pp. 240-248, 2006.
- [27] A. Chrysochoos and H. Louche, "Infrared image processing to analyze the calorific effects accompanying strain localization," *International Journal of Engineering Science*, vol. 38, pp. 1759-1788, 2000.
- [28] T. Boulanger, *et al.*, "Calorimetric analysis of dissipative and thermoelastic effects associated with the fatigue behavior of steels," *International Journal of Fatigue*, vol. 26, pp. 221-9, 2004.
- [29] G. Brustenga, *et al.*, "Measurements of stress pattern on roll bearing supports by thermoelasticity," in *CD proceedings of the SEM Spring Conference*, 2003.
- [30] T. Ummenhofer and J. Medgenberg, "On the use of infrared thermography for the analysis of fatigue damage processes in welded joints," *International Journal of Fatigue*, vol. 31, pp. 130-137, 2009.
- [31] O. Hatamleh, "A comprehensive investigation on the effects of laser and shot peening on fatigue crack growth in friction stir welded AA 2195 joints," *International Journal of Fatigue*, vol. 31, pp. 974-988, 2009.
- [32] N. Harwood and W. M. Cummings, *Thermoelastic stress analysis*. Bristol, UK: Adam Hilger, 1991.
- [33] A. S. Khan and S. Huang, *Continuum Theory of Plasticity*: Wiley-Interscience, 1995.
- [34] E. Planting, "Thermoelastic behavior of a small bearing cage," Masters Thesis, Mechanical Engineering, Clemson University, Clemson, 2009.

- [35] Y. Zhou and M. Omar, "Dynamic-template processing for passive thermograms: Applied to automotive stamping split detection," *NDT and E International*, vol. 41, pp. 582-588, 2008.
- [36] M. A. Omar, *et al.*, "Automated applications of the infrared imagers in the automotive assembly lines: products and process control," in *Thermosense XXIX, 9 April 2007*, USA, 2007, pp. 65410-1.
- [37] M. Omar, *et al.*, "IR self-referencing thermography for detection of in-depth defects," *Infrared Physics & Technology*, vol. 46, pp. 283-9, 2005.
- [38] Z. Zhang and R. S. Blum, "Region-Based Image Fusion Scheme For Concealed Weapon Detection," in *In Proceedings of the 31st Annual Conference on Information Sciences and Systems*, 1995.
- [39] J. Lanir, *et al.*, "Comparing multispectral image fusion methods for a target detection task," *Optical Engineering*, vol. 46, pp. 66402-1, 2007.
- [40] J. Liu, *et al.*, "Comparisons of several pixel-level image fusion schemes for infrared and visible light images," in *Proceedings of the IEEE Instrumentation and Measurement Technology Conference, 16-19 May 2005*, Piscataway, NJ, USA, 2005, p. 4 pp.
- [41] G. Pajares and J. M. de la Cruz, "A wavelet-based image fusion tutorial," *Pattern Recognition*, vol. 37, pp. 1855-72, 2004.
- [42] M. Kumar, "Model based image fusion," Ph.D. Dissertation, Electrical engineering, Michigan State University, 2008.
- [43] Z. Zhang and R. S. Blum, "A categorization of multiscale-decomposition-based image fusion schemes with a performance study for a digital camera application," *Proceedings of the IEEE*, vol. 87, pp. 1315-26, 1999.
- [44] J. J. Lewis, *et al.*, "Pixel- and region-based image fusion with complex wavelets," *Information Fusion*, vol. 8, pp. 119-30, 2007.
- [45] R. S. Blum and Z. Liu, *Multi-Sensor Image Fusion and Its Applications*: CRC Press, 2005.
- [46] G. Hong and Y. Zhang, "High resolution image fusion based on wavelet and IHS transformations," in *2nd GRSS/ISPRS Joint Workshop on Remote Sensing and Data Fusion over Urban Areas. URBAN 2003, 22-23 May 2003*, Piscataway, NJ, USA, 2003, pp. 99-104.

- [47] H. Li, *et al.*, "Multisensor image fusion using the wavelet transform," *Graphical Models and Image Processing*, vol. 57, pp. 235-45, 1995.
- [48] P. R. Hill, *et al.*, "Image fusion using a new framework for complex wavelet transforms," in *2005 International Conference on Image Processing, 11-14 Sept. 2005*, Piscataway, NJ, USA, 2006, pp. 1338-41.
- [49] Y. Zhou and M. Omar, "Pixel-Level fusion for infrared and visible acquisitions," *International Journal of Optomechatronics*, vol. 3, pp. 41-53, 2009.
- [50] O. David, *et al.*, "Range gated active night vision system for automobiles," *Applied Optics*, vol. 45, pp. 7248-54, 2006.
- [51] Y. Zhou, *et al.*, "Feature-level and pixel-level fusion routines when coupled to infrared night-vision tracking scheme," *Infrared Physics & Technology*, vol. 53, pp. 43-9, 2010.
- [52] N. Rajic, "Principal component thermography for flaw contrast enhancement and flaw depth characterisation in composite structures," *Composite Structures*, vol. 58, pp. 521-8, 2002.
- [53] S. Marinetti, *et al.*, "Statistical analysis of IR thermographic sequences by PCA," in *7th International Workshop on Advanced Infrared Technology and Applications, 9-11 Sept. 2003*, Netherlands, 2004, pp. 85-91.
- [54] Y. Zheng, *et al.*, "Effective image fusion rules of multi-scale image decomposition," in *2007 5th International Symposium on Image and Signal Processing and Analysis, 27-29 Sept. 2007*, Piscataway, NJ, USA, 2007, pp. 90-4.
- [55] Q. Miao and B. Wang, "A novel image fusion algorithm using FRIT and PCA," in *FUSION 2007 - 2007 10th International Conference on Information Fusion, July 9, 2007 - July 12, 2007*, Quebec, QC, Canada, 2007.
- [56] S. Singh, *et al.*, "Infrared and visible image fusion for face recognition," in *Biometric Technology for Human Identification, 12-13 April 2004*, USA, 2004, pp. 585-96.
- [57] FLIR Systems Inc, "ThermoVision A40-M Specification, ," ed, 2005.
- [58] Edmund Optics Inc. (2010). *IEEE-1394/FireWire VGA Board Level Cameras*. Available: <http://www.edmundoptics.com/onlinecatalog/displayproduct.cfm?productID=2631>
- [59] FLIR Systems Inc., "ThermoVision SDK," ed, 2010.

- [60] FLIR Systems Inc, "ThermoVision SDK User's Manual V2.6," ed, 2007.
- [61] The MathWorks Inc. (2010). *Image Acquisition Toolbox Overview*. Available: <http://www.mathworks.com/access/helpdesk/help/toolbox/imaq/f11-6381.html>
- [62] The MathWorks Inc., "Image Acquisition Toolbox 3.2," ed, 2008.
- [63] The MathWorks Inc. (2010). *What Is a GUI?* Available: http://www.mathworks.com/access/helpdesk/help/techdoc/creating_guis/f2-998436.html
- [64] The MathWorks Inc. (2010). *How Does a GUI Work?* Available: http://www.mathworks.com/access/helpdesk/help/techdoc/creating_guis/f2-998548.html
- [65] Y. Chen, "Investigation of image fusion algorithms and performance evaluation for night vision," Ph. D. Dissertation, Electrical engineering, Lehigh University, 2007.
- [66] Y. QIU, *et al.*, "Multi-sensor image data fusion based on pixel-level weights of wavelet and the PCA transform," in *2005 IEEE International Conference on Mechatronics and Automation, 29 July-1 Aug. 2005*, Piscataway, NJ, USA, 2005, pp. 653-8.